UNIVERSITÀ DEGLI STUDI DI MILANO
FACOLTÀ DI SCIENZE E TECNOLOGIE

DEPARTMENT OF PHYSICS
PHD SCHOOL IN
PHYSICS, ASTROPHYSICS AND APPLIED PHYSICS
CYCLE XXXVIII

Engineering the complex electrical response of metallic cluster-assembled films for neuromorphic computing applications

Disciplinary Scientific Sector FIS/03

PhD Thesis of:

Davide Decastri

Matr. R13961

Orcid: 0009-0004-5822-0388

Supervisor: Prof. Paolo Milani

Co-supervisor: Dott.ssa Francesca Borghi

PhD school director: Prof. Aniello Mennella

A.Y. 2024 - 2025

To my parents, to my friends,

and to all those who have cared for me.

Abstract

Mammalian brain outperforms modern computers in executing complex tasks with high energy efficiency. These capabilities rely on the processing of stimuli by a network consisting in thousand billion neurons intricately interconnected through synapses. Neurons integrate signals in a non-linear way. Synapses can modulate their effectiveness according to stimuli (synaptic plasticity), providing the basis for learning. Nontrivial responses to stimuli are due to the collective dynamics regulating the network operations along with network topology.

Neuromorphic Computing (NC) draws inspiration from the structure and operation of the brain to offer an alternative to the present Von Neumann paradigm of computation. Metallic cluster assembled films (MCAFs) constitute a potential physical substrate for this scope due to their topological complexity, non-linear conduction properties, and plasticity.

A key role in determining MCAF conduction properties is played by their ability to undergo reversible structural modifications, thus producing changes in their electric conductivity. This phenomenon is referred as Resistive Switching (RS). Even if MCAF based devices have been already exploited in different computing tasks, we still have poor insight on the physics underlying the complex dynamics that govern RS activity. The main goal of my thesis is to exploit a novel approach relying on micro-thermography to characterize the evolution of conductivity in MCAF and gain a deeper understanding of this rich phenomenology. My analysis led to the identification of “switching sites” undergoing the structural modifications responsible of RS. This strategy also allowed to study the statistical properties of RS in space and time, unveiling the presence of non-trivial correlations in these systems. My analysis also highlighted the impact of sample geometry and dimension on the number and distribution of the switching regions. Furthermore, I probed the electrical response to different stimuli, and I observed stereotyped behaviours that emerge from the average response of the switching regions. Modelling the deterministic component of the electrical response, offers the possibility to enhance controllability of MCAF based devices, while the intrinsic stochasticity provides a natural mechanism for efficient state-space exploration, ultimately supporting efficient programmability of such systems.

Contents

1 Introduction

1.1 The challenges of neuromorphic computing

The advent of the first microprocessor in 1971 and the commercialization of personal computers in the late 70s [1], paved the way for the last technological revolution in humankind, namely, the digital revolution. Nowadays digital computing technology is becoming ubiquitous: billions of devices are connected thorough cloud services [2], continuously collecting and processing information. The amount of digital data produced worldwide is growing exponentially [3], [4] (figure 1a), thus pushing the computational capabilities of modern computers to the limit [5], [6]. Furthermore, recent advances in automation, quality control, and large-scale data analytics have led to increasing interest in the development and adoption of Artificial Intelligence (AI), and in particular Deep Learning (DL) algorithms. In recent years, these brain inspired models have achieved remarkable breakthroughs, surpassing human performance in different tasks [7]. However, this outstanding progress highlighted the limitations of the classical computational paradigm. Despite continuous hardware improvements, digital computers have shown to be energetically inefficient [8]. As a result, the growing computational demand is driving a fast increase in power consumption (figure 1b), with the energy footprint of digital technologies already hitting that of entire countries.

New efficient computing strategies are needed to deal with these challenges. A source of inspiration is the mammalian brain. Thanks to its peculiar architecture and properties, such as self-adaptation and parallel processing, the brain achieves ultralow power consumption and high robustness [9]. *Neuromorphic computing* indicates all the computational strategies that take inspiration from brain functioning to perform efficient data processing. Assemblies of nano-objects with synaptic like behaviour can be exploited in this framework, and significant proof of concepts for many computing applications have been presented [10].

In the following introduction, I first provide a brief review of the classical paradigm of digital computing, with specific focus on the sources of power inefficiency. Then I will cover the topic of unconventional computing strategies, highlighting the potential of these novel approaches.

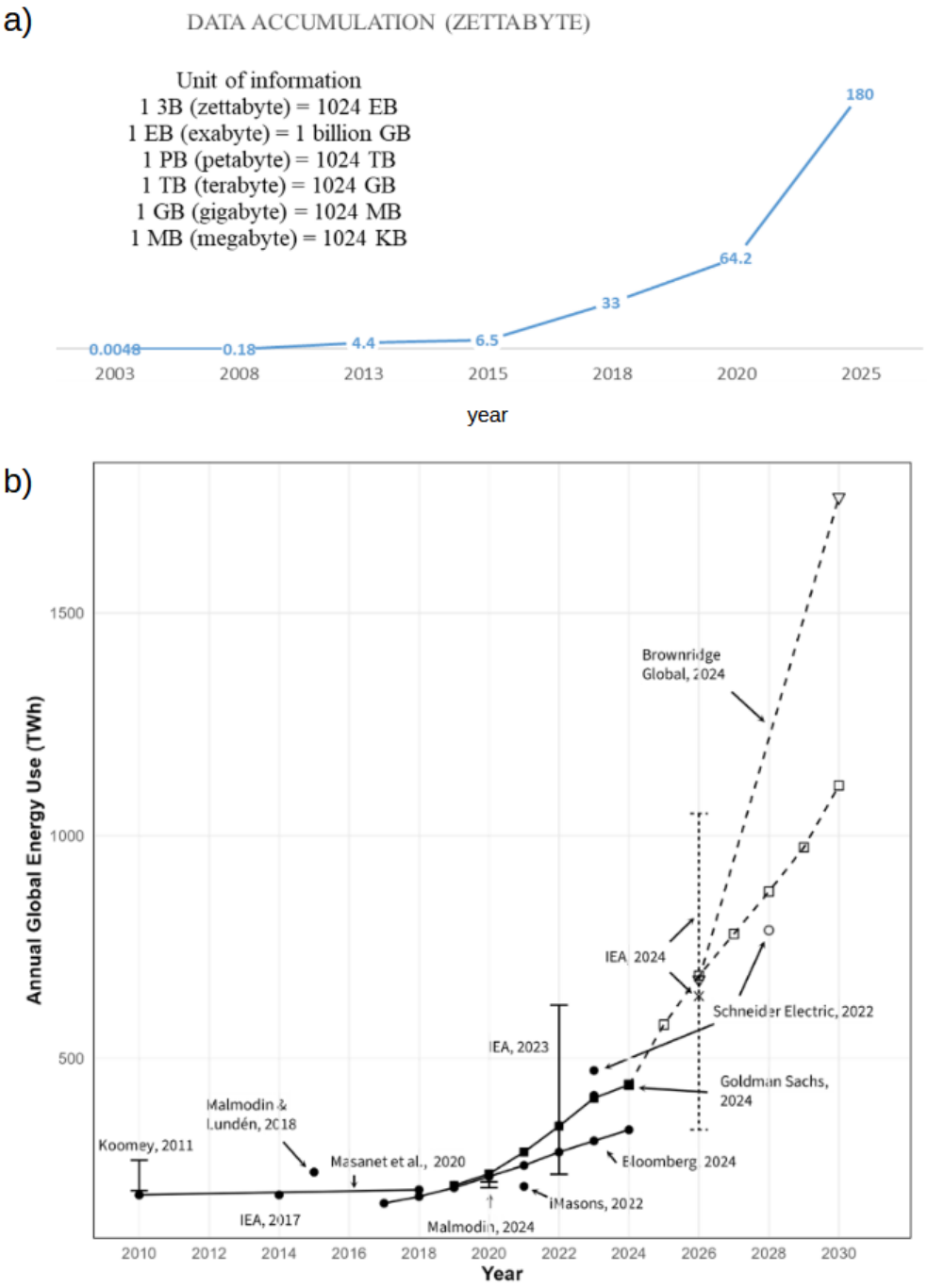

Figure 1: a) Stored digital information over time (worldwide). Adapted from [4]. b) Evolution of data centres energy consumption over time. Dashed lines represent five years forecasts. Adapted from [11].

1.2 Digital computing

In 1936 Alan Turing addressed Hilbert famous *Entscheidungsproblem* (or *decision problem*) [12]: the problem asked to prove the existence of an algorithm capable of determining whether any unspecified statement in first-

order logic is provable or not. Turing proved that this problem is impossible to solve [13]. However, the significance of Turing seminal work went far beyond the solution of Hilbert problem. In a section of his proof, Turing introduced the idea of universal computing machine, later known as the "Turing machine" [14].

1.2.1 Turing machines

The conceptual framework described by Turing represent the first formalization of the model of computation that underpins the functioning of modern computers (see [15] for a formal definition of the Turing machine). Specifically, a Turing machine is an abstract device consisting in an infinite writable tape and a read-write head that operates on the tape according to some rules that are executed in discrete time steps, or *operating cycles* [16]. The tape is segmented in sections, each containing a symbol, that can be addressed during an operating cycle. The read-write head operates as a finite state machine [17], [18], i.e., it possesses an internal state that can be updated during every cycle. The operating cycle consists in four steps [16]:

- Reading the symbol in the section of tape underneath the head.
- Erasing the symbol.
- Performing on operation according to the rules and the internal state. The operation consists in writing a new symbol and/or move the tape to another section.
- Updating the internal state.

The machine performs a sequence of operating cycles until a certain halting criterion is met. Despite its simplicity, the computing model of the Turing machine embodies all the essential features of a programmable computing machine capable of executing an algorithm to solve a problem.

It is possible to identify some key ingredients of this abstract picture. The first one is the representation of the data that are read and written on the tape by means of an alphabet: the Turing machine implements a rule-governed mechanisms that handles *symbolic* representations of physical quantities [19].

Two main consequences derive from this fact: first of all, the ability to implement algorithms, i.e., to perform a sequence of operations according to a set of instructions. For this reason, there is an intimate connection between Turing machines and human logical thinking (this is what H. Jaeger define *computing-cognition match* [20]). Namely, a Turing machine can be programmed, i.e., instructed to perform a task by implementing a series of rules derived from a well-established framework in first-order logic [21]. The second consequence is that, in general, the physical implementation of a Turing machine is challenging. First of all, one has to find a proper way to map symbols into a physical substrate. Then, he must exploit some phenomena that read and transform that symbols, obeying specific rules [19]. In modern digital computers, for example, Boolean 0 and 1 are codified in different values of voltages and logic operations are implemented by means of transistor-based logic gates.

Another key ingredient in the Turing machine is the sequential operation. The write-read head operates as a finite state machine, so it updates the symbols on the tape along with its internal state in a series of time steps, till obtaining the final result. From a theoretical point of view, this is not a problem, since every parallel machine can be reduced to a sequential one.

1.2.2 Von Neumann Architecture

Ten years after the publication of Turing groundbreaking work, John von Neumann gave a fundamental contribution to the development of Electronic Discrete Variable Automatic Computer **(**EDVAC), one of the first general purpose electronic digital computers [22], [23]. The EDVAC stored binary information (both data and user-specified instructions) in mercury delay-line memories and performed Boolean logic operations by means of tens thousands vacuum tubes [24].

Beyond the practical realization of the machine, the significance of von Neumann work lies in the conceptualization of the design of modern computers. His proposal inherits all the essential features of the Turing machine, and nowadays known as *von Neumann architecture* [22], [25], [26]. The key features of the von Neumann architecture are schematized in figure 2.

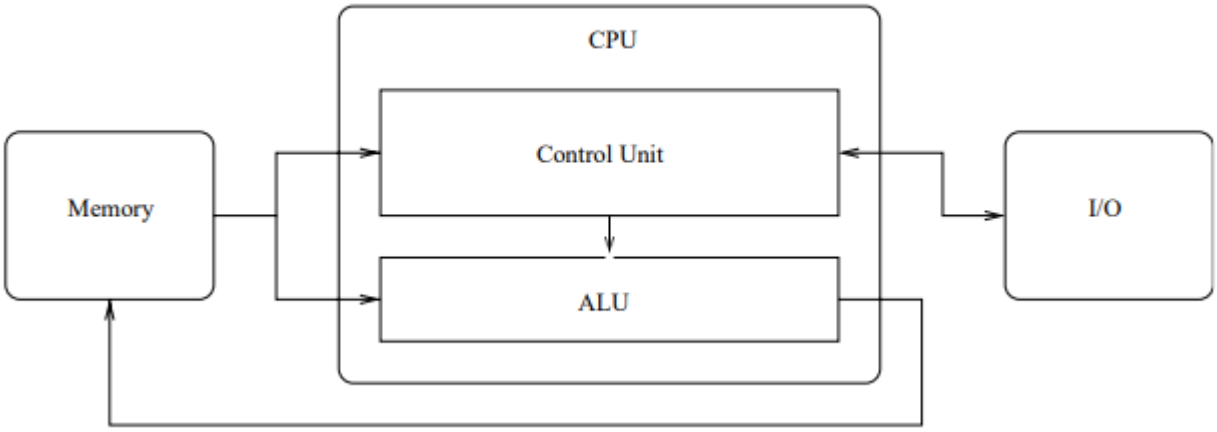

Figure 2: scheme of the von Neumann architecture. From [26].

Von Neumann architecture consists in a Central Processing Unit (CPU) and a memory unit. The CPU comprises a control unit that reads and interprets instructions stored in memory and coordinates the operations of an Arithmetic Logic Unit (ALU) that handles and transforms data by performing arithmetic operations. Both data and instructions (i.e., the software) are allocated in the memory unit that is physically distinguished from the CPU. The possibility to store instructions in memory is a significant feature: contrary to all previous computing machine, the one conceptualized by von Neumann does not need to modify the wiring (the

hardware) to implement different functionalities [27]. Nowadays, all commercial computers implement the von Neumann architecture.

1.2.3 The advent of modern computers and the Moore's law

In 1948, the invention of the transistor by J. Bardeen and W. H. Brattain [28] paved the way for the implementation of transistor based logic gates, which replaced vacuum tubes within few years. In late 1960s, the development of Complementary Metal-Oxide Semiconductor (CMOS) technology and Metal Oxide Semiconductor Field Effect Transistors (MOSFETs) transistors [29], set the most significant milestones in the context of digital computing, and a turning point in developing modern computers. After the commercialization of the first CMOS microprocessors in early 1970s [30] the computational performances of digital computers increased rapidly over the years. The performance in digital computers is usually expressed in terms of computational speed, i.e., number of floating-point operations per second (Flop/s). The graph in figure 3 illustrates the evolution of computational power, by reporting the number of Flop/s for different generations of supercomputers.

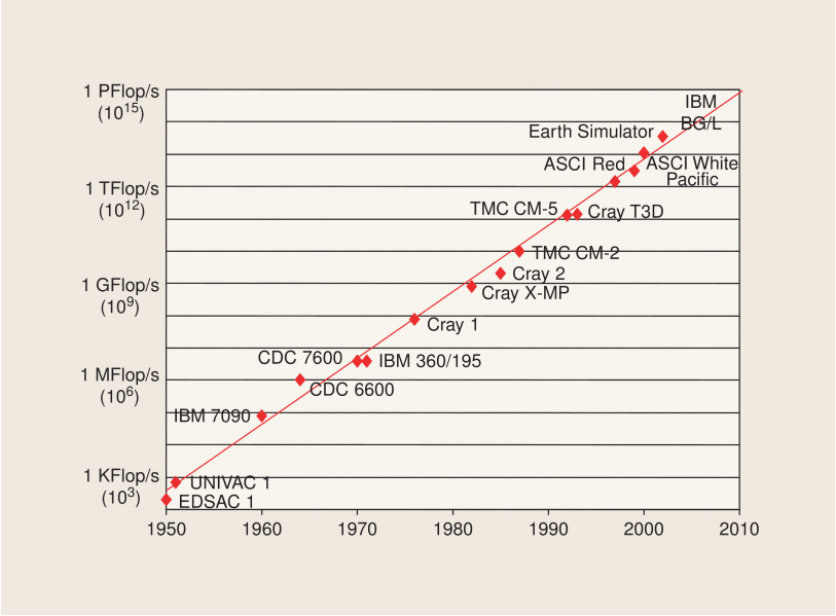

Figure 3: evolution of computational performance in different generations of supercomputers. From [31]

Devices miniaturization, made possible by continuous advances in CMOS microfabrication techniques, had been the driving force for these remarkable progresses in computational performances over the years [29], [32], [33], [34]. The benefit of downscaling to computation efficiency is manyfold: it allows a steady increase of the density of electronic components in integrated circuits, and enhances clock speed [35] (figure 4a-b). Furthermore, energy efficiency is generally enhanced with devices miniaturization: shrinking the two in plane dimensions of the transistors allows to reduce both current and voltage for device operation, thus leading to reduction in the energy consumption. For this reason, as pointed out by R. H. Dennard in 1974, increasing

density of transistors in integrated circuits does not raise the power consumption per unit area, provided the clock frequency remains constant [36].

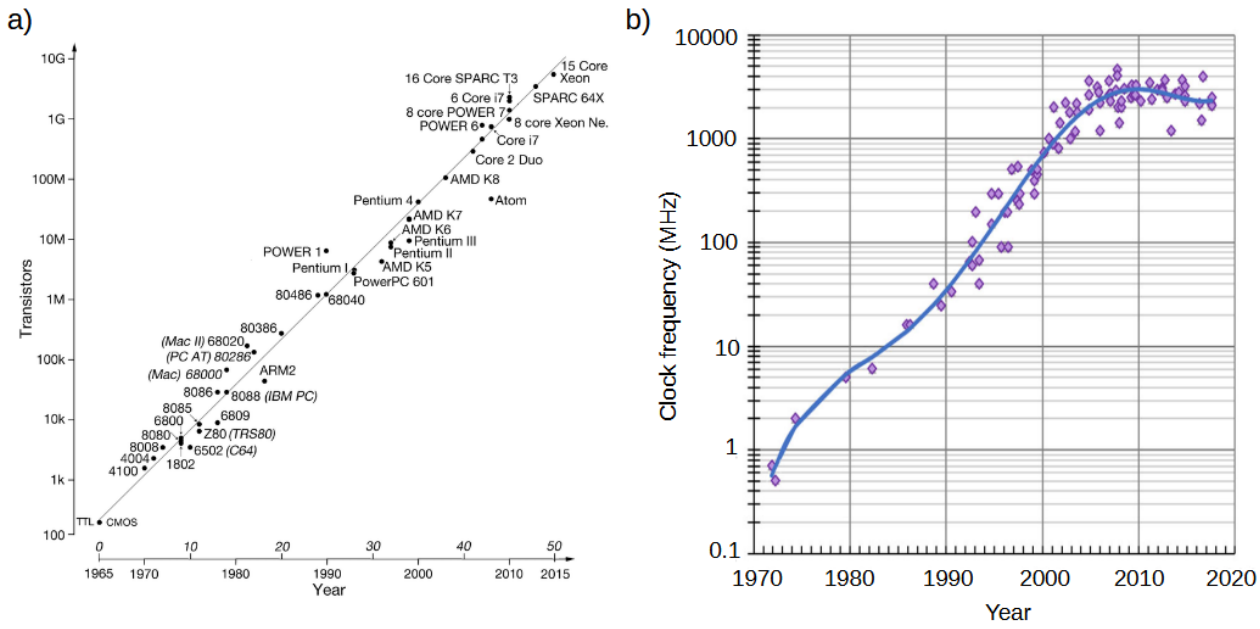

Figure 4: a) evolution of the number of transistors per unit area over time. From [37]. b) Evolution of CPUs clock frequency over time. Adapted from [38].

The trend of devices miniaturization has been forecasted by G. Moore in 1965 [39], who predicted that the number of electronic components integrated on a chip would have doubled roughly every two years. This empirical evidence is often referred to as *Moore law*.

1.3 Limits of digital computing

However, in recent years improvements in circuit microfabrication slowed down significantly [40], facing important issues that are likely to pose a limit to these developments. Here below I report the main ones.

1.3.1 Scalability

Dealing with thermal fluctuations and insulators breakdown below 5 nm node turns to be challenging [41], and, obviously, downscaling has an ultimate limit due to the approaching to atomic scale [42]. A promising strategy, that is currently under investigation, is the three-dimensional packing of transistors [40], [43]. Instead of relying on lateral downscaling, 3D packing exploits the vertical dimension by stacking multiple devices on top of each other within the same chip. This way, it could be possible to significantly increase device density without requiring further reduction of the individual transistor size, thus partially avoiding the limitations of

planar scaling. Nevertheless, scalability is not the main limitation. Miniaturization of electronic components presents further significant technical drawbacks that poses severe limits in computational efficiency.

1.3.2 Heat wall

The first limit is heat dissipation: increasing the density of electronic components turns into an increase in the heat generated through Joule heating. This is a well-known issue in modern PCs, that led to the development of many thermal management strategies [44]. Modern CPU, for example, are not able to run at maximum clock frequency for long periods without incurring in damages due to overheating. For this reason, they implement an automatic control of the temperature for the regulation of the clock frequency. Consequently, improvements in microfabrication techniques must be accompanied by improvements in heat management. In order to understand to which extent heat production in electronic circuits is a major limitation to devices performances, consider the following argument [35]: Landauer found that, due to the irreversibility of thermodynamic processes in the switching operation, the minimum energy required for changing the state of a bit equals to $k_B T log 2$ [45]. Assuming to be able to reach this physical limit in energy efficiency, the minimum device size turn to be limited to $\sim 1.5\ nm$, and the switching time is limited to $\sim 0.04\ ps$ by position-momentum and time-energy uncertainty relations. The power generated per unit surface by staking devices with $1.5\ nm$ of lateral dimension operating at maximum clock frequency equals to $3.7\ MW/cm^2$ [35], that is four orders of magnitude higher than heat produced by last generation chips [46], and well beyond the heat dissipation capability of any dissipator.

1.3.3 Von Neumann bottleneck

Another key limit is intrinsically related to von Neumann architecture, and is usually referred as *memory wall,* or *von Neumann bottleneck* [47]. In von Neumann architecture, memory and computing units are distinct (refer to figure 2), requiring data to be transferred thorough physical interconnects. This introduces three major issues [47], [48]:

- Access data stored in memory introduces a latency that severely limits the achievable computational speed, regardless of the processing power of the CPU.
- Non-ideal interconnects have a limited bandwidth, i.e., only a finite amount of data can be transferred simultaneously, thus creating a bottleneck in the communication.
- Energy consumption due to data transfer is typically higher than the energy required for computing itself [48], [49].

1.3.4 Economical challenges

As we have already seen, during the last decades major efforts have been devoted to improving digital circuits performances. Major advances in this field have been driven by contributions from several disciplines, ranging from micro-lithography to circuit design optimization and materials science. These developments, however,

come at cost of enormous investments for circuit manufacturers. Interestingly, the so-called Moore law is not a mere forecast of technological improvements, but it describes an economic trend. In fact, Moore considers the number of electronic components on a chip as the number which *minimize the cost* of the chip [50]. This implies that, thanks to technological advances, the fabrication of integrated circuits with an increasing number of components has been economically advantageous for a long period of time. Nowadays, the continuation of the Moore law has become mostly a financial challenge. Since the advent of the 100 nm era (namely, over the past 30 years), integrated devices manufacturers struggle to keep up with the unsustainable cost for innovation, with hundred million dollars for chip design and billion dollars for fab modules construction [51], [52]. The GlobalFoundries CEO Doug Grose stated [51]:

"*Despite the technical challenges, the biggest hurdle to continued innovation (in the semiconductor industry) is economics.*"

1.3.5 New challenges from Artificial Intelligence

Nonetheless, the growth in DC utilization is still running, and modern world remains increasingly hungry of computational resources [53]. However, looking at the current trends in DC usage, it is easy to notice significant shifts from the past. Our era is characterized by pervasiveness and ubiquity of digital devices: tens billions electronic devices worldwide, comprising smartphones, smart sensors and embedded systems, are connected to the Internet [54] and continuously collect and transfer data. This scenario, often referred as Internet of Things (IoT), is driving a rapid increase in the volume of information that need to be stored and processed. From 2011 in roughly ten years the amount of data generated worldwide rose by a factor 25, reaching 44 zettabytes (10^{21} bytes) by 2022 [55]. The term *big-data* has been coined to indicate massive datasets characterized by complex structure and composition, and presenting inherent difficulties in storage and analysis [56]. The huge amount of data generated coupled with the vast proportion of unstructured data, overwhelms the possibilities of conventional DC to effectively exploit them. These challenges are further compounded by the diverting of computational resources in emerging applications such as autonomous driving, image and sound recognition, etc.

Artificial Intelligence (AI) models are increasingly adopted to address these needs, owing to their excellent abilities in feature extraction and performing complex tasks on extended and often unstructured datasets. AI refers to all algorithms that enable computing machines to display some sort of intelligent behaviour.

1.3.6 Artificial Neural Networks

Interestingly, biological brain can deal with a large number of stimuli and accomplish many of these tasks effectively and with extremely high energy efficiency. Indeed, the nervous system of any animal is naturally optimized carry out specific functions that are crucial for survival and reproduction with the limited resources that the body can supply. While computers outperform the brain in many logical tasks, such as arithmetic

operations, most of the brain capabilities remained by far unmatched by DC until very recent times. Back in 1990s Carver Mead, one of the pioneers of AI, stated [57]:

"[…] we still cannot begin to do the simplest computations that can be done by the brains of insects, let alone handle the tasks routinely performed by the brains of humans. So, we have finally come to the point where we can see what is difficult and what is easy. Multiplying numbers to balance a bank account is not that difficult. What is difficult is processing the poorly conditioned sensory information that comes in through the lens of an eye or through the eardrum."

The mammalian brain is one of the most complex structures in nature, comprising a complex network of roughly 10^{11} neurons intricately interconnected by 10^{15} synapses. Neurons exhibit a peculiar morphology: the cellular membrane present numerous ramified structures called *dendrites* and a single long protrusion, the *axon* [58], [59]. These tree-like structures significantly increase the surface of the membrane and serve as primary sites for establishing connection between neurons (figure 5a). Neuronal communication occurs thorough electrochemical synapses [60], located along the dendrites and the cell body. The ability of a neuron to respond to stimuli relies on specific physiological properties. At rest, homeostasis allows to maintain a stable potential difference between the two sides of the cellular membrane of approximately -60 mV, that is referred as *membrane potential.* This potential is regulated by both chemically gated and voltage gated ion channels. Each synapse transmits signals with an efficiency that depends on the local density of ion channels, and the different strength of synaptic connections determine the functional connectivity of the network. Synapses can modulate their efficiency on the basis of the incoming stimuli. This property is known as *synaptic plasticity*. Furthermore, a functional distinction exists between the dendrites and the axon: dendrites are used to receive stimuli, while the axon conveys stimuli to other neurons. This anisotropy, referred as *neuronal polarity* [61],

[62], is responsible for the existence of a directionality in the transmission of information in biological neural networks (figure 5b).

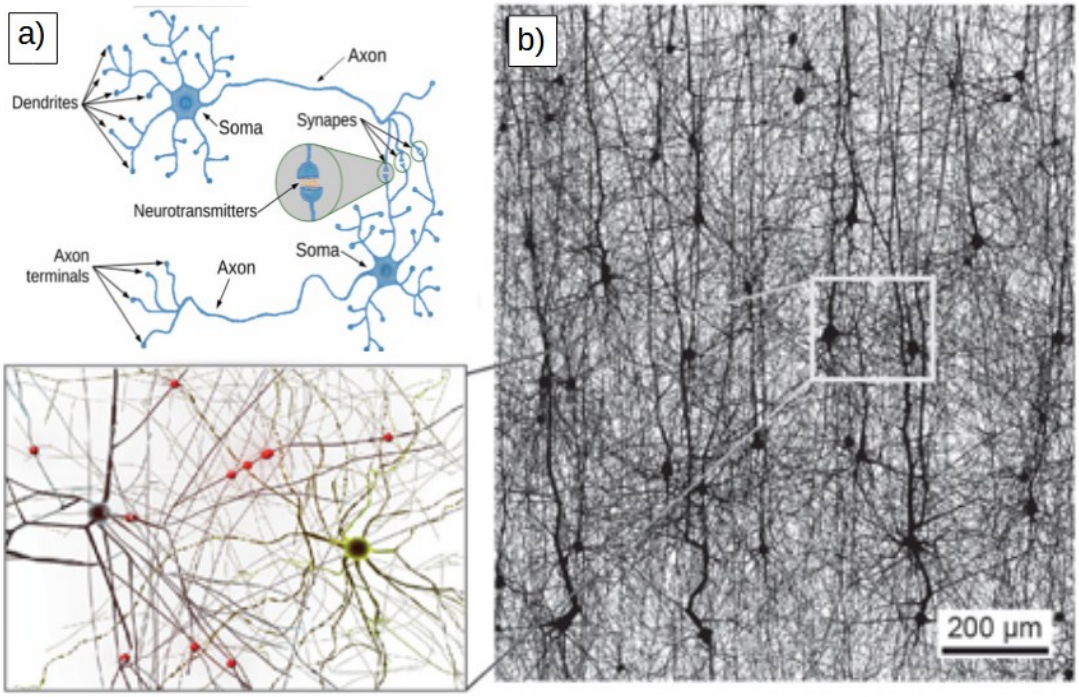

Figure 5: a) schematics of pre-synaptic and post-synaptic neurons. From [63]. b) reconstruction of a portion of a neuronal microcircuit with the algorithm presented in[64]. The density of neurons is set to 5% for better visualization. Adapted from [64].

When a chemical neurotransmitter is released at the synapse by a presynaptic neuron, chemical gated ion channels in the postsynaptic neuron open, and induce a change in the cellular membrane permeability to specific ions (Na^+, K^+ and Cl^-), thus resulting in a variation of the membrane potential. If membrane potential in the soma exceeds a threshold, due to the integration of one or multiple stimuli, voltage gated ion channels open and causes the migration of further positive ions through the axon. This determines a rapid depolarization, taking lasting 1 ms - 5 ms, referred as *action potential* or *spike* [65]. Neuron response to stimuli is strongly nonlinear, as the action potential can only be triggered if the membrane potential exceeds the threshold that triggers this positive feedback loop.

The structure of the dendrites and the distribution of the synapses along the cellular body also plays a crucial role in determining neuronal response. Recent studies have demonstrated that synapses that are close to each

other tend to sum inputs less linearly than synapses that are far apart. As a result, even different regions of the neuron are able to integrate nonlinearly the inputs [66].

Most AI models have drawn inspiration from some of the features of biological neural networks. Among these models, Artificial Neural Networks (ANN) [67], are one of the most popular architecture, and have demostrated impressive performances in identifying complex patterns in large datasets [68]. The origins of ANN interestingly dates back to the very same period of the genesis of the computers and their development has followed a non-linear trajectory. In 1943, McCulloch and Pitts proposed a model for the neuron based on the idea that neuron functions can be represented by means of symbolic logic [69], [70]. In their model, the neuron receives Boolean inputs, integrates them according to their respective synaptic efficiency, and produces an output if the result exceeds certain threshold. This model constitutes the formalization of what later became known as Threshold Logic Gate (TLG).

In 1958 F. Rosenblatt worked on his own model for the neuron, the *perceptron* [71] (figure 6a). Unlike McCulloch and Pitts, Rosenblatt incorporated the possibility to learn, by including synaptic plasticity in his model: by adjusting synaptic efficiencies (or weights), the perceptron is able to learn different tasks. Given an input vector $x = \{x_1, \dots, x_n\}$, the output of the perceptron is:

$$y = \Theta\left(\sum_{i=1}^{n} x_i w_i - t\right) \tag{1.1}$$

Where w_i are the weights, t is a threshold, and Θ is the Heaviside step function ($\Theta(x) = 1$ if $x \geq t$ and 0 otherwise). One of Rosenblatt more interesting intuitions was that neurons processing capabilities is rooted not in symbolic logic, but in statistical separability: perceptron itself acts as a Boolean classifier. However, in 1969, Minsky and Papert showed that Rosenblatt model was unable to solve nonlinearly separable problems (e.g., it is not able to implement the XOR function) [72], and for more than fifteen years this field was abandoned (first AI winter). Actually, the solution of the problem has been found by many authors over the years (notably, by Rosenblatt himself! [71]), and consists in connecting multiple perceptrons in successive layers, forming what would be called a *deep* network. Such an architecture has been shown to be able to implement a wide class of functions. However, the real breakthrough came in 1986 when a leaning algorithm has been introduced, thus allowing to train ANNs efficiently. The algorithm is back-propagation [73] and is still used today to train ANNs: a loss function is introduced to measure the difference between the network output and a target output. The gradient of the loss function with respect of network weights (i.e., the model parameters) of every layer is computed, and weights are adjusted in order to minimize the loss function. Deep Neural Networks (DNNs), i.e., networks with high number of layers were introduced in 2006 [70], and started

to be widely exploited. Deeper architectures improved training techniques, and ANNs achieved the state-of-the-art results in image recognition, natural language processing, and many other domains [68].

Spiking Neural Networks (SNNs) [74] represent a valuable alternative approach to classical ANNs already discussed. These architectures incorporate temporal dynamics by transmitting information through discrete spikes, thus representing more closely brain-inspired models. Exploitation of temporal domain makes SNNs particularly suited for computer vision and robotic control applications [75].

AI models grown in popularity since the introduction of Graphic Processing Units (GPUs) as general purpose cores [76]. GPUs were originally designed for fast graphic rendering, and relies on hundreds cores optimized for parallel processing [77]. This specific feature makes GPU particularly suited for the implementation of AI models, significantly speeding up both training and inference.

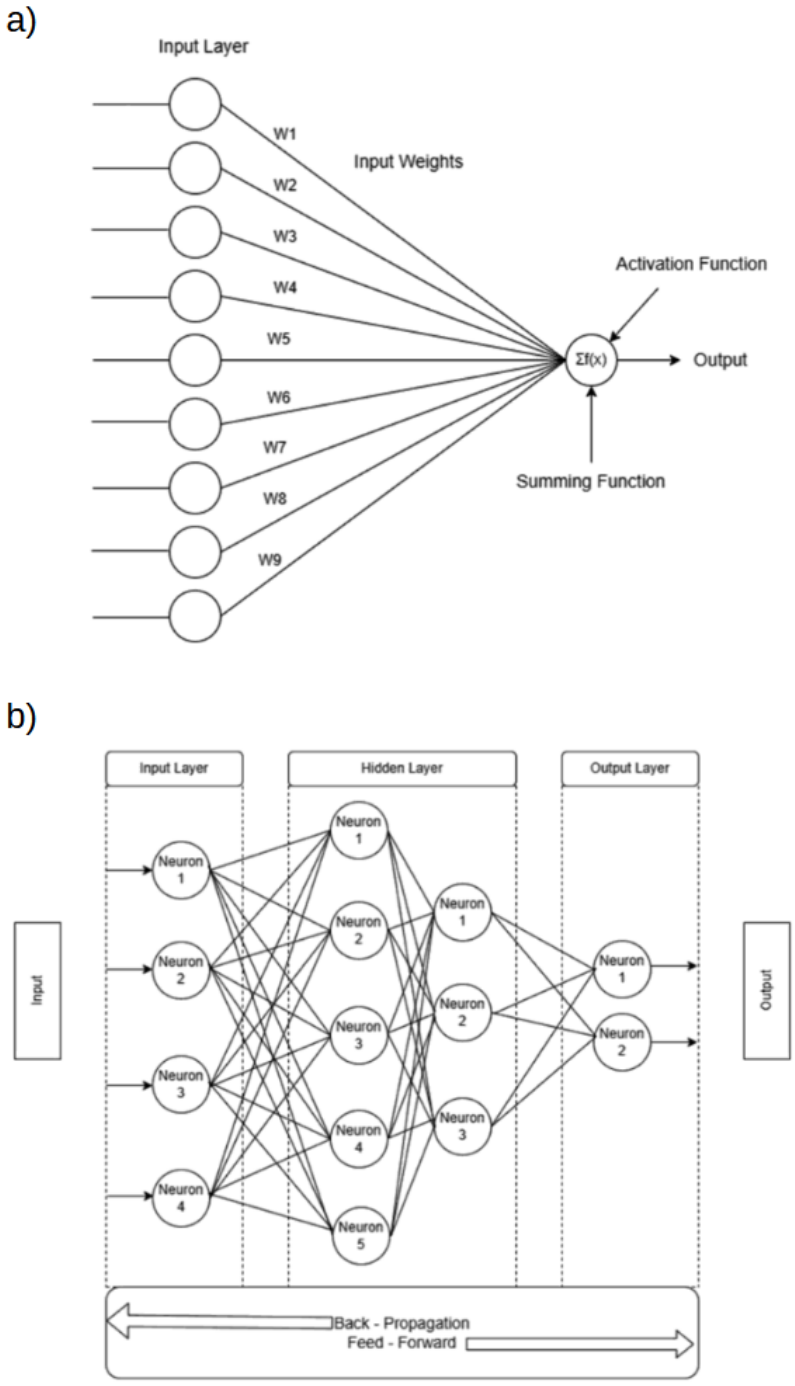

Figure 6: a) schematics of a perceptron, following the idea of Rosenblatt: Every input is associated with a tuneable synaptic weight. B) schematics of a DNN with two hidden layers. Adapted from [78].

Despite outstanding achievements of ANNs and DNN in particular, these models present a major drawback, namely the need to deal with an extremely high number of parameters. Modern models are often deliberately overparametrized, since a high number of parameters reveals to be beneficial for network learning abilities and performances [79]. Popular chatbots like ChatGPT, DeepSeek and Gemini are based on DNN architecture with hundred billions of parameters [74], [80]. Furthermore, processing large, unstructured datasets requires an extraordinarily high number of operations. These facts lead AI applications to be energetically extremely demanding. Training AI large models turns out to be the most expensive phase in term of energy and money, with cost for training new models increasing by a factor 2.4 per year during the last decade [81].

Nonetheless, in this period, AI is still experiencing a phase of explosive growth, driven by enormous investments from DC companies and the diffusion of commercially available AI tools, such as conversational generative chatbots [82]. Being the energy for inference significantly larger for AI with respect to traditional search engines (figure 7), the increasing popularity of these new tools is having a major impact over energy footprint of AI.

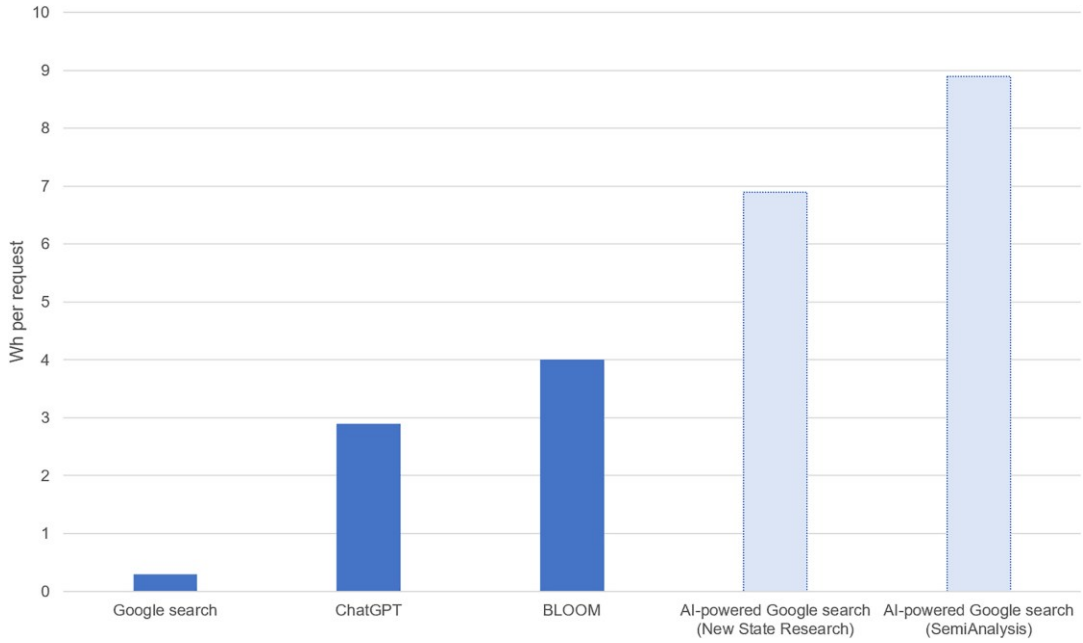

Figure 7: energy per request for AI based tools, compared to traditional search engine. From [8].

The rapid increase in computational demand has by far exceeded the improvements in hardware power efficiency: over the past decades, the power consumption of data centres has grown steadily, by about 1% per year [53], but, in the early 2020s this trend accelerated sharply, largely due to the large scale adoption of AI models (figure 8). Increasing concerns about environmental impact of AI led to the development of the new field of "Green AI", with the aim to provide energy efficient solutions to implement AI models [83].

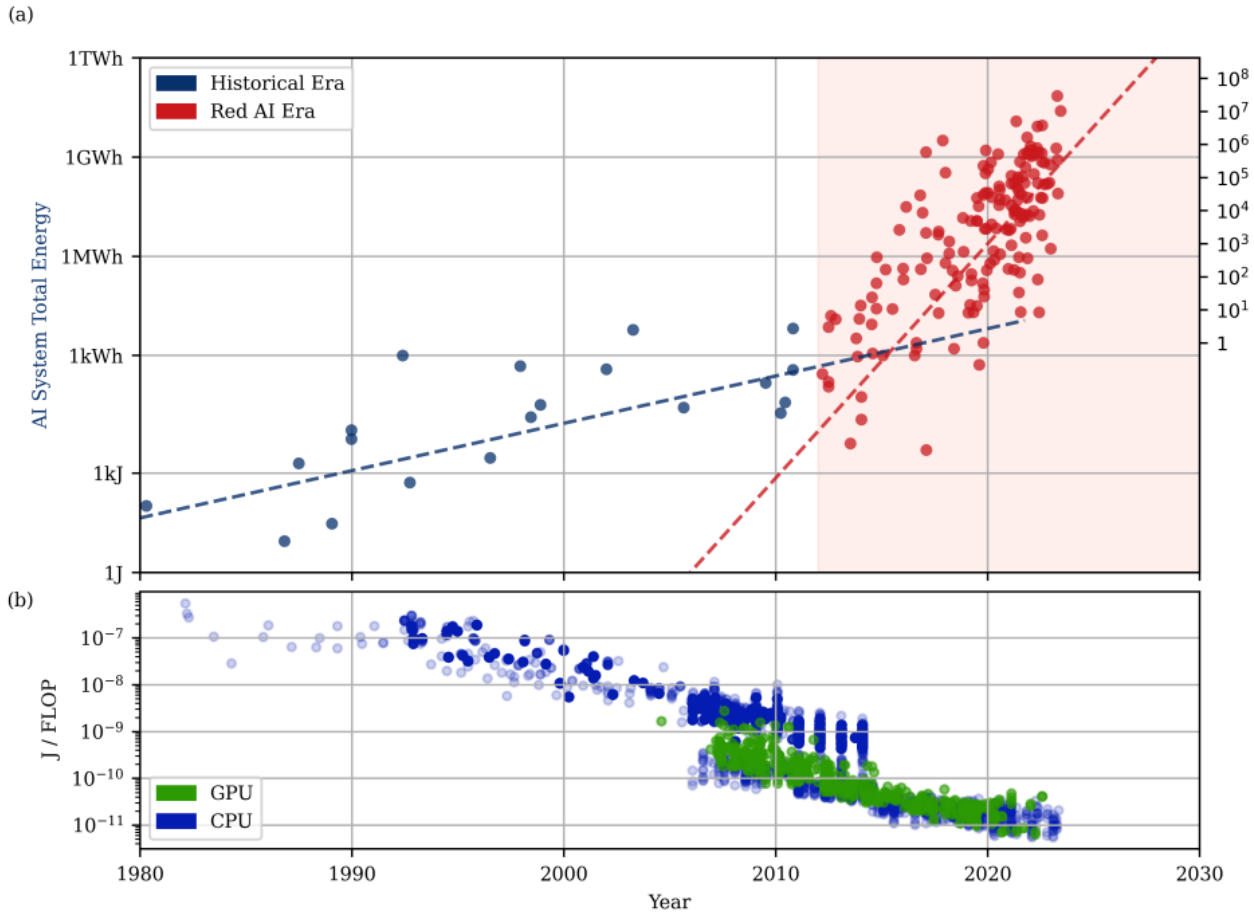

Figure 8: a) evolution over time of the energy consumption and corresponding carbon emission for training AI models. Carbon emissions have been evaluated according to the energy generation mix in the United States. B) evolution over time of the energy efficiency of CPU and GPU, expressed in energy per operation. From [84].

In summary, mainly due to the spreading of AI, and specifically deep models, computationally intensive tasks are no more bounded to few high-level applications but are becoming routinary for any user.

1.4 Neuromorphic computing

From the previous discussion, one crucial question remained unsolved. Even if, in recent times, we managed to reproduce some brain capabilities [85], we are still far from matching its power efficiency: the brain performs complex tasks using barely 20 W, i.e., its power efficiency is several orders of magnitude higher than modern supercomputers [86]. Surprisingly, brain outstanding abilities relies on a wet, noisy system, where neurons are three orders of magnitude bigger that transistors, and communicates with extremely low frequencies if compared with the clock speed of modern CPUs. This naturally raises the question about the origin of this efficiency. As I will discuss in this section, the structure and functionality of the brain is substantially different from that of a digital computer. This fact highlights that, despite being in principle able to compute all Turing computable functions (Turing himself present his model describing the work of a human

mathematician [13]), the brain *does not* work as a Turing machine [66], [87]. We often take for granted that computability must always be tied to programmability. This comes from the fact that we are used to think about computation in Turing's terms. However, the brain is a paradigmatic example of a system that performs tasks without any kind of symbolic abstraction. So, programmability is not a necessary requirement for something to be computable.

Is has been widely recognised that the achievement of efficient computing solutions requires the adoption of new computational paradigms beyond the traditional computing scheme. All the approaches that take inspiration from brain functioning go under the broad term *neuromorphic computing*. This broad research field comprises many different paradigms: recently, neuromorphic circuits based on standard CMOS technology has been designed specifically to emulate neurons functions [88]. On the contrary, other approaches aim to integrate novel devices that reproduces synaptic like features in CMOS circuitry [9], [79]. Beyond CMOS based approaches, recent studies have demonstrated that self-assembled networks of nano-objects can reproduce some key features of brain connectivity and emergent dynamics [10]. In the following paragraphs I present a brief overview of some of the most widely studied and promising strategies. For a more extensive discussion, the reader can refer to my publication, ref. [89].

1.4.1 In-memory computing

Carver Mead, one the pioneers of AI, addressed the issue of computational efficiency [57], and identified some key factors that are responsible for the gap between biological and digital systems: from energetical considerations, it becomes evident that most of the energy in digital computing is not used in the computation itself, but rather in charging the interconnects (this is one of the issues linked to the memory wall discussed previously). On the contrary, in biological neural networks the function of memory is implemented in the synapses, that are directly responsible of signal processing. In other words, both memory and processing are embedded in the network connectivity. This observation inspired the adoption of a new paradigm to overcome the limitation of the memory wall, and to implement more closely brain-inspired strategies. *In-memory computing* [79] refers specifically to all the strategies implementing the integration of memory and processing, i.e., enabling computing within the memory [90]. A widely studied approach relies in the exploitation of electronic components with synapse-like properties: memristors [91], [92]. A memristor (theorized by L. Chua in 1971 [93]) is a two terminal device whose resistance depends on some internal state variable, that be tuned by means of suited electrical stimuli [94]. The conduction state is retained over time, thus implementing the function of memory. These characteristics make memristors good candidates for both information storage and processing. Many different physical mechanisms can be exploited to implement this functionality. In [89] I present a brief overview of the state-of-the-art of memristor technology. In figure 9a the schematics of a filamentary memristor is shown. This device consists in a metal-insulator-metal structure. The application of a voltage pulses causes the destruction of a nanometric conductive filament across the insulating layer, thus

inducing the transition between a high resistance state and a low resistance state [95]. Reversible variations of electric resistance are generally referred as *Resistive Switching* (RS) phenomena (See section 2.2).

Memristive crossbar arrays (figure 9b) consist in two sets of parallel conductive lines perpendicular to each other, connected with memristors at each intersection [96], [97]. These devices can be exploited to perform efficiently vector matrix multiplications, thus being particularly suited for in-memory implementations of ANNs [98]. Furthermore, they enable highly parallel processing [99], and they also provide a platform for spiking-based computing devices (see [97] and references therein), thus reproducing dynamics that resemble those found in biological neural networks.

Critical issues in this framework, are nonidealities at the device level that can significantly degrade the performances of the circuits, especially in case of deep (multilayer) architectures [79].

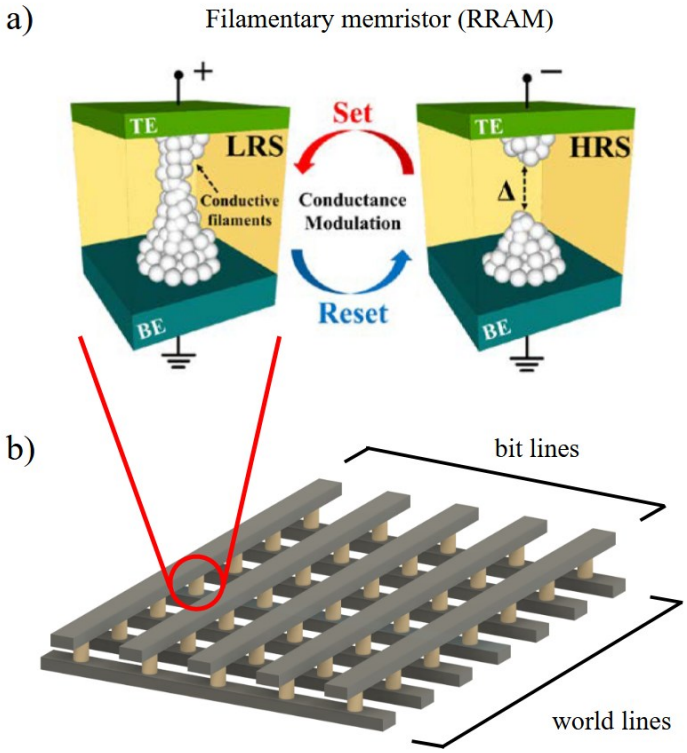

Figure 9: a) schematics of a filamentary memristor, adapted from [100]. B) memristor crossbar array, adapted from [89].

1.4.2 In-materia computing

In-memory computing solution described in the previous section are highly promising, since they capture some fundamental characteristics of biological neural networks. However, even in their spiking-based implementations, they are still far from replicating the mechanisms of the biological counterparts [66].

Embedding memory and computing is one of the major differences between brain structure and von Neumann architecture, but it is not the only one. The brain presents a complex connectivity based on redundant and multiscale neural circuits [89], [101]: efficient signal processing arises from the emergent behaviour of neurons in their peculiar structural self-organization [66]. These features cannot be reproduced in ordered and fully connected architectures such as memristive crossbar arrays. Interestingly, engineers of Hewlett Packard working on a pilot project named Teramac in 1990s, recognized the importance of wiring in retrieving robustness and efficient computing, highlighting the need to develop novel fabrication strategies to achieve functional complexity [102].

Exploitation of bottom-up fabrication approaches, in contrast with standard top-down microfabrication techniques, allows to easily produce self-assembled materials with complex topology that is needed to reach this goal.

In these physical systems, computational capabilities arise directly from the collective behaviour emerging from the interaction of fundamental components. Differently from DC approach, here, computing is not matter of mapping rules of first-order logic in some specific physical phenomena, but rather to exploit the physics of the system itself to perform data processing [103]. This computational paradigm is often referred to as *in-materia* computing. In this context, as should be evident, the distinction between software and hardware is completely meaningless [21].

Several physical substrates have been proposed as candidates to implement this approach. Among them, metallic nanoparticle networks near the percolation threshold (figure 10a) [104], [105] and beyond the percolation threshold (figure 10b) [106], [107], [108], and nanowire networks (figure 10c) [109], [110]. These systems self-organize in topologically complex networks of memristive elements, thus implementing both synaptic-like properties and neural-like topology.

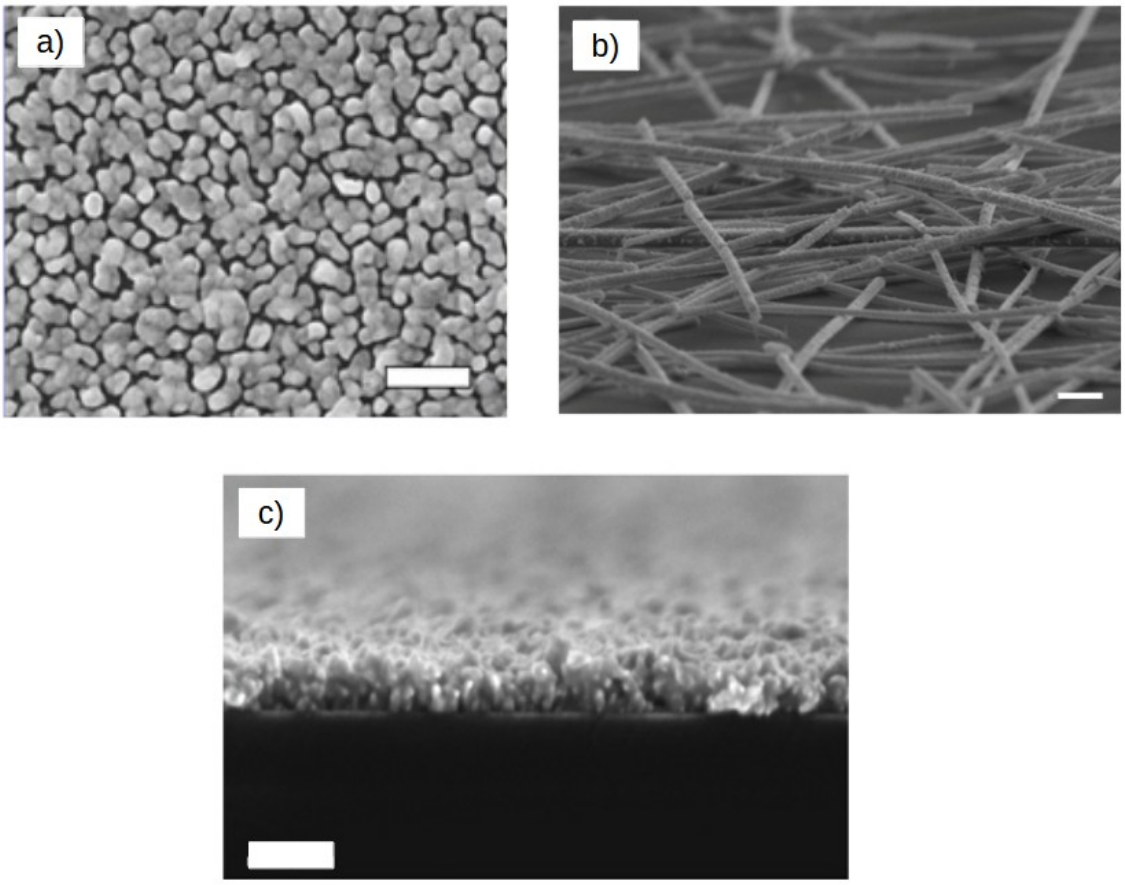

Figure 10: random-assembled nanostructured materials for neuromorphic computing applications. a) random assembled Sn nanoparticle network at the percolation threshold. Scalebar 200 nm, adapted from [105]. b) silver nanowire network, scalebar 500 nm, adapted from [111]. c) Au cluster assembled film. Scalebar 100 nm, adapted from [108].

In recent times, many different computing applications have been suggested based on self-assembled networks of nano-objects [10]. Thanks to their intrinsic complexity, recurrent connections, and emergent dynamics, these systems are particularly suited for *reservoir computing* (RC) applications. A RC system consists in a nonlinear recurrent network for project input in a high dimensional space, i.e., the reservoir, thus facilitating the classification task, that is carried out by a simple redout layer [112], [113]. The key advantage of RC is that it avoids the training of large and complex networks [114], since training is only limited to the readout layer. Within the framework of in-materia computing, the nanoscale assemblies, thanks to their self-organization and complex dynamics, are exploited in the role of reservoir. Feasibility of RC using nanowire networks as physical reservoir has been demonstrated [115], [116], [117]. Nanoparticle networks have been also successfully employed to address factorization problems [118] and for random number generation [119].

Metallic Cluster-Assembled Films (MCAFs) over percolation threshold are a promising physical substrate for neuromorphic computing applications [120], [121], [122]. They form a complex network of nanojunction exhibiting memory properties and a complex RS activity [106], [108], [123].

1.5 Implementation of Metal Cluster Assembled Film-based Receptrons

Recently, an MCAF based reconfigurable nonlinear threshold logic gate has been implemented [120], [121]: MCAF are fabricated on a substrate functionalized with electrodes (see section 2.2) that are used to provide inputs and retrieve an output from the device (figure 11). Boolean inputs are provided as low voltage stimuli (usually 0 V and 1 V). Electric current is measured at the output electrode, and the Boolean output is determined thorough a simple thresholding procedure [121]. This operation is referred as *reading*. If electrical stimuli are sufficiently high, MCAF undergoes structural modifications that affect the network connectivity, thus enabling the implementation of new functions. This second operation is referred as *writing.* In figure 11 is provided a schematic representation of the device operation: a first Boolean function is implemented (a). Then the system connectivity is modified by a suited electrical stimulus (b), and a new Boolean function can be retrieved (c). Thanks to the peculiar electrical characteristics of MCAFs discussed in the previous section, different current paths inside the network can effectively interact, thus implementing non-trivial data processing capabilities. In fact, this system has been shown to be always able to implement a complete subset of Boolean functions [124], and, notably, non-linearly separable ones.

This device finds a theoretical formalization in the *receptron* model [10], [125], [126]. The receptron (reservoir-perceptron) is a generalization of the perceptron (1.1) and presents input-dependent weight functions. I limit the discussion to the "digital" version of the receptron, i.e., receptron with Boolean inputs. Consider a device with n inputs, $\vec{x} = (x_1, \dots, x_n)$, with $x_j \in \{0,1\}\ \forall\ j$. A weighted sum is performed in analogy with (equation 1.1):

$$S = \sum_{j=1}^{n} x_j w_j(\vec{x}) \tag{1.2}$$

Where w_j are functions $w_j(\vec{x})$: $\mathbb{R}^n \to \mathbb{C}$, with the constraint $S(\vec{x})$: $\mathbb{R}^n \to \mathbb{R}$. The output of the device is obtained by means of a threshold function, as for the case of perceptron:

$$Y(x_1, \dots, x_n) = \Theta(S + b) \tag{1.3}$$

where b is a constant bias. The dependence of weight functions on the all the inputs means interacting inputs, leading to the classification of non-linearly separable functions [10]. It is also possible to show that the number of free parameters for the digital receptron with n Boolean inputs equals the number of different n inputs combinations [125]. This implies that by carefully tuning the model parameters, *all* the set of 2^{2^n} Boolean

functions with n inputs can be implemented. Thanks to high order terms that are not present in the perceptron model, receptron is able to implement non-linearly separable Boolean functions.

Hereafter, I will refer to the MCAF based receptron simply as *receptron*. Receptron *de facto* does not require training [121]: a sequence of write operations, each one carried out by randomly sorting one electrode couple and applied bias, are exploited to explore the space of configurations and find a specific target function [120], [121]. In case of an extremely large number of configurations, the random search turns out to be a suitable strategy to explore efficiently the state space of the system [10].

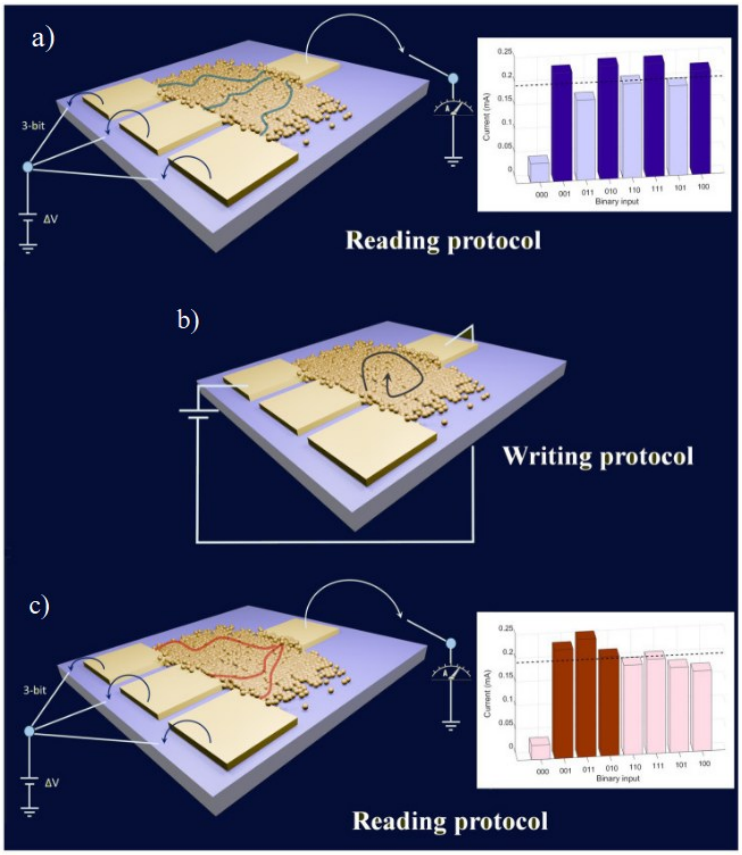

Figure 11: operation of MCAF based receptron. Adapted from [66].

Despite being the theoretical model completely general, not all the functions are equally likely to be implemented in a real device, with some of them that are rarely found during the random exploration of the state space. In [124], Martini exploited an architecture consisting in multiple receptrons connected in a configuration analogous to an Arithmetic Logic Unit (ALU) to improve the search protocol and to efficiently implement complex functionalities.

1.6 Objectives and Thesis outline

Despite the growing interest in neuromorphic computing applications based on random assembled materials and outstanding achievement in providing proof-of-concept of functional devices, we are still far from the realization of commercial devices based on this specific paradigm, for different reasons.

First of all, we still have poor insight in the physical mechanisms underlying RS phenomena. These mechanisms govern the emergent collective behaviour that is crucial for information processing, and their nature has been not fully clarified.

Secondly, systematic studies on the influence of geometrical parameters and electrode interfaces on network topology and electrical response are crucial to allow effective engineering of MCAF based devices, but they are still relatively scarce. Such investigations are essential to find the prospects for device scalability and, ultimately, for integration with standard CMOS electronics.

Finally, strategies aimed at optimizing electrical stimulation protocols, improving the reproducibility of electrical responses and efficiency in states space exploration are necessary.

Exploring all these aspects is essential to pave the way toward the engineering of MCAF-based devices that can be reliably designed, scaled, and employed in real life applications. In this thesis I will address these pivotal topics focusing both on fundamental physical mechanisms orchestrating complex RS behaviour in MCAFs and devices engineering possibilities.

Chapter 2 presents the experimental methods. Section 2.1 focuses on the integration MCAFs fabrication technique with standard microlithography for precise definition of deposit geometry. The choice of substrates is discussed in detail. Section 2.2 overviews the state of the art in MCAFs physics, with main reference to my paper ref. [108]. Section 2.3 presents the methods for MCAF characterization. In this work electric measurements are complemented by real time IR thermal imaging to map sample conduction. Finally, section 2.4 discusses the application of analytical tools developed in neuroscience for the analysis of RS in MCAFs.

Chapter 3 presents the main outcomes of the thesis. This section specifically refers to the results published in my paper ref. [127]. Section 3.1 discusses the possibility to exploit IR imaging for the characterization of the morphology and electric behaviour of MCAFs. Section 3.2 presents the results of electrical and thermal characterization of RS in two terminal devices, pointing out the influence of stimulus and geometrical parameters of the deposits. The presence of correlation and their tunability by acting over structural or stimuli parameters is discussed as well. Section 3.3 describes the response of MCAF to time varying stimuli, in view of engineering optimal stimulation protocols. Section 3.4 introduces the modelling of MCAFs response in multiterminal devices, with the aim to improve training processes for MCAFs-based receptrons.

2 Materials and methods

This chapter is organized as follow: in the first paragraph MCAF fabrication technique and the lithographic process for substate preparation will be presented. Then, follows an outline of the state-of-art on the electric properties of MCAFs, mainly focusing on resistive switching (RS) phenomena, that are key subjects in the next two chapters. Finally, an extensive overview of the experimental methods and statistical analysis used for electrical and thermal characterization will be provided.

2.1 Nanostructured metallic film fabrication

2.1.1 Supersonic Cluster Beam Deposition

The MCAFs where fabricated by means of a Supersonic Cluster Beam Deposition (SCBD) apparatus equipped with a Pulsed Microplasma Cluster Source (PMCS). In figure 12a a schematic of the apparatus is presented. The PMCS (see the inset in figure 1a) relies on the ablation of a target electrode by means of a confined plasma discharge [128], [129], [130]: an inert gas at high pressure (Ar in this work) is injected into a gold target by means of a pulsed valve. The gas is ionized by an electric discharge that is fired between the target, acting as the cathode, and an anode. The positive ions in the plasma hit the negatively charged target and mechanical ablation of Au atoms takes place. Thanks to aerodynamic confinement, in PMCS the plasma is highly localized, thus allowing the sputtering to be highly efficient and stable compared to other cluster sources [128], [131]. Gas acts as a heat bath for vaporized atoms, that condense to form clusters. The gas-cluster mixture is extracted from the source chamber by means of the pressure gradient established between the source and the expansion chambers (refer to figure 12a). Under specific pressure conditions and nozzle geometry (see [132] for further details) the gas expansion is supersonic. Aerodynamic focusing is performed after gas cluster mixture extraction [131], [133], [134]: a series of axisymmetric aerodynamic lenses allows to produce contractions and expansions of the gas stream following the original idea by Liu [135], [136] (see focuser in figure 12b-c). Nanoparticles are concentrated close to the axis of the focusing lens, and the outcoming seeded beam has low divergence [137]. Aerodynamic separation [134] allows to accomplish mass selection inside the focuser thanks to different inertia of the nanoparticles: massive ones do not follow carrier gas streamlines and are deposited on the walls of the focuser, while lighter ones effectively follows gas streamlines and are not concentrated on the axis on the focusing lenses. In order to deposit nanoparticles in supersonic regime, the focused beam is intercepted by a skimmer located in the zone of silence of the supersonic expansion at the focuser exit. This strategy allows to eliminate all the shock waves from the deposition chamber, and the small amount of gas passing thorough the skimmer allows to maintain high vacuum conditions. The substrates are mounted on a motorized sample holder equipped with a quartz microbalance. The substrates and the microbalance are alternatively exposed to the cluster beam for real-time monitoring the thickness of the film during deposition. One substrate functionalized with electrodes has been used to monitor the evolution of the electrical resistance

in situ during the film growth. To perform this characterization, a feedthrough flange has been employed to contact the substrate inside the deposition chamber with a multimeter located outside the apparatus. Real time measurement of the thickness and the electrical resistance provide two independent parameters to monitor MCAF growth.

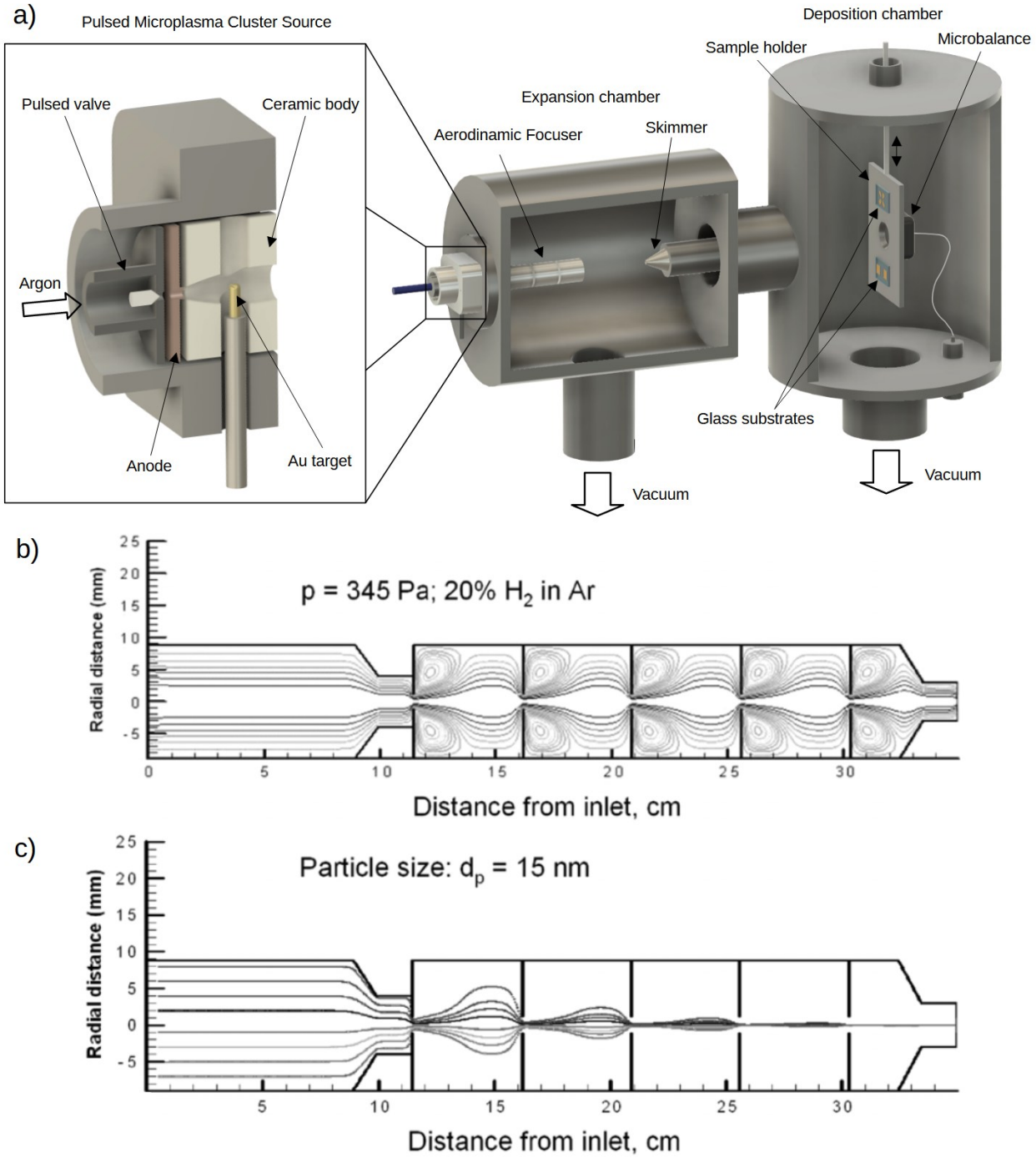

Figure 12: a) schematization of Supersonic Cluster Beam apparatus, and Pulsed Microplasma Cluster Source in the inset. B) gas flow streamlines and c) nanoparticles trajectories, inside the focuser, according to [137]. Figure b) and c) are adapted from [131].

2.1.2 Substrates

The choice of the substrate plays a crucial role in determining MCAF growth and electrical properties [107], [138], [139], [140]: for this reason, factors such as surface roughness, mechanical stiffness, chemical composition, and heat dissipation capability must be carefully tailored to both the specific application context and the desired electrical characteristics of MCAF.

I adopted borosilicate glass substrates covered with a 100 nm thick silicon oxide overlayer for easiness of future integration with standard integrated electronic circuitry, and for multiple important thermal properties that I am going to discuss in this paragraph.

In borosilicate glass, both glass transition temperature and softening temperature lie over 500 °C: for this reason, its operative temperature range is suitable to sustain electrical forming (see paragraph 2.2), when temperature of hundreds degrees Celsius can be reached [138]. Furthermore, this material is resilient to thermal shocks and present a low thermal expansion coefficient (between $3 \times 10^{-6}\ K^{-1}$ and $6 \times 10^{-6}\ K^{-1}$ at room temperature [141]), thus being particularly suited to avoid mechanical stress in the nanostructure and potential breakage when stitched to PCB for electrical characterization.

Borosilicate glass has low thermal conductivity ($\sim 1\ [W/Km]$) and low specific heat (~ 840 [J/g K]). The physical consequences of this fact become apparent writing down the heat equation [142]:

$$\rho c \frac{\partial T}{\partial t} - \nabla \cdot (k \nabla T) = Q \tag{2.1}$$

Where ρ is the material density, c the specific heat, k the thermal conductivity and $Q = Q(x, t)$ the heat source term. The specific heat modulates the transient term: materials with low specific heat are expected to undergo faster thermal transients to fulfil the equality. Similarly, the thermal conductivity modulates the diffusive term, so sharper thermal gradients are present in materials with low thermal conductivity [143].

We can easily observe these effects in our case study by solving the heat equation in a simple system, consisting in a portion of the substrate, heated up by a thin MCAF layer with round geometry (figure 13). The substrate is massive cube in thermal contact with a small cylindrical heat source, representing a portion of the nanostructure.

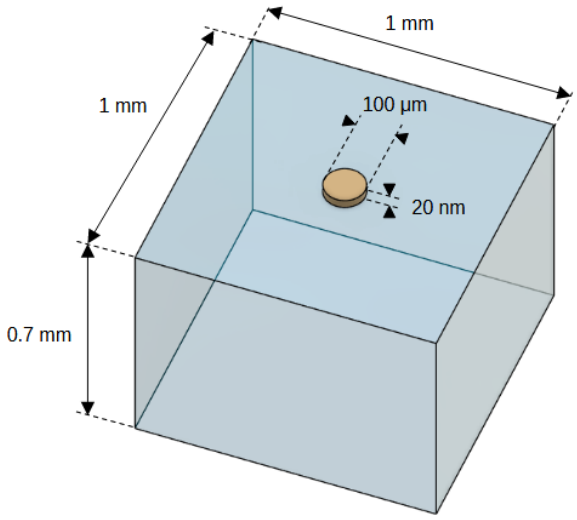

Figure 13: schematics of the domain for FEM thermal simulations. Blue: substrate, yellow: heat source.

Current flow in MCAF during electrical stimulation is responsible for joule heating. The source term in (1) is

$$Q = \tilde{\rho} j^2 \tag{2.2}$$

where $\tilde{\rho}$ is MCAF resistivity, and j the modulus of the current density. Here, we implicitly assumed that MCAF resistivity is isotropic. This assumption is physically reasonable, considering that current only flows parallel to the surface of the substrate, and the deposit is highly uniform in space, and, due to the large number of random oriented crystalline domains (see paragraph 2.2), no preferential directions are present on the microscale.

I adopted values for $\tilde{\rho}$ and j that have been reported in literature [138], [144], [145]. Current starts flowing at the instant t = 0 s and the source is heated up concurrently.

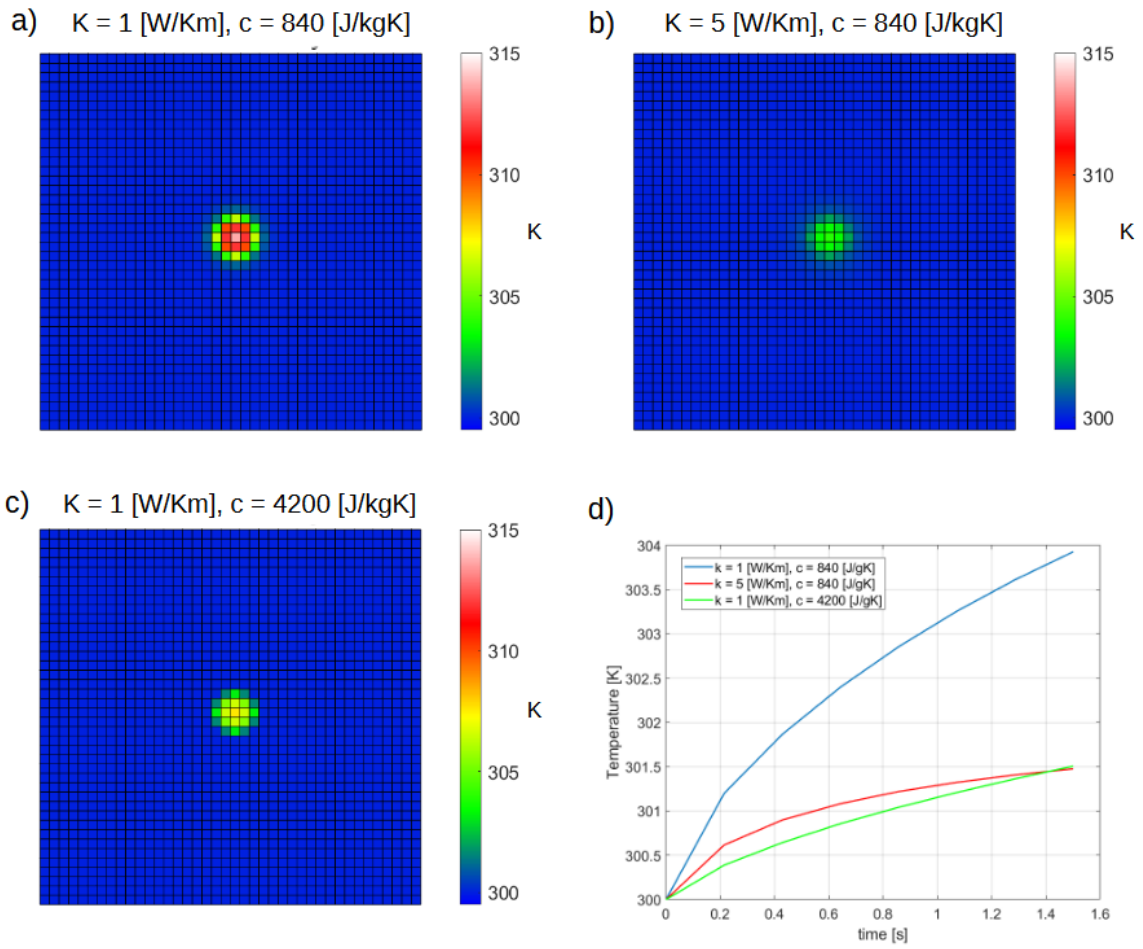

Figure 14: a-c) temperature profile on the substrate surface for three different combinations of specific heat and thermal conductivity (see labels in the figure), after 1.5 s from the start of heat production. Parameters used in a) corresponds to the glass's ones. d) thermal transients in the three cases presented in a-c).

Dirichlet boundary condition were applied on the bottom and sides of the cube (T = 300 K at the boundaries), while no heat is transferred through the upper surface (Neumann boundary condition with). I adopted MATLAB built-in partial differential equation (PDE) toolbox to find an approximate solution by means of Finite Element Method (FEM) [146]. In figure 14 a-c, I show the temperature along the surface of the cube at t = 1.5 s, for different values of specific heat and thermal conductivity of the material: in a) typical parameters for glass have been used, while in b) and c) thermal conductivity and specific heat has been increased respectively. In both b) and c) we observe substantially lower temperatures compared to a). In case b) heat diffuses rapidly through the material and it is effectively dissipated in the bulk and the boundaries. This effect leads also to a smoother temperature profile, with a less evident peak. In case c) a more pronounced peak is

still visible, but the temperature is low due to the highest amount of energy that needs to be provided to heat up the system. In figure 14.d I show the time evolution of temperature in a point of the surface located 6.5 μm from the boundary of the heat source. Both the systems with low specific heat (blue and red lines) present a sharp increase in temperature immediately after heat source activation. This means that the material closely "follows" temporal variation in Q(x,t). On the contrary, the material with high specific heat (green line) presents a slower increase in temperature.

In summary, low thermal conductivity and low specific heat allows to obtain both localized temperature peaks in correspondence to the location of the heat sources, and high temporal responsiveness. These aspects will turn out to be particularly important in the discussion of the microthermography based approach for Resistive Switching (RS) tracking (see next paragraph).

2.1.3 Microfabrication

As previously discussed in the Introduction, a central objective of this thesis is to investigate how MCAFs electrical response depends on their geometry, and to explore potential strategies for their microfabrication and integration with CMOS technology. For these reasons, I needed to establish a robust and reliable microfabrication approach, that is compatible with SCBD technique and allows to define the geometry of the nanoparticles deposit with high lateral resolution.

With respect to effusive sources, in SCBD the deposition is highly directional, and shadow masks can be exploited to obtain sufficient lateral resolution for most applications. However, the achievable resolution is still limited: in fact, , and distribution of cluster trajectories due to both cluster beam divergence and interactions between clusters and carrier gas [147]. by the non-zero distance between the mask and the substrate. For these reasons, it turns out to be challenging to achieve lateral resolution below $\sim 10\ \mu m$ by means of stencil masks.

I adopted standard microfabrication techniques [148] to deal with this issue and improve lateral resolution. A detailed description of the microfabrication process follows (see also figure 15 for reference).

Sample fabrication requires two lithographic steps, namely for electrodes and MCAF fabrication. JD Photo Data Grade 4 photomasks with $\sim 0.6\ \mu m$ tolerance over critical dimension have been employed for both processes.

- Electrodes consist in a $10\ nm$ thick Ti adhesion layer and $50\ nm$ thick Au layer deposited by means of magnetron sputtering (figure 15 II.-III.). The thickness of the Au layer was selected in order to obtain a square resistance sufficiently low with respect to MCAF, thus limiting series resistance during electrical stimulation: for a $50\ nm$ thick atom-assembled Au layer the square resistance is approximately 0.5 Ω, about three order of magnitude smaller than the square resistance of $20\ nm$ thick Au MCAF, which ranges between 100 Ω and 1000 Ω [145]. Electrodes geometry has been defined

according to standard UV photolithography technique [149]: positive photoresist (Fujifilm OIR 305-12) was applied, exposed and developed (figure 15 IV. – V.). Au and Ti were then removed by wet-chemical etching (figure 15 VI. – VII.). Plasma cleaning was employed to eliminate organic residues after the procedure.

- MCAF geometry was defined by means of lift-off procedure. Sacrificial photoresist mask was fabricated on top of electrode-glass surface (figure 15 IX.-X.). Negative photoresist (micro resist technology GmbH Ma-N1420) was adopted to obtain undercut profile [148] needed for lift-off. MCAFs were then fabricated by means of SCBD (figure 15 XI.), and, finally, lift-off was accomplished by means of acetone immersion (Figure 15 XII.). High purity isopropanol has been used to eliminate contaminants after lift-off completion.

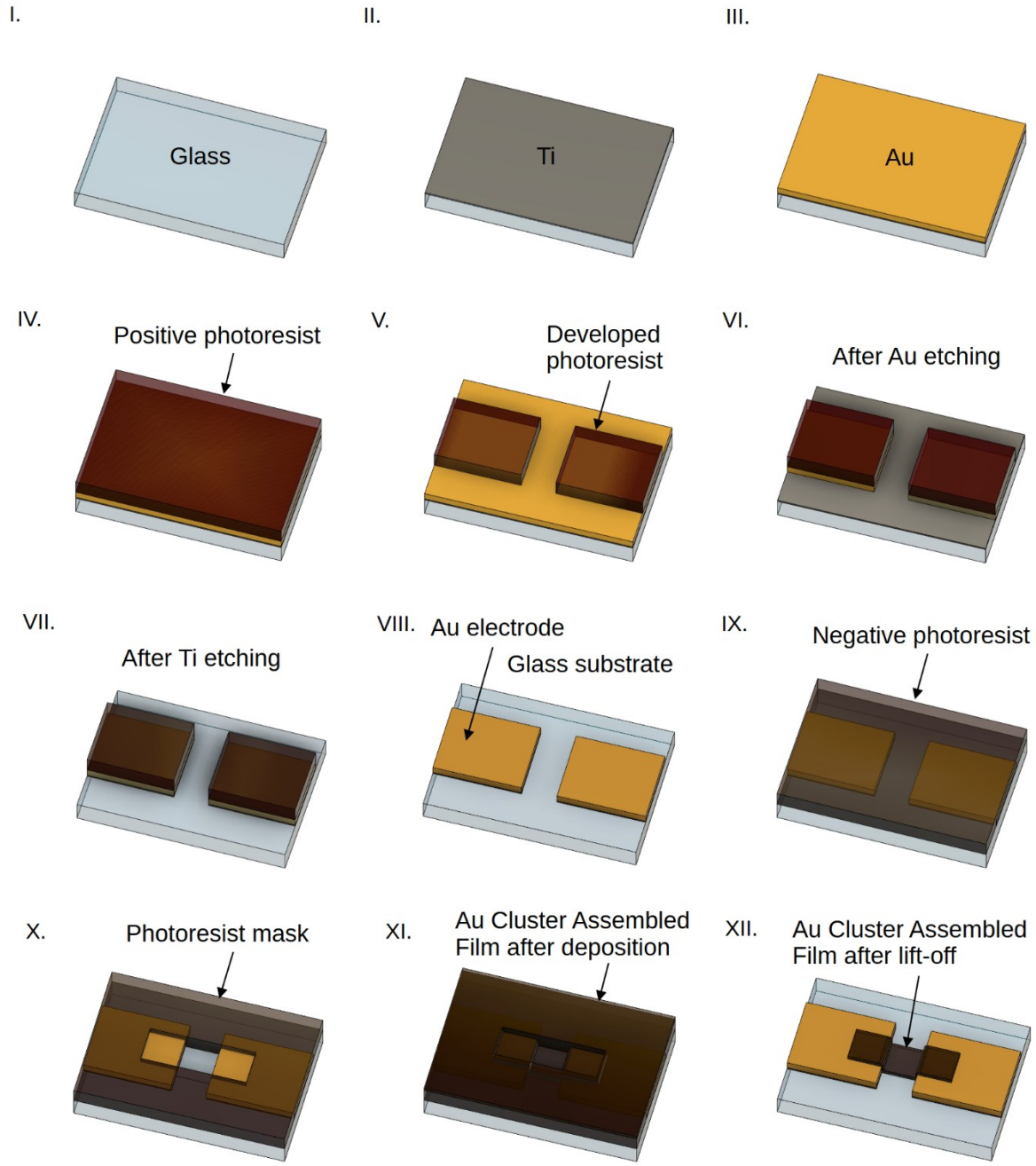

Figure 15: schematisation of the main steps in the microfabrication process. Ti and Au are deposited by means of magnetron sputtering (I.-III.). Photolithography (IV.-V.) and wet chemical etching (VI.-VIII.) are employed to define electrodes geometry. MCAF is microfabricated by SCBD and lift-off (IX.-XII.).

SCBD is particularly suited to be integrated with lift-off: high directionality in cluster deposition and ballistic growth allow to strongly limit film growth along photoresist undercut profile (see figure 16 and also [148]), thus minimizing the interference with the action of solvent also in case of thick (> 30 nm) deposit.

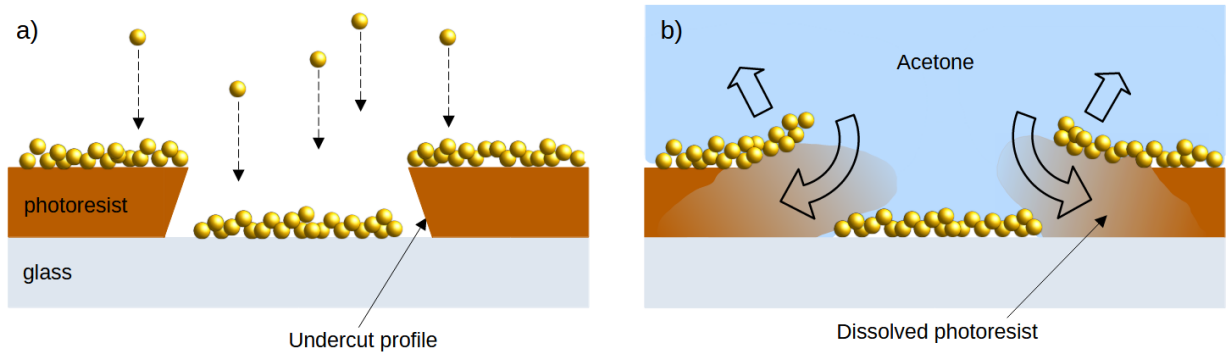

Figure 16: a) scheamtic representation of cluster deposition with a highly directional beam. The undercut profile of the photoresist is left uncovered. b) during acetone immersion, the solvent easily diffuses over the uncovered surface and dissolve photoresist, leading to MCAF lift-off.

Along with higher (micrometric) lateral resolution, integrating MCAF fabrication in lithographic process allows to obtain optimal alignment between MCAF and electrodes. After MCAF fabrication, the substrates were integrated into a PCB for electrical characterization. Wire bonding [150], [151], [152] has been employed for contacting electrodes with pads on the PCB.

2.2 Structural and electrical properties of MCAF

The size of the clusters deposited according to the technique presented in paragraph 2.1, present a bimodal distribution with two main peaks roughly at 6 nm and 0.5 nm [144], [145]. MCAF growth can be described by means of percolation theory [153], [154]: in the early stages of deposition, only few aggregates are present on the substrate, forming separate islands, and MCAF is effectively insulating. When a certain critical coverage is reached, namely, the system is at the percolation threshold, continuous conductive paths start to form through the sample, leading to an abrupt drop in resistivity that follows a power law dependence respect to coverage. During the last stages of the deposition the substrate is almost fully covered, 3D growth takes place, and a fully connected film is formed.

Clusters kinetic energy during deposition is less than cluster cohesive energy, so clusters retain their individuality and the porosity is almost independent from the thickness [155] (figure 17a-b). Island coalescence can take place only in the early stages of fabrication, and ballistic deposition model reliably describes film growth for high coverage [156]. As a consequence, the density [157] and resistivity [144], [145], [158] of MCAFs are substantially different from bulk or atom assembled counterparts. Clusters stability against coalescence has reported also for samples with high coverage (figure 17c), and allows to obtain an extremely high density of grain boundaries and defects [159], as clearly highlighted by means of HRTEM imaging (figure 17d).

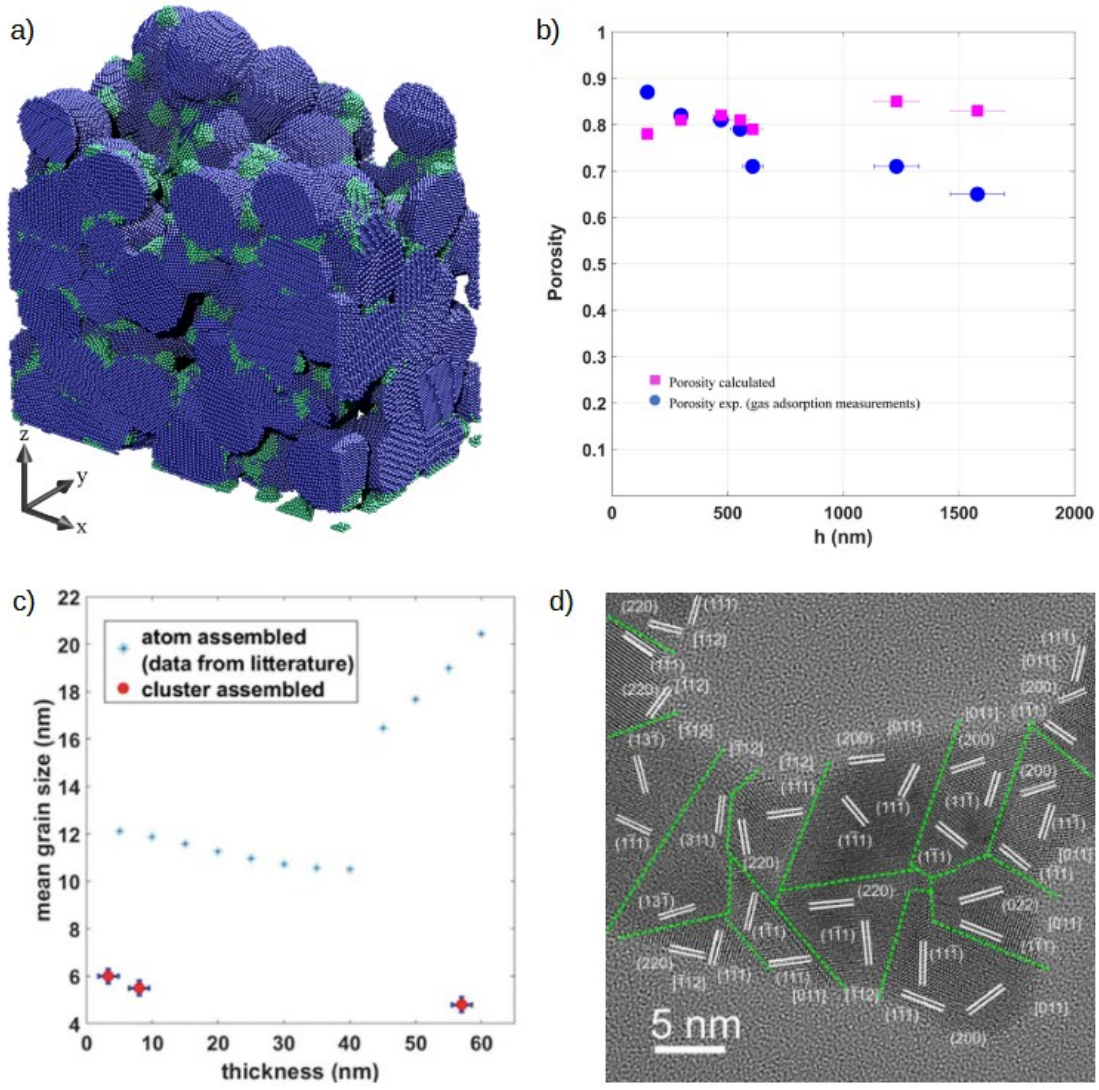

Figure 17: a) final state of molecular dynamics simulation of cluster deposition, from ref [160]. Different colours represent nanoparticles of different size. b) measured porosity, from [155]. c) evolution of mean grain size with film thickness for atom assembled films and cluster assembled films [159]. d) HRTEM image of a sub-monolayer MCAF. Crystalline domains, separated by grain boundaries are easily detectable [123].

These features strongly affect the conduction properties of MCAFs [123], [161]. As deposited MCAFs beyond the percolation threshold show ohmic conduction at room temperature [138], [159]. However, if sufficiently intense electrical stimuli are provided, MCAFs undergo electrical-thermal driven structural modifications[1] [145], [163], [164], [165], [166], that can be characterized by morphological study (figure 18a). In particular, most ohmic connections are broken via joule heating enhanced electromigration and dewetting. This process is referred as *electrical forming*. At this stage, strongly nonlinear conduction properties arise [123], [145], as

[1] A complete formalization of the effects of electrical and thermal induced stresses in solids can be found in [162].

different conduction mechanisms start to be dominant, [123], [167], such as space charge limited current (SCLC) mechanisms and coulomb blockade. Furthermore, MCAFs present the ability to undergo reversible structural modifications, that are responsible for variations in their electrical resistance. This phenomenon is referred to as Resistive Switching (RS) [106], [107], [145], [108], [144], [138]. RS has been found and characterized in similar nanostructured systems, such as embedded nanoparticles and nanowire networks [105], [168], [169], [170], but, interestingly, it was reported for the first time by the group of P. Milani to take place in bare metallic nanostructures [159]. RS in MCAF is linked to local modifications in electrical connectivity between different regions of the nanostructure, i.e., the formation and destruction of conductive paths, physically originating from thermal assisted defect annealing, electromigration and atomic rearrangement at grain boundaries. We have suggested the formation of local hot spots that catalyse these processes in a previous study [108].

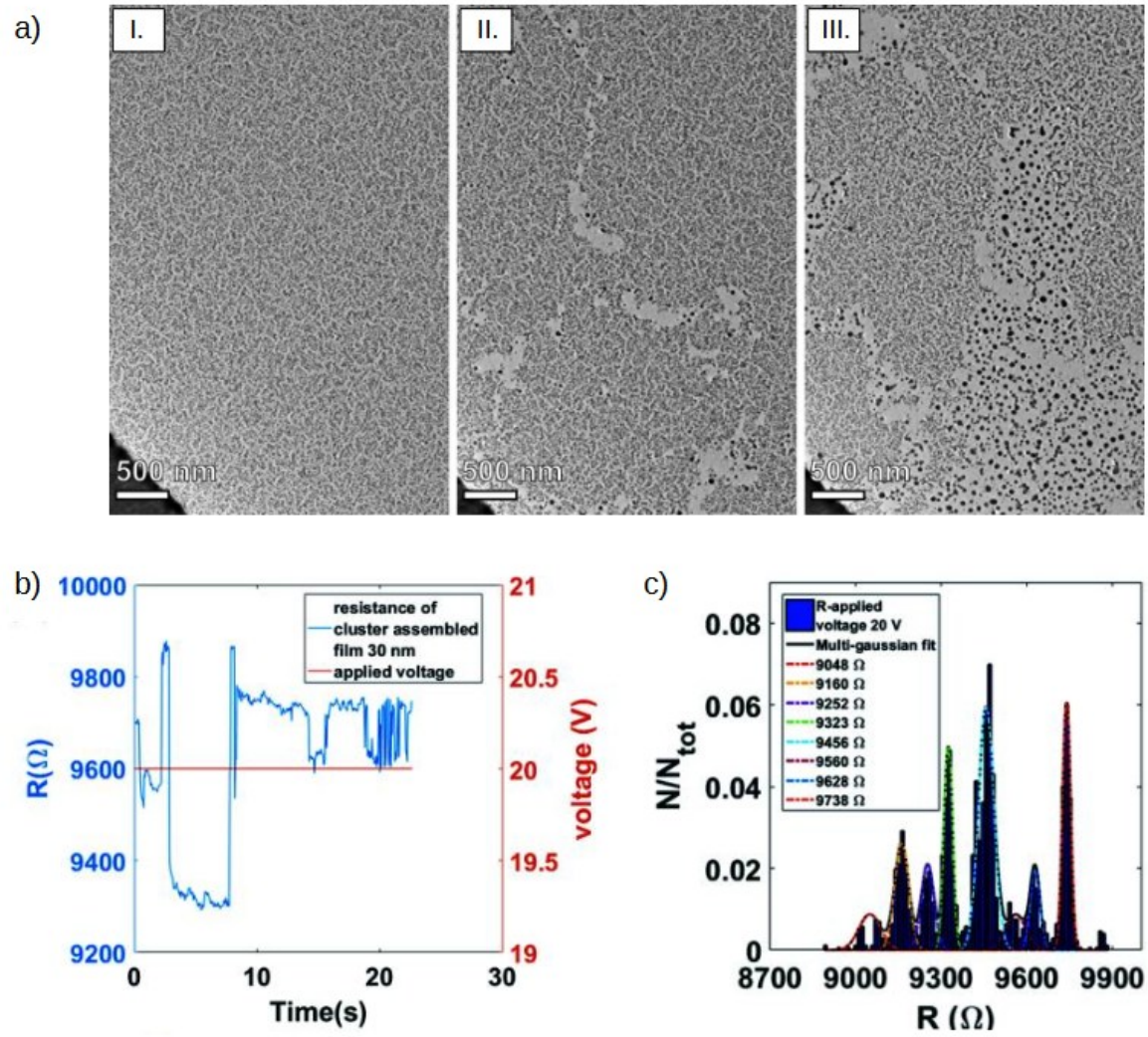

Figure 18: a) TEM images showing the evolution of MCAF morphology after biasing at 20 V (I.) and 30 V (II.). Dewetting phenomena [171] are clearly visible and are responsible for the formation of islands in (III.). Adapted from [166]. B) resistive switching phenomena during electrical stimulation of MCAF at constant bias, from [145] C) normalized distribution of resistances during biasing. Multiple discrete resistance levels are explored, from [145].

In order to trigger RS, there is the need to induce structural modifications, i.e., it is necessary to provide sufficient energy to overcome a potential barrier and drive the system away from a (local) energy minimum. For this reason, RS turns out to be a threshold activated phenomenon, that can be triggered only if sufficient power is provided by means of electrical stimulation. If this is the case, RS events are triggered, and the system undergoes a spontaneous and continuous dynamical evolution as long as energy is supplied. In figure 19a I show the time evolution of the electrical resistance during a stimulation with constant voltage bias. Abrupt variations in the resistance time series due to RS events are immediately detectable. Interestingly, resistance

variations induced by RS do not span a continuum. Instead, it is common to observe the exploration of a limited set of resistive states, suggesting the recurrent disruption and restoration of *specific* structural configurations over time. The distribution of the resistances measured during biasing is displayed in figure 18d. It turns out to be the convolution of a finite set of gaussians, and the peaks corresponds to the resistance levels explored.

In a recent paper, I also characterized the temporal statistics of RS in MCAF, showing the presence of strong temporal correlations[ref]. This phenomenology is highlighted in the distribution of the time intervals between consecutive events, namely the Inter Switch Intervals (ISI). If events were generated by means of a Poisson process, i.e., independently from each other, and with uniform probability in time, ISI distribution would exhibit a purely exponential decay. However, ISI distributions displayed by MCAF are heavy tailed, and present a power law decay. This evidence indicates that RS events are likely to trigger subsequent events, leading to bursts of activity separated by comparatively long periods of quiescence. This effect can be also appreciated by performing a statistical analysis similar to the one suggested by Karsai et al. in [172]. In figure 19b I plot the normalized occurrences of RS events in a sliding time window of duration Δt. Dashed lines represent the same analysis performed over a fictitious time series generated by means of a Poisson process. Distributions retrieved from experimental data are one again fat tailed, as a consequence of the presence of bursting activity.

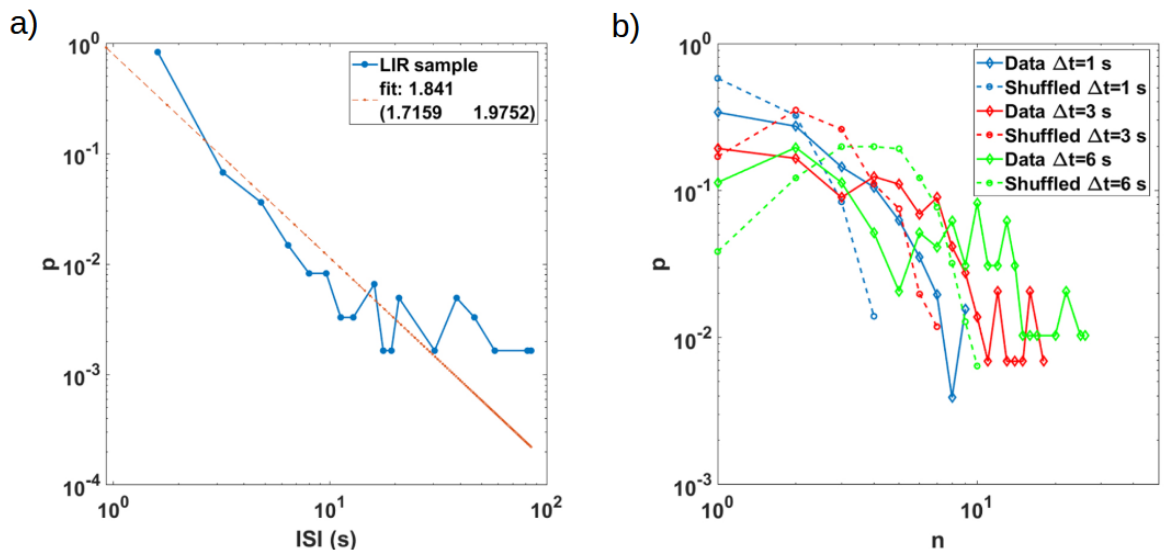

Figure 19: a) ISI distribution from a 20 minutes long stimulation with constant bias (5 V). Notice that both axes are in logarithmic scale. The linear fit highlights the presence of a power law trend. b) correlation analysis . Figures adapted from [108].

Analogue temporal dynamics have been already reported in other classes of nanostructured materials [104], [105], [173]. These characteristics are of particular interest since similar phenomenology has been observed in

the spontaneous spiking activity of biological neural networks [174] (see also the Introduction). In these biological systems, avalanches of spiking activity and scale invariance emerge from collective operating near critical regime. These properties have been suggested to be one of the principal ingredients for optimal signal processing in the brain [175], [176], [177].

MCAFs, as well as other aforementioned nanostructured systems [105], [109], [168], [169], [170] present other strong similarities with biological neural networks. They are a topologically complex network of interacting memristive nanojunctions, with small-world characteristics [178].

Noteworthy, in view of neuromorphic computing applications, key synaptic like behaviours has been already recognized in MCAFs, namely potentiation and depression capabilities [106], [108], [179] and long term temporal correlations [180].

2.3 Experimental methods

2.3.1 Electrical characterization

Electrical characterization was performed by means of a Keithley 2600 series Source Measure Unit (SMU) [181]. This instrument allows to perform voltage biasing up to $20\ V$ to with a programming resolution $< 1\ mV$ and accuracy $0.02\% + 12\ mV$. Current measurements can be performed with high resolution, namely down to $100\ pA$. The time resolution is limited by the extremely accurate readout circuitry, namely an integrating ADC. Resolution in current readings could be limited, or some artifacts could rise, due to the need for long integration times, or by the presence of artifacts due to measurements performed in different phases of the AC power line. We limited the sampling frequency to 20 Hz, with an integration time equal to one Power Line Cycle (PLC), to avoid these limitations to current resolution. Current measurements have been performed in automatic range selection mode, whenever possible. Namely, the range of the ADC has been selected by the instrument itself by fast scanning of the available measurement ranges. This procedure allows the current to be measured with the maximum resolution allowed by the instrument, depending on the present conduction state of the sample.

Different stimulation and measurement protocols have been employed in this work. Constant voltage stimulations consist in the application of a constant bias for a defined duration and measuring electrical current concurrently. Under the application of a constant bias, MCAFs conduction evolve in time, and display RS activity (see paragraph 2.2). This type of characterization allows to monitor the spontaneous evolution of MCAF and study the statistical properties of RS. Stimulation using voltage pulses have been performed as well. In this case, a sequence of rectangular voltage pulses has been applied to trigger RS phenomena and modify the conduction state of the system. Short constant voltage stimulations with low bias are usually

performed immediately after each pulse train to monitor the conduction state of the sample without triggering further RS events. This experimental protocol resembles the electrical reconfiguration process in actual devices [124], i.e., a fast, high voltage stimulation is performed to trigger RS and drive the device in the desired conduction configuration, while low amplitude voltage signals are used for computing operations. Following [120], [121], [124], I will refer to these two protocols as "write" and "read" operations, respectively. Automatic range selection, comprising the scanning of the measurement ranges, is not possible during pulsed measurements due to the need to precisely control time delays between voltage rise, the start of the measurement, and voltage fall. However, automatic range selection is always performed during read operations to ensure highest possible accuracy.

Keithley 2600 is not a pulse generator, and the resolution on the rise-fall time is limited to hundreds of microseconds. In our experiments, we performed stimulations with minimum pulse duration of 100 ms, so this instrumental uncertainty is negligible.

Some of microfabricated samples exhibit low electrical resistance before forming. In particular, the ones with small electrode spacing ($125\ \mu m$), typically present a resistance in the order of few Ω. In these cases, sample resistance is comparable with lead resistance due to wiring and connections, resulting in consistent voltage drop across the external circuitry, and causing uncontrollable stimulations. For this reason, electrical stimulations were performed by means of four-point probe setup (see figure 20a): SMU generates a current bias, and voltage drop across the sample is measured by means of Sense probes, that present high series resistance. A feedback loop allows to continuously adjust the current in order to keep the desired bias across the sample.

For the characterization of multiterminal MCAFs, the SMU is connected to a relay switch matrix controlled by a microcontroller Arduino Uno, that allows to selectively connects each terminal to high voltage or ground (figure 20b).

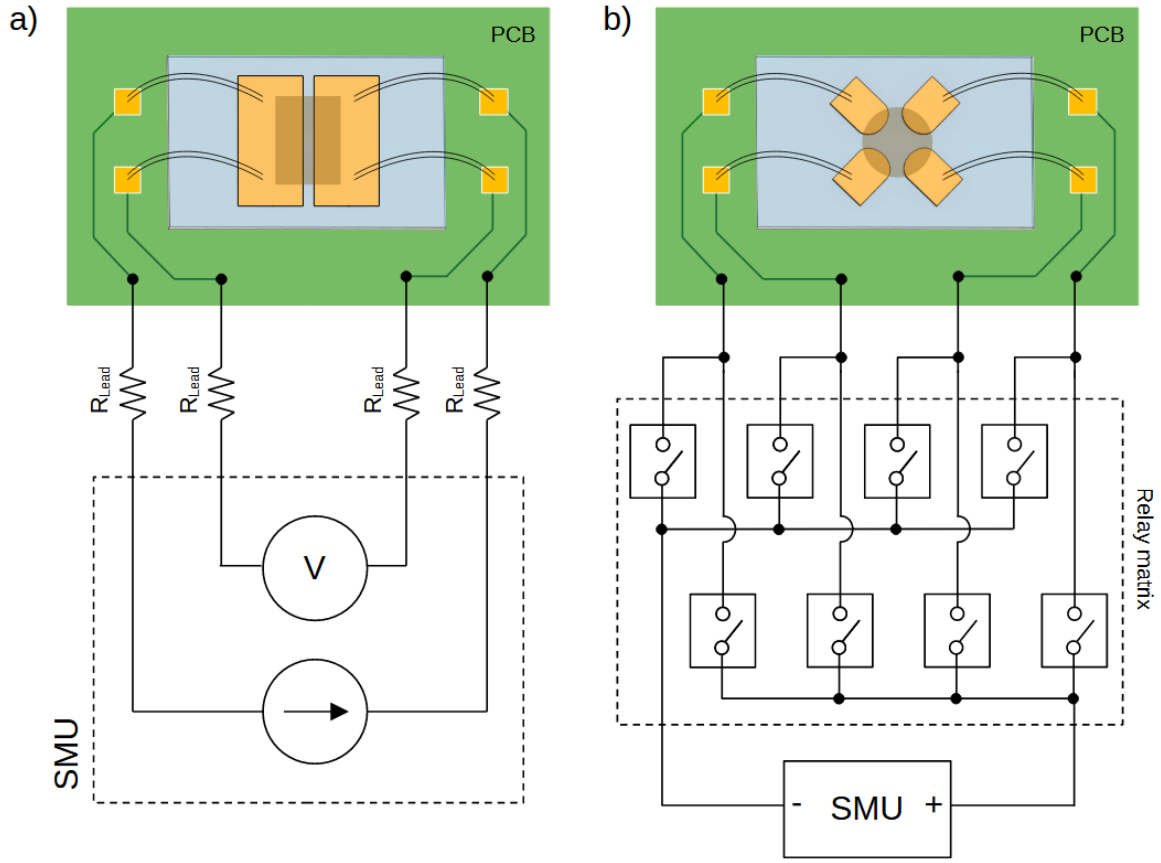

Figure 20: a) schematics of four point probe measurement. Voltage is measured with high series impedance through a couple of sense electrodes. The internal feedback adjusts the current source in order to keep the voltage bias constant. B) setup for multiterminal device characterization. Each electrode can be short-circuited with both the high and low voltage terminals.

2.3.2 Imaging by means of IR-microthermography

Different imaging techniques have been shown to be suited to obtain insight on RS in different nanostructured systems. In particular, structural modification induced by RS phenomena can be detected by means of different electron microscopy-based techniques: direct imaging of the nanostructure is possible by means of a Transmission Electron Microscope (TEM) [166], and Scanning Electron Microscope (SEM) can be effectively employed to map sample conductivity by means of Voltage Contrast (VC) techniques [170], [182]. These techniques allow to obtain detailed images of the evolution of the nanostructure with sub nanometric resolution. However, they also present some important drawbacks. First of all, measurements should not be performed in standard (atmospheric) conditions. This can influence the conduction properties of the samples and have strong impact on devices functioning [138]. Usage of TEM also poses severe limitations on the physical characteristics of the substrates: in particular, low thickness due to the need for electron transparency

(along with high vacuum environment) leads to poor heat dissipation capabilities (see the discussion paragraph 2.1). Another mayor drawback in all the aforementioned imaging techniques, is the risk to perturb the inspected nanostructure, due to the high energy probe beam. Field of View (FOV) is also limited at higher magnification, allowing to finely inspect nano-micrometric regions, but losing the ability to resolve collective RS dynamics taking place on broader scales.

The group of G. Milano recently developed an imaging technique that overcome some of these difficulties, and that was proven to reliably monitor the evolution of the resistivity in nanowire networks [183], [184]. This technique uses multi electrode arrays for four point probe trans resistance measurement at the deposit border, and reconstructs electric resistivity on a discrete mesh by means of Electrical Resistance Tomography (ERT) algorithm [185], [186]. One main limitation of the technique is the achievable spatial resolution, that strongly depends on the number of electrodes and distance from the border.

IR-thermography has proven to be a valuable alternative imaging technique for real time monitoring the conduction in MCAF and constitutes one of the main subjects of the present work. In particular, the term *Microthermography* (or *micro-thermography*) refers to all the IR-thermography techniques that allow to perform thermal imaging with micrometric resolution. These techniques are well developed and routinely used in semiconductor industry for chip quality control. The typical setup for microthermographic measurement consists in a thermal camera mounted on a PCB probe station similarly to [187], [188], and a SMU for electrical stimulation and measurements.

IR microthermography presents some key advantages with respect to the other aforementioned techniques, that make it particularly suited for our case of study: first, it is completely non-perturbative. In fact, it relies on the detection of IR thermal radiation that is naturally emitted due to joule heating. The Field of View (FOV), in the order of square centimetres, or square millimetres, for highest magnification, is sufficient to effectively image collective dynamics in extended (and complex) systems. Temporal resolution is mainly limited by substrate thermal responsiveness (see the discussion in the following paragraphs), but in principle it can be in the order of milliseconds or less. Good temporal resolution makes IR-thermography extremely appealing for real time monitoring the dynamical evolution of electrical conduction. Furthermore, thermal cameras allow to operate in atmospheric condition, or even in specific controlled environmental conditions. The only physical requirement for the nanostructure/substrate is to have sufficiently high emissivity (see the discussion in the following paragraphs). This requirement is almost always met due to the usage of electrically insulating substrates that are generally very good emitters. The main drawback of microthermography is the poor spatial resolution, that is diffraction limited to $\sim 2\ \mu m$ for high grade science cameras.

Sannicolo et al., and Li et al., already exploited microthermography [189], [190] to map conduction in nanoparticles and nanowires networks. In particular, they characterized the sample conductivity in steady state conditions, by means of lock-in thermography [191], [192], demonstrating measurement feasibility and being able to image conductive paths with micrometric resolution. However, the employment of lock-in

amplification, despite being beneficial to increase temperature resolution, strongly limits the achievable temporal resolution, thus making studies on temporal dynamics almost completely unfeasible. In this work we will demonstrate that, in most cases, RS spatial and temporal dynamics in MCAF can be characterized as well as steady state conduction, by standard microthermographic measurements, with no need of further sensitivity improvements. Later on, we will show that microthermography also offers information about morphology of the nanostructure.

In the following paragraph, I concisely review the fundamental concepts of IR thermography, complementing the discussion with important remarks tailored on our specific application.

Two main types of IR sensors exist, namely, photon detectors and thermal detectors [193], [194]. In photon detectors IR radiation is absorbed and causes changes electronic energy distribution in the detector material [194]. This effect can be achieved through different physical mechanisms, a common example being the generation of photocurrent in a narrow-bandgap semiconductor (photodiode). IR photon detectors present a major drawback: they need to be cryogenically cooled to prevent the thermal generation of charge carriers. However, they show fast response, allowing to perform thermal imaging with high framerate ($> 1\ kHz$). Photon detectors are typically used in the Mid Wave Infrared (MWIR) or Short-Wave Infrared (SWIR) spectral ranges.

In thermal detectors, the absorption of IR radiation causes an increment in detector temperature. This results in the change of some physical property of the material, that serves as sensor readout. Since late ‘90s, microbolometers are the most popular thermal sensor in IR cameras and exploit temperature dependence of resistivity for this purpose [195], [196]: when the sensor is heated up by IR radiation, the change in electrical resistance is detected by the readout circuitry. Respect to photon detectors, the frame rate is limited to roughly $100\ Hz$ due to the relatively slow thermal transient. Microbolometers popularity is mainly due to their affordability with respect to photon detectors, along with their excellent performances for most applications. Microbolometers are responsive in the Long Wave Infrared (LWIR) spectrum.

IR detectors are characterized by their responsivity, defined as the ratio between total output signal (voltage or current in case of microbolometers) and radiant power hitting the surface of the sensor:

$$R_v = \frac{V_s}{P_{BB}} \tag{2.3}$$

Noise Equivalent Power (NEP) is a fundamental parameter that quantifies the performance of the detector, and is defined as the amount of input power required to generate a signal to noise ratio equal to unity [195], [197]. It can be expressed in terms of responsivity:

$$NEP = \frac{v_s}{R_v} \tag{2.4}$$

The Noise Equivalent Temperature Difference (NETD) is defined as the minimum temperature difference giving a radiant power difference equal to the NEP [192]:

$$NETD = \left(\frac{\partial P_{BB}}{\partial T_{BB}}\right)^{-1} NEP \tag{2.5}$$

NETD is the most common metric for IR detector sensitivity and depends on physical and constructive parameters of both detector and optics.

Other than the aforementioned lower integration time, photon detector generally presents higher thermal sensitivity (down to $NETD \sim 10\ mK$) with respect to thermal detectors ($NETD \sim 30\ mK$). However, the choice of the detector should consider also the specific imaging applications. In particular, one crucial aspect is detector spectral responsivity. For this reason, I will briefly review some important concepts of thermal radiation.

Spectral radiance of blackbodies is described by the well-known Planck law [198], [199]:

$$L(\lambda, T)d\lambda = \frac{2hc^2}{\lambda^5} \frac{1}{e^{hc/(\lambda kT)} - 1} d\lambda \tag{2.6}$$

where h is the Planck constant, c is the speed of light in vacuum, and k is the Boltzmann constant. The blackbody spectrum presents a peak in correspondence to a specific wavelength λ_{max} that is linked to the temperature of the material by the Wien displacement law [192], [200]:

$$\lambda_{max} T = 2897.8\ \mu mK \tag{2.7}$$

The dependence of the peak of the blackbody spectrum over temperature is schematically presented in figure 21b.

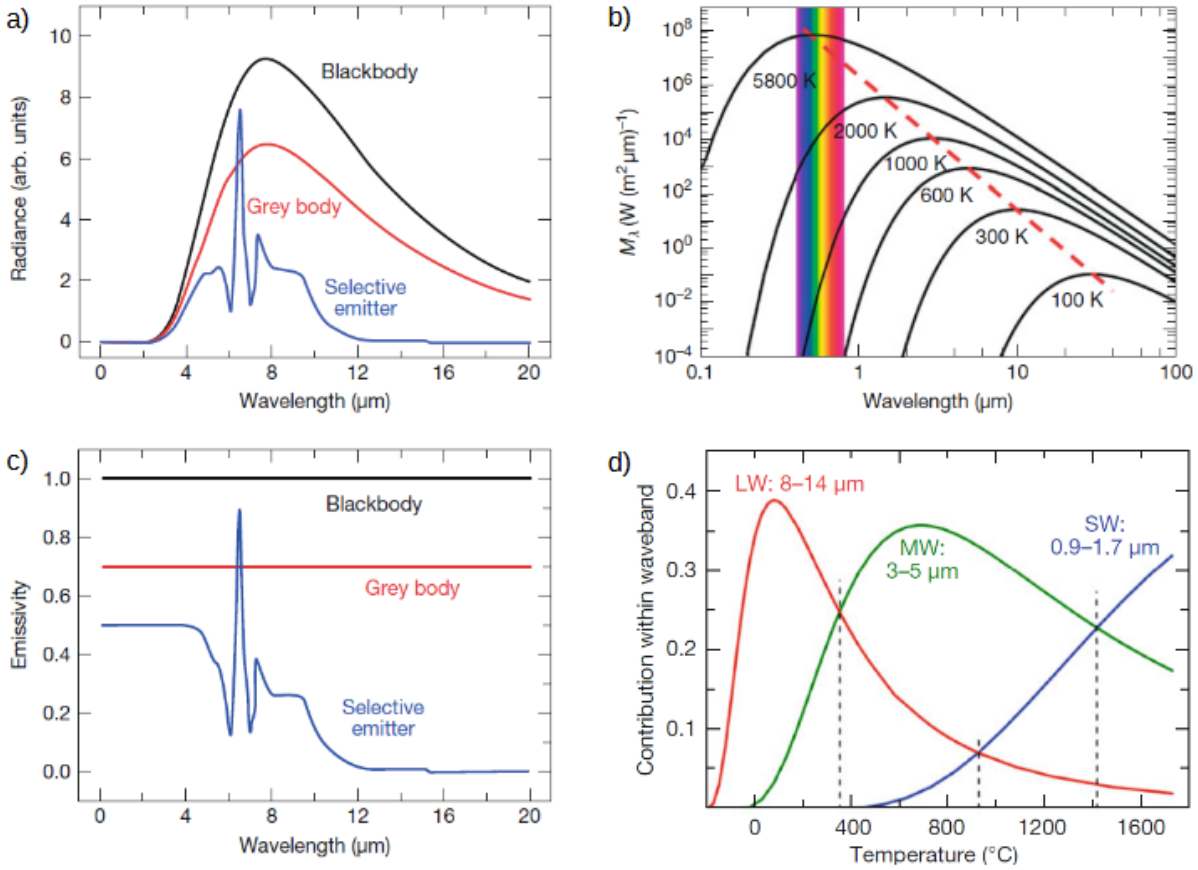

Figure 21: a) comparison of perfect blackbody, graybody and selective emitter emission spectra. b) blackbody spectra at different temperatures. The position of the peak shifts according to the Wien displacement law. c) comparison of emissivity of blackbody, graybody and selective emitter. In both blackbody and graybody, emissivity is independent of the wavelength. d) radiation contribution in three different wavebands, as a function of blackbody temperature. All figures are reproduced from [192].

Identifying the most intense region of the emission spectrum allows to select a sensor with optimal spectral sensitivity, thereby maximizing measurement accuracy for our application. From a previous study [138] it is known that temperatures during electrical forming in MCAF can rise up to hundreds degrees Celsius due to high current densities, up to $j = 10^{10}\ A/m^2$. After forming completion, resistivity increases significantly, but overall current density drops, and from the expression for Q we expect significantly lower temperatures, possibly close to room temperature. Our experimental evidence confirms this hypothesis (see chapter 3). According to Wien displacement law, the blackbody peak emission for temperatures between 300 K and 500 K is comprised roughly between $\lambda_{max} = 6\ \mu m$ and $\lambda_{max} = 10\ \mu m$, i.e., in the LWIR spectrum (see figure 21d). For this reason, I opted for a high-grade science camera microbolometric uncooled thermal camera working in LWIR ($7.5\ \mu m - 14\ \mu m$) spectral range. The thermal camera that I employed, Flir model A655sc, presents high sensitivity ($NETD = 30\ mK$ at room temperature) and high framerate ($200\ Hz$) [201]. MWIR

camera could be also used in my case of study, as in [189], [190] providing a comparable accuracy and even higher sampling frequency and spatial resolution (see [192], chapter 2). However, as will be apparent in chapter 3, neither higher NEPD, nor higher framerate are needed for my specific application, since environmental noise tends to dominate over camera sensitivity, and the achievable time resolution over RS events turns out to be strongly limited by substrate responsiveness (as already discussed in the previous paragraph).

As I already mentioned, the main limitation of the imaging technique with respect to the others is spatial resolution. The diffraction limit is

$$d = 1.22\lambda\frac{f}{a} \tag{2.8}$$

Where f is the focus distance and a the lens diameter. It turns out that resolution for LWIR cameras is practically limited to roughly $20\ \mu m$ in diffraction limited optics. Despite this limitation, high FOV of a thermal camera allows to effectively characterize collective dynamics in MCAFs taking place on the mesoscale or macroscale. The thermal camera has been equipped with a close-up lens that allows to obtain an Instantaneous Field of View (IFOV) of $25\ \mu m$. The camera FOV is 1.2 cm x 1.8 cm in full frame acquisition mode.

My main goal is to perform *quantitative* thermography, i.e., to obtain reliable temperature measurement from the measured radiance. Perfect blackbodies, defined as objects whose emission spectra strictly follow Planck's law and whose temperature can therefore be directly determined from it, do not exist in the real world. Nevertheless, it is possible to use the blackbody spectrum as a reference to describe the emission properties of many materials. Following the definition 1.26a in [192], I introduce the spectral emissivity

$$\epsilon(\lambda, \delta, \phi, T) = \frac{L(\lambda, \delta, \phi, T)}{L_{BB}(\lambda, T)} \tag{2.9}$$

where $L_{BB}(\lambda, T)$ is the radiance of a blackbody at temperature T and $L(\lambda, \delta, \phi, T)$ is the material radiance, and we also highlighted the dependence over direction of emission by means of the angles δ, ϕ (for the general case of the so-called non-Lambertian emitters, i.e., emitters that do not follow Lambert cosine law). From thermodynamics, the blackbody spectrum represents an upper limit to radiance at any given temperature. As a result, emissivity should always be $0 \leq \epsilon \leq 1$. A strong dependence of ϵ on the wavelength λ denotes a nongray emitter (typically gases or plastics). Emissivity is a key physical quantity that needs to be known in order to link radiance to temperature, i.e., to perform quantitative thermography. Thermal imaging systems collect light in an extended solid angle $\Delta\Omega$, and are sensitive to specific spectral ranges $\Delta\lambda$. For this reason, an

operative version of (2.9) should be introduced, by integrating radiance over solid angle and spectral range of the thermal camera [192], [202]:

$$\epsilon = \epsilon(\Delta\lambda, \Delta\Omega, T) \tag{2.10}$$

Due to (even small) deviations from graybody spectrum and uneven detector sensitivity over the spectral range, emissivity changes according to the imaging system, and should always be estimated. In most cases, and in particular if the relative changes of temperature are small (in the order of tens °C), the dependence of emissivity on temperature can be effectively neglected [203]. Now I can introduce some other important quantities in radiometry. Transmissivity (τ), reflectivity (ρ), and absorptivity (α) describe the fraction of incident light that is transmitted, reflected, and absorbed by a body, respectively. These quantities are related due to energy conservation:

$$\alpha + \rho + \tau = 1 \tag{2.11}$$

Transmissivity is typically extremely low in LWIR spectrum [192], i.e., thermal cameras are sensitive to temperature at the surface of objects. In the case of silica glass, LWIR skin depth can be estimated in the order of μm (see [204], and reference therein), whereas in Au it is approximately $\sim 10\ nm$. For this reason, we can neglect the contribution of transmission:

$$\alpha + \rho = 1 \tag{2.12}$$

If a body is in thermodynamic equilibrium with the environment, Kirchhoff law of thermal radiation holds [205], [206]:

$$\epsilon = \alpha \tag{2.13}$$

So, we can write:

$$\epsilon + \rho = 1 \tag{2.14}$$

This relation leads to consider an important drawback when performing thermography of metallic surfaces: metals are in most cases bad emitters, i.e., their emissivity is low (in the order of $\epsilon \sim 0.1$) [207], and only a small amount of thermal radiation is emitted. In these cases, IR radiation from the object is dominated by reflections from the surroundings, so temperature reading is prone to systematic errors, and quantitative

thermography measurements become extremely unreliable. As a general rule, quantitative thermographic measurements (with accuracy at least in the order on 5 °C) can be done if $\epsilon > 0.5$ [208].

However, some key physical characteristics of the systems under study enable us to overcome the limitation of dealing with an extremely poorly emissive metal, and, in turn, to perform reliable thermal characterizations. First of all, our system presents a coverage that is less than 100%, and the radiating surface consists of both Au nanoparticles and uncovered glass regions [138]. Glass and gold (polished) present strongly different emission properties, with $\epsilon_{glass} \sim 0.8$ and $\epsilon_{Au\ bulk} \sim 0.02$ respectively [207], and glass turns out to be a particularly good emitter in LIR spectrum. Camera IFOV is four orders of magnitude higher than typical cluster size, the overall emission is effectively a weighted average of MCAF and glass contributions, as modelled in [138]. MCAF emissivity is particularly challenging to estimate, but nonetheless, it is considerably higher than that of bulk, polished surfaces. The emissivity of bulk metals with polished surface can be estimated through the Hagen-Rubens relation [209], that follows by taking the asymptotic behaviour of the electric permittivity at low frequencies estimated by the Drude model [210] and computing the reflectivity by using Fresnel equations. According to the Hagen-Ruben relation, the emissivity of a metal is expected to increase with increasing resistivity. For this reason, the high density of defects and roughness of the surface could play a significant role in increasing the emissivity of MCAFs. However, this simple approach cannot be used for quantitative estimations of MCAF emissivity due to the presence of absorption mechanisms that are not included this model and that provide a further enhancement in emissivity. The first limitation in the applicability is the failing of the bulk hypothesis (as reported also in [211]): the Hagen–Rubens relation neglects multiple scattering phenomena arising from the two interfaces of a thin film. Metallic films with thickness beyond roughly 100 nm, always present very low emissivity (typically $\epsilon < 0.1$) [207], due to high absorption of thermal radiation in the bulk, in good accordance with the theoretical prevision. However, when thickness approaches skin depth (roughly 10 nm for Au), multiple scattering phenomena at the interfaces strongly enhance the emissivity [212], with the theoretical limit for Au has been estimated to be $\epsilon = 0.5$ [212], [213]. Importantly, metallic nanoparticles smaller than the wavelength of light can induce localized surface plasmon resonances (LSPRs) [214] potentially leading to a further enhancement of light absorption in the material. Furthermore, rough surfaces can strongly enhance emissivity in metals [215]. Even if relatively high roughness (in the order of 100 nm) has a strong impact over emissivity in LWIR spectrum, this factor can still contribute to enhance emissivity in our systems. For all these reasons we expected to find a substantially higher emissivity for MCAFs both respects to bulk counterparts and atom assembled thin films.

The effective emissivity in our systems has been measured by means of the most simple direct method widely reported in literature [216], [217], [218], [219]. Namely, all the absorbed energy should be emitted in the form of thermal radiation. Glass substrate is almost completely opaque in LWIR spectrum, so neglecting the contributions of transmitted light, we only need to deal with reflections [188], (see equation 2.14). Given the small working distance of the close-up lens (4.5 cm), the main contribution of reflected light comes from

camera sensor itself, that is heated above room temperature by the electronics. The contribution of the reflected radiation has been characterized by means of a highly reflective surface and set in the camera software to take it into account in radiance-temperature conversion. Subsequently, temperature has been measured by means of a reference object of known emissivity (electric tape) in good thermal contact with the PCB. Then, MCAF was imaged, and the value of emissivity that reproduces the same temperature as the reference measurement is considered the emissivity of MCAF. [220]

2.4 Analysis methods

In this section I present two analysis methods that I employed for the characterization of the thermal videos. As I already discussed in Section 2.3, and will be apparent in Chapter 3, my study relies on the possibility to obtain spatial information regarding RS activity. The first technique that I discuss is a feature extraction algorithm that allowed me to identify the regions of the samples that are responsible for RS. In the last paragraph I present a measure of correlation, useful to characterize interactions between different regions of the samples.

2.4.1 Principal Component Analysis

Principal Component Analysis (PCA) is an unsupervised learning algorithm for dimensionality reduction that allows to retrieve the most informative variables (or set of variables) in a dataset [221], [222], [223], [224]. Before explaining the main concepts behind PCA, I need to clarify the meaning of the term "informative variables". Consider a generic dataset, consisting of data points in an n-dimensional feature space, i.e., each observation is represented as a tuple of values $x = (x_1, x_2, \dots, x_n)$. These data points are distributed according to a specific multivariate distribution, that is fully characterized by all its statistical moments, namely, mean, variance, skewness, kurtosis, etc. Lower-order moments of a distribution are generally the more informative, since they capture features related to the global structure of the dataset, such as centre of mass and dispersion. Higher-order moments, on the other hand, tend to describe finer details that may be less relevant and more sensitive to noise. If the features of interest are described specifically by relative variations between data points (as in the case of temperature variations induced by RS), mean is no more relevant, and the variance becomes the most informative moment. In a multivariate dataset, the variance is described by the covariance matrix:

$$cov_{ij}(\boldsymbol{x}) = E\left[(x_i - \mu_i)(x_j - \mu_j)\right] \tag{2.15}$$

Which account for the covariance between different variables. $Tr\left(cov_{ij}(\boldsymbol{x})\right) = \sum_{k=1}^{n} \sigma_k^2$, represents a measure of the overall variance in the dataset. The matrix $cov_{ij}(\boldsymbol{x})$, is obviously symmetric by construction, so it has

a complete set of orthogonal eigenvectors, with real eigenvalues associated. It can be diagonalized by means of a suitable change of basis $\boldsymbol{x} \rightarrow \boldsymbol{x^{PC}}$, that being a unitary transformation, preserves the total variance $Tr\left(cov_{ij}(\boldsymbol{x})\right) = Tr\left(cov_{ij}(\boldsymbol{x^{PC}})\right)$. Diagonalization in the context of PCA is usually done by mean of Singular Value Decomposition algorithm (see [225] for details). In the new basis, covariance between different variables is null, and the overall dispersion in the dataset is taken into account by the eigenvectors alone. The eigenvectors of the covariance matrix are referred as Principal Components (PCs). Each eigenvalue $\sigma^2_{PC_k}$quantifies the amount of variance explained by the corresponding component, PC_k. Each PC accounts for a fraction of the overall dispersion $Tr\left(cov_{ij}(\boldsymbol{x_{PC}})\right)$, and PC are ordered such as their relative $\sigma^2_{PC_k}$ are in descending order. This way, the first PCs are the one associated with the largest fraction of explained variance in the dataset, i.e., they are the most informative. Dimensionality reduction is generally performed in the context of PCA, since PC decomposition typically allows to summarize the most significant information in the subspace generated by the first PCs alone.

In this case of study, each recorded frame represents an experimental point, described by a number of variables equal to the number of pixels (e.g., 40x80=3200 in case of 1 mm x 2 mm samples), and the collection of all frames in a single recording constitutes the dataset. If some consistent and systematic temperature variations in correspondence of one or few pixels are present in a recording, they are likely to produce a spread of data along specific directions in the experimental domain, which can be detected by PCA. Obviously, the number of temperature variations, along with temperature magnitude influences the variance in the dataset. For this reason, the regions of the samples undergoing the most intense or frequent events will appear in the first PCs.

Some caution is needed when interpreting the results of the analysis if the data exhibit strong irregularities. PCA is not a clustering technique and rely only the first two moments of the distribution. For this reason, if the dataset contains some features that cannot be effectively captured by these two moments alone, PCA is likely to be unable to resolve them, as shown in figure 22 (see also figure 4 in [224]).

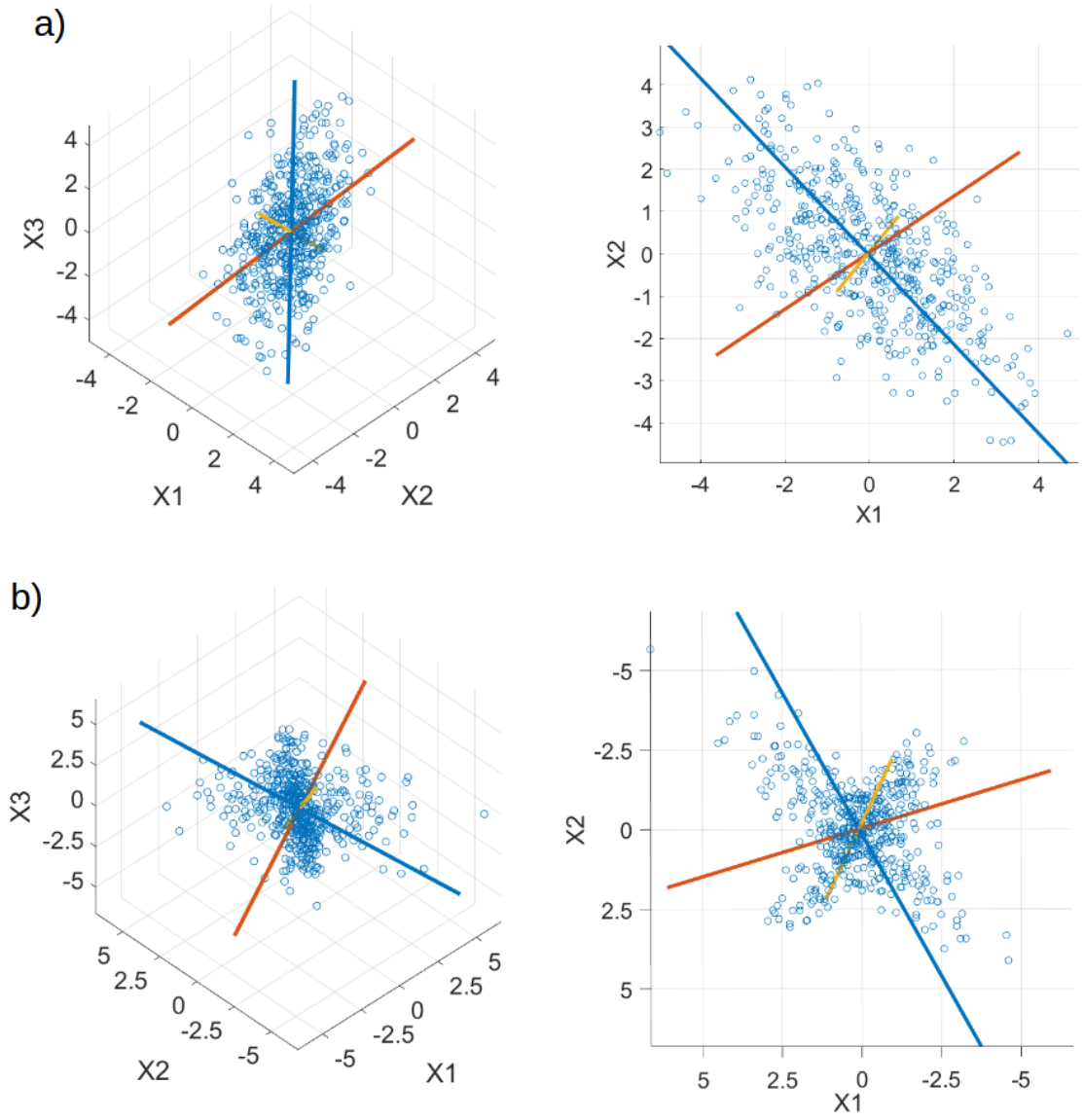

Figure 22: results of PCA applied on 3D randomly generated datasets with two different distributions. A) moments of order higher than two are null. PCs (coloured lines) correctly accounts for the significant features in the dataset. B) moments of order higher than two are non-zero. PCs cannot discriminate data dispersion along two distinct directions, as they tend to mix them.

2.4.2 Spike Time Tiling Coefficient

To investigate correlations in MCAFs, the first step is to find a suitable metric, i.e., a parameter able to quantify their intensity. A useful source of inspiration comes from neuroscience: different metrics for neuron correlations exist in literature (see for example [226], [227], [228]), and one of the most popular is the

correlation index [229]. However, it has been shown by C. S. Cutts and S. J. Eglen that most of them lack some key requirements to provide a robust measure of correlation [230]. In first instance, some are not robust against the amount of data, i.e., their results depend on the length of the recordings. Second, and most importantly, most of these metrics show a dependence on neurons firing rate or on the differences in firing rates between neurons.

The Spike Time Tiling Coefficient (STTC) [230] provides a robust metric to measure correlations that overcome all the aforementioned limitations, and has been adopted for the quantification of the correlations between switching sites. From its introduction, STTC has been widely used to study biological neuronal cultures, [231], [232], [233]. In the remaining part of this this paragraph, I will introduce STTC and discuss its main properties.

Consider a recording with duration T, and two regions A and B producing N_A and N_B RS events respectively during this time interval. Each event in A occurs at a certain instant, $0 \leq t_i^A \leq T$ with $i = 1, \dots, N_A$. Given a synchronicity window Δt, it is possible to define:

$$\tilde{T}_A = \left\{ \bigcup_{i=1}^{N_A} \left[t_i^A - \Delta t, t_i^A + \Delta t \right] \right\} \cap [0, T] \tag{2.16}$$

$\tilde{T}_A$ corresponds to the set of all time instants "in proximity" to any RS event happening in A during the recording. The meaning of "proximity" is intrinsically related to the choice of the synchronicity window, that sets the time scale at which correlations can rise. The knowledge about the timescale of the mechanisms that produce correlations allows to set a reasonable value for Δt (or, at least, to set an upper bound to Δt). Note that $\tilde{T}_A$ is defined by considering also intervals starting *before* RS events in A. This in not conflicting with causality principle but instead accounts for the possibility that events in B trigger events in A.

I will use $\tilde{T}_A$ to define two other quantities, namely:

$$T_A = \frac{\lambda(\tilde{T}_A)}{T} \tag{2.17}$$

where $\lambda(\tilde{T}_A)$ represents the Lebesgue measure of $\tilde{T}_A$. Roughly speaking, T_A is the fraction of the recording where the activity in A takes place. If the recording period is sufficiently long, i.e., the statistics is sufficiently high, T_A turns to be the probability of any random event to happen synchronously to any RS event in A (according to the frequentist interpretation of the probability).

Turning the attention to the switching site B, I define:

$$P_A(B) = \frac{\left|\{t_i^B : t_i^B \in \tilde{T}_A, i = 1, \dots, N_B\}\right|}{N_B} \tag{2.18}$$

where the notation || denotes set cardinality. $P_A(B)$ is the fraction of RS events in B that happen simultaneously to any TE in A, according to the synchronicity window Δt (i.e., takes place within $\pm\Delta t$ from at least one RS event in A).

STTC discriminates correlations by comparison with the expected statistics in uncorrelated activities: considering a sufficiently long recording period, if the activity in A is completely uncorrelated to the activity in B, then it should be $P_A(B) = T_A$. On the contrary, if activities in A and B tend to be positively correlated, we expect that $P_A(B) > T_A$. Similarly, in case of anticorrelation $P_A(B) < T_A$.

By using the quantities that have been defined above, STTC has the form:

$$STTC = \frac{1}{2}\left(\frac{P_B(A) - T_B}{1 - P_B(A)T_B}\right) + \frac{1}{2}\left(\frac{P_A(B) - T_A}{1 - P_A(B)T_A}\right) \tag{2.19}$$

STTC is defined to fulfil symmetry with respect to A and B, and the normalization ensures that it is bounded between STTC = -1 (fully negatively correlated) and STTC = 1 (fully positively correlated). It must be noted that Δt is the only free parameter of the model: if the characteristic timescales of the physical mechanisms underlying the interactions are unknown, Δt cannot be fixed a priori. However, it can be varied in order to probe the existence of characteristic correlation timescales. [230]. Due to the lack of precise information about the physics that could generate interactions in MCAFs, I followed the second strategy.

3 Results and Discussion

This chapter presents the main outcomes of my research activity and is organized as follow: **Section 3.1** illustrates the potential of IR microthermography for characterizing the morphology and electrical behaviour of MCAF. On these bases, the development and validation of the data analysis tools used in the subsequent sections are presented. **Section 3.2** presents the results of electrical and thermal characterization of RS in two terminal devices during constant bias stimulations, with emphasis on the temporal and spatial statistical properties of these phenomena. The impact of the geometry over the electrical characteristics of MCAF and it implications for the design of MCAF-based devices is also discussed. Starting from the insights from the previous part of the discussion, **Section 3.3** presents the response of MCAF to time varying stimuli and discuss the possibility of describing it by means of a semi-deterministic model. Finally, **Section 3.4** introduces the design of multiterminal devices and discuss the possibility to improve the random search protocol for receptron programming.

3.1 IR-Microthermography for morphology and electric conduction characterization during forming

As I already highlighted in the previous chapter (section 2.2), the forming process induces structural modifications in MCAFs, from the nano to the macro-scale [138], that are responsible for the emergence of the complex phenomena, subject of this work. In this section I will describe the stimulation protocol that I employed for forming, and I discuss the possibility to investigate structural modifications by means of IR imaging.

3.1.1 Forming process

Forming has been carried out by applying a sequence of constant bias stimulations, with duration of one minute each. The applied voltage has been increased after each stimulation in order to keep the increment in the electric field constant to $2 * 10^3$ V/m. This procedure is carried on since high resistance state ($R > 10^6\ \Omega$) has been reached. At this stage, MCAFs are able to reversibly switch from high resistance to low resistance states, and multilevel RS can be triggered.

During each forming step, temperature is not uniform across the sample. Even if thickness and electrical conduction properties are spatially homogeneous, the central region of the deposit reaches the highest temperatures (figure 23b).

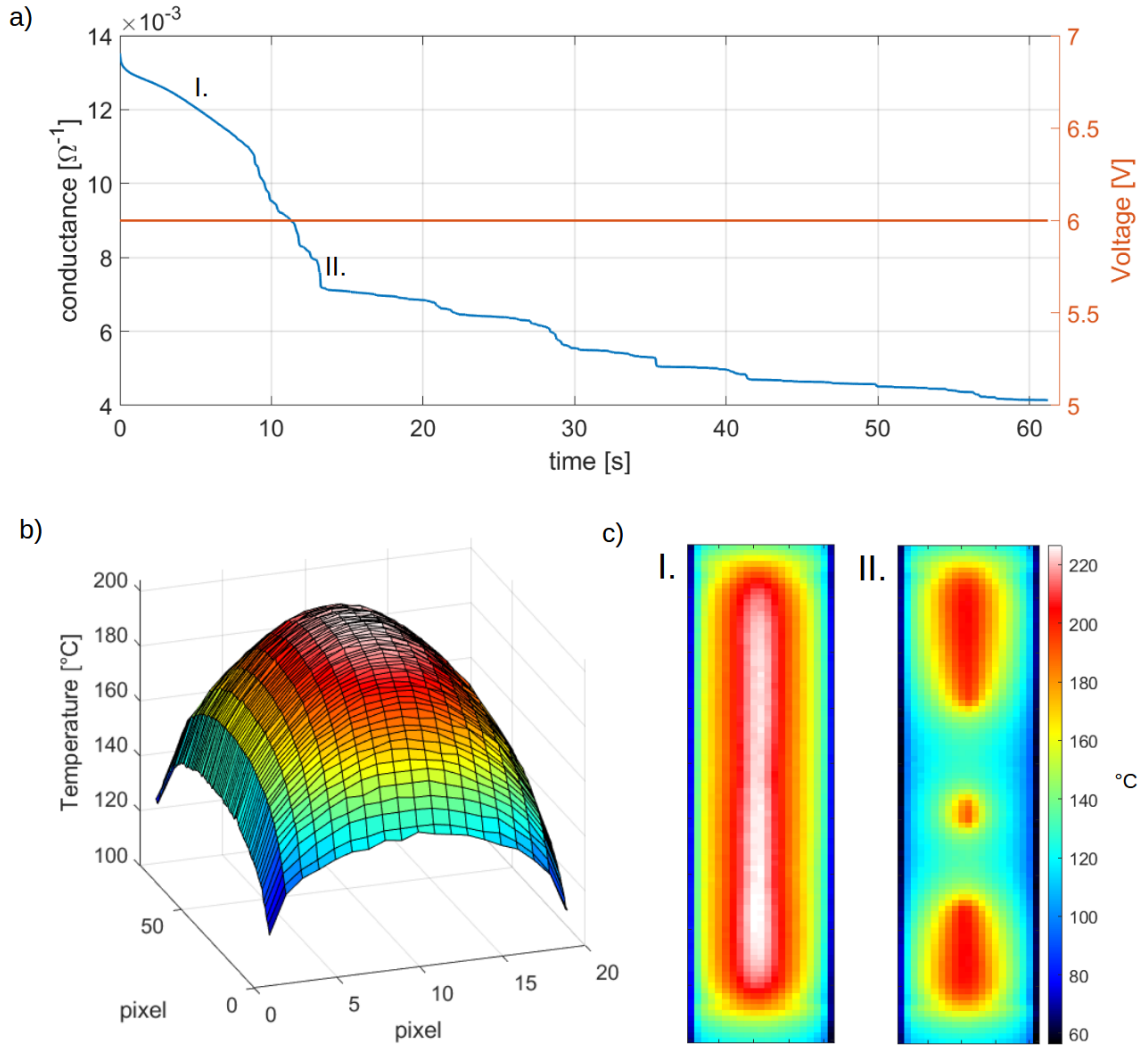

Figure 23: a) temporal evolution of the conductance during a forming step at constant bias (6 V). Step-like drops are visible. b) temperature map during the first stages of the forming process. The applied bias is 4 V. At this stage emissivity is no more uniform, and, therefore, temperatures on the border could be slightly underestimated. C) temperature in two different instants of the forming step in (a). In II., temperature has decreases in different regions because of a sequence of conductance drops.

Intuitively, a region in the centre of the deposit accumulates the heat diffusing from all directions, while a region near the edge of the deposit can more effectively dissipate heat on the surroundings (refer also to the analytical models for heat dissipation in similar geometries discussed in [234], [235], [236]). Metallic electrodes have high thermal conductivity and good dissipation properties due to their large surface. So, they also play a significant role in heat dissipation [237]. Temperatures in the range between 200 °C and 300 °C have been reached during forming.

During the first few forming steps electrical conductance always undergoes a small but sensible increase in the order of 1% of the initial conductance. During the later stages of forming, it progressively decreases till reaching values in the order of $10^{-6}\ \Omega^{-1}$. The decrease in electrical conductance shows a smooth trend interspersed by step like drops (figure 23a). These drops are typically accompanied by sharp decrements in temperature occurring along the central section of the deposit (figure 23c). The first drop of the temperature always takes place in the centre of the deposit. At the end of the forming process, i.e., when the low conductance state is reached, no more regions above room temperature are visible. Optical inspection reveals that a groove is often present along the central region of the deposit, i.e., where the highest temperatures are reached during forming.

Emissivity measurements were performed between subsequent stimulations in the central region of the deposit. These measurements highlight that, during forming, MCAF emissivity in the LWIR spectrum changes dramatically (see figure 24a), following an opposite trend with respect to conductance: during the first stages of the forming process, emissivity undergoes a slight decrement. Then, after several stimulation with increasing applied voltages, the emissivity increases, reaching typically values between 0.65 and 0.70 at forming completion.

Having glass and gold strongly different emission properties, the emissivity of MCAF/glass samples strongly depends on film coverage. In [138] the emissivity of MCAF/glass has not been directly measured but estimated by averaging gold and glass emissivity weighted by coverage and exposed surface respectively. The measured emissivity is in very good agreement with the estimation provided by this simple model [138], assuming nanostructured gold emissivity to be 0.5 [138], [212] and coverage equal to 0.7 for MCAF of thickness 15 nm, in accordance with previous SEM and AFM characterization [138].

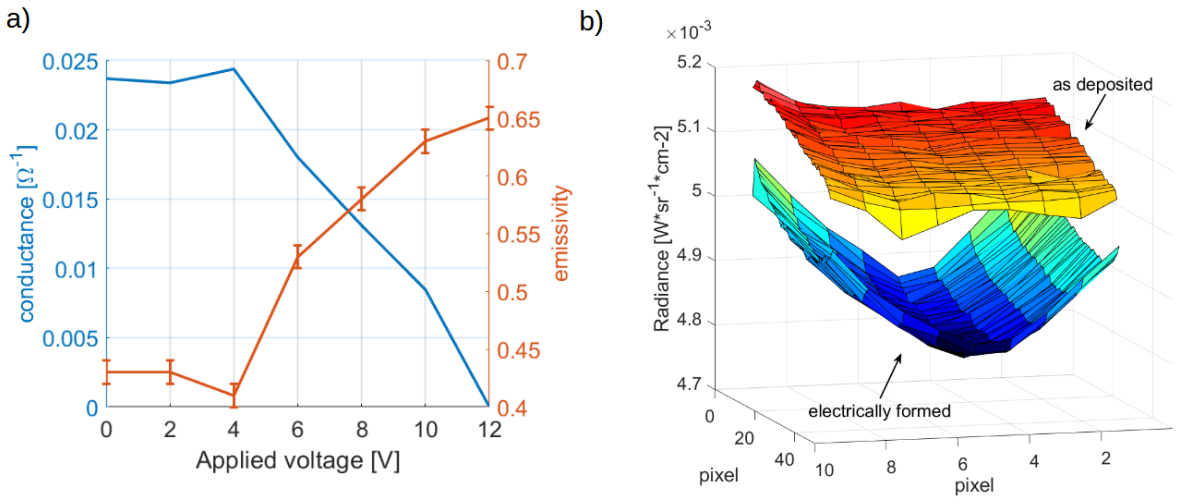

Figure 24: evolution of emissivity and morphology during forming process. a) evolution emissivity and conductance during forming. b) comparison of radiance maps of as deposited and electrically formed sample.

Radiance decreases significantly at the centre of the deposit, due to the decrease in reflectivity and increase in emittance. Adapted from [127].

The emissivity variation is not uniform across the sample. In figure 24b I report the radiance maps of a sample before and after forming for comparison. As deposited sample presents almost uniform radiance, while a significant drop in the central region is visible after forming. This effect is due to the decrease in reflectivity concurrent with the increase in emissivity (see section 2.3, equation 2.14). It is worth noting that the region of higher emissivity in Figure 24b coincides with the area that reached the highest temperatures during forming (Figure 23b), highlighting that the structural changes responsible for the emissivity variation are thermally driven.

Importantly, it should be noticed that the emissivity at the end of the forming process is sufficiently high to allow reliable quantitative thermographic measurements (see discussion in section 2.3).

3.1.2 Annealing and dewetting

The concurrent variations in conductance and emissivity can be explained by morphological modifications induced by annealing. Electrical and thermal annealing has been widely studied in nanostructured metallic systems such as nanowire networks [238], [239], and cluster assembled films [240]. Significant thermally induced morphological modifications have been reported in ranges of temperatures compatible with those recorded during MCAF forming. During heating, these systems display an evolution in electrical conductance that is also analogous to that observed in MCAFs, namely, an initial increase followed by decrease.

When nanostructured materials are heated for short periods of time and at low temperature, annealing is responsible for the reduction of the density of defects and voids [241]. Furthermore, surface diffusion takes place, thus leading to in plane growth and cluster coalescence [240]. These two effects cause an increase in the electrical conductance due to reduced density of electron scattering sites and the increasing number of conductive paths across the network. Direct imaging of the formation of conductive paths due to thermal annealing has been already reported by Sannicolo et al. [190] in nanowire networks.

These two effects can also explain the decrease in emissivity observed in the early stages of MCAF electrical forming. In fact, the increase in the number of conductive paths and the reduction of the density of defects leads to the reduction of electrons confinement, thus producing a decrease in absorptivity and increase of material reflectivity. On the other hand, in plane growth of the nanostructure increases coverage, thus enhancing the fraction of poorly emissive surface.

In case of higher temperatures or longer heating periods, dewetting (also referred as “solid-state dewetting”) takes place. This phenomenon consists in the transition of thin films from a continuous layer to a set of isolated particles at temperatures significantly below bulk melting point [171]. This effect is due to surface free energy minimization [242], and consequently, the range of temperatures in which this phenomenon takes place

strongly depends on film thickness, with thinner films undergoing dewetting at lower temperatures [243], [244].

Structural reorganization due to dewetting has been observed in electrically formed MCAF in previous studies [138], [166]. However, here, for the first time, I report reliable information about the temperature reached during forming. Dewetting has been reported in atom assembled Au films with thickness 15 nm deposited on glass substrate after few minutes of thermal annealing at 550 °C [245]. Although this temperature is lower than bulk melting point of gold (1064 °C [246]), it is still significantly higher than the maximum temperatures recorded during MCAF forming. This observation highlights the crucial role of MCAF morphology in governing thermally induced structural modifications as well as the final morphology at forming completion: as already discussed in Chapter 2, MCAF present a significant fraction of clusters with diameter below 2.5 nm, whose melting point is well below 550°, due to size effect [247]. In addition, the high density of defects and voids in MCAF strongly promotes dewetting phenomena, since these features act as nucleation point for voids, thus driving islands separation [242]. Temperatures compatible with the ones observed during MCAF forming have been reported to cause dewetting in nanostructured gold assemblies also on different substrates [248].

Dewetting induces depercolation [240], thus explaining the decrease in the electric conductance in MCAF during the last stages of electrical forming. Furthermore, the reduction of Au coverage leads to the observed increase in emissivity due to increased fraction of exposed glass surface.

Atomic Force Microscopy (AFM) measurements were performed to monitor the evolution of the morphology during forming and confirmed these findings. In figure 1a are reported three AFM images taken at different stages of the forming process. From the comparison of figure 25a I. (as deposited) and II. (after electrical stimulation) it is possible to appreciate the variation in cluster size and the increment in the exposed glass surface. The root-mean square roughness (Rq) of the film increases from about 3 to 6 nm due to the vertical growth of the islands.

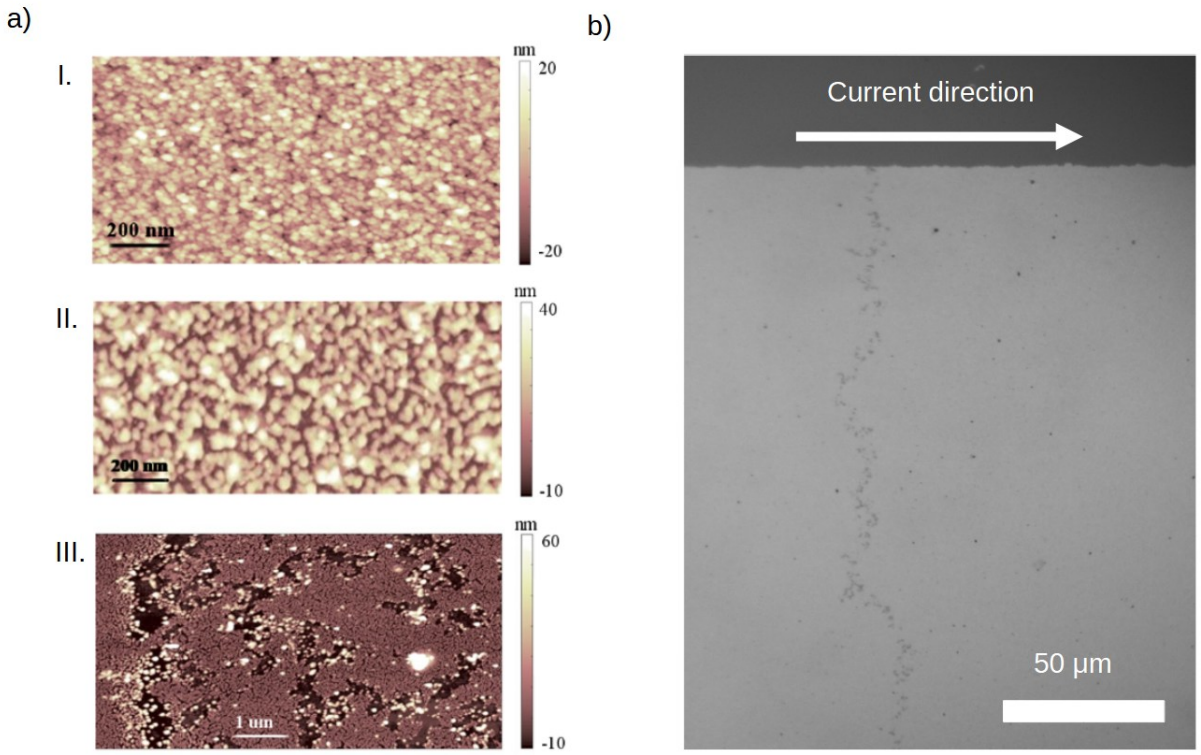

Figure 25: a) MCAF morphology in three stages of forming. I. As deposited, II., sample undergoing dewetting, III. Sample with extensive crack induced by electromigration. b) optical image of the groove. Adapted from [127].

In summary, in this section I presented the thermal characterization of the forming process, highlighting the possibility to monitor the evolution of the morphology by means of IR microthermography. Several thermally activated mechanisms responsible for these modifications were discussed with particular focus on dewetting. I showed that dewetting in MCAF happens at significantly lower temperatures with respect to atom assembled counterparts, due to the reduced cluster size and the influence of the high density of defects.

3.1.3 Electromigration and Joule heating interplay

In the previous paragraphs I discussed the influence of purely thermal effects on the evolution of MCAF morphology. However, another crucial role in determining structural and electrical properties in MCAFs during forming is played by electromigration [249], [250]. This phenomenon is particularly important in thin films and even more in nanostructured films for different reasons. In first place, nanostructured films present an extremely high density of defects that promotes electron scattering and momentum transfer to the atoms.

Secondly, surface atoms are much more numerous in nanostructured films with respect to bulk materials, and their binding energy is strongly reduced.

Electromigration actually results from the interplay of multiple phenomena, that I am briefly reviewing in the following. First, the electric field causes the motion of conduction electrons, that undergo scattering events with ionized atoms, thus causing a momentum transfer opposite to the current direction. This mechanism is referred as "wind force". Nonetheless, positive ionized atoms are subject to force induced by electric field in the direction of the electric current ("direct force"). These two contributions can be expressed in terms of the electric field $\vec{E}$ and the effective valence of electrons Z_{wind} and ions Z_{direct} respectively.

$$\begin{aligned} \vec{F}_{wind} &= Z_{wind} e\vec{E} \\ \vec{F}_{direct} &= Z_{direct} e\vec{E} \end{aligned} \tag{3.1}$$

Specifically, Z_{wind} is a fictitious valence that accounts for the magnitude and the direction of the momentum transfer by electron scattering, while Z_{direct} depends on actual valence of the chemical species, with a correction due to electron screening (electron density is higher in vicinity of ions) [251].

The summation of the two contributions constitutes the *field driving force of electromigration:*

$$\vec{F}_{em} = \vec{F}_{wind} + \vec{F}_{direct} = (Z_{wind} + Z_{direct}) e\vec{E} = (Z_{wind} + Z_{direct}) e\rho\vec{j} = Z^* e\rho\vec{j} \tag{3.2}$$

Where the electric field $\vec{E}$ has been expressed in terms of current density $\vec{j}$ by means of Ohm law, assuming the resistivity ρ to be isotropic. The effective valence $Z^* = Z_{wind} + Z_{direct}$ has been introduced for convenience. The high resistivity of MCAFs compared to the bulk counterpart that is due to the high density of defects is responsible for the enhancement of the field driving force. Furthermore, joule heating inherently causes temperature gradients. In turns, atoms momenta present gradients, that induce diffusion opposite in direction with respect to the temperature gradient (Soret effect). As in the previous case, a driving force $\vec{F}_{tm}$ can be associated to ions motions under a thermal gradient [252]:

$$\vec{F}_{tm} = -\frac{Q^*}{T}\vec{\nabla}T \tag{3.3}$$

Where Q^* is the heat of transport, i.e., the heat flow needed to maintain the steady state condition per unit mass transport [252].

The motion of chemical species due to thermal gradients is commonly referred as *thermomigration* [253], and in most cases it produces a higher mass transport than electromigration in strict sense [162].

Two other mechanisms of mass transport are present: atoms accumulated at the edge of a conductor due to filed driving force or thermomigration are subjected to a tensile stress that counteracts the wind force. This effect produces the *stress gradient driving force*.

$$\vec{F}_{\sigma} = \Omega\vec{\nabla}\sigma \tag{3.4}$$

Where Ω is the atomic volume and σ is the stress tensor.

Finally, the different densities of vacancies and atoms induce spatial variation of their respective chemical potentials. Chemical potential gradients induce the motion of both species. The mass flux $\vec{J}_{diff}$ is proportional to the gradient of their concentration:

$$\vec{J}_{diff} = -D\vec{\nabla}c \tag{3.5}$$

Where c is the concentration and D is the diffusion constant.

The last two mechanisms have typically much less impact with respect to field driving force and thermomigration. The net atom flux can be obtained by summing up the contributions to atom motion for all the different driving forces, and adding the diffusion term:

$$\vec{J}_{total} = -D\vec{\nabla}c + \mu c\left(\vec{F}_{em} + \vec{F}_{tm} + \vec{F}_{\sigma}\right) = D\left(-\vec{\nabla}c + \frac{c}{k_B T}\left(\vec{F}_{em} + \vec{F}_{tm} + \vec{F}_{\sigma}\right)\right) \tag{3.6}$$

Where μ is the atom mobility, linked to the diffusivity by the well-known Nernst-Einstein relation $D = \mu k_B T$ [254].

In the case of MCAF forming, the presence of the groove cannot be explained by thermomigration since the temperature gradient is relatively small at the centre of the deposit. Conversely, it must be purely field induced. However, the formation of the groove in the middle of the deposit, suggests that temperature still play a significant role in localizing the most important structural modifications. This can be linked to different effects. Most importantly, the probability of atomic displacement depends on the energy distribution (Boltzmann at thermal equilibrium), with higher temperatures corresponding to higher displacement probabilities. Moreover, the diffusivity typically follows an exponential trend with temperature [255], leading to a significantly higher atomic flux at high temperatures, as predicted by (3.6).

The stress gradient driving force, that usually counteracts the effects of mass transport, can be significantly less important in case of cluster assembled films with respect to atom assembled counterparts, since, due to the presence a large fraction of loosely bonded surface atoms and hillocks connecting neighbouring nanoparticles, strains cannot be accumulated, and atoms are likely to migrate instead.

The Black law [256] describes the mean time to failure due to electromigration:

$$\langle t \rangle = AJ^{-2}e^{\frac{\Phi}{kT}} \tag{3.7}$$

Where $A = A(T)$ and Φ is the activation energy for failure. According to Black law, the mean time to failure decreases by increasing the temperature. In fact, high temperature increases atoms mobility, thus enhancing electromigration. This effect explains why the first region that undergoes strong modifications, thus significantly increasing electrical resistance (i.e., the first region where the temperature drops), is the central one (figure 23c). Step like changes in the conductance in figure 23a are likely to be relatable to electromigration effects, while continuous changes are due to much slower dewetting phenomena.

Contextual AFM measurements show the presence of extended cracks and uncovered regions (figure 25a III.). in correspondence of the groove (figure 25b).

The characterization of electrically and thermally induced structural modification has been already shown to be crucial in understanding the electrical properties of nanogaps [257] and nanowires [258].

In summary, during the forming process, significant structural modifications take place due to joule heating and electromigration interplay, both at the nano and meso-scale [138]. Specifically, during the early stages of forming, temperature promotes the reduction of defects, while in the later stages it drives dewetting, and, consequently, depercolation. Both phenomena have already been reported in nanostructured systems within temperature ranges comparable to those observed in MCAFs. They are responsible for the reorganization of the nanostructure in a vast portion of the samples and can be easily tracked by means of IR imaging. Electromigration is exacerbated in the region that reaches the highest temperature during forming, i.e., the centre of the deposit. Here, a groove is formed.

3.1.4 Metallic cluster assembled film conduction after forming

In this section I discuss the application of IR microtermography for the characterization of the electric conduction after forming.

After forming, MCAFs can reversibly switch between a high resistance state and a low resistance state, as previously reported in literature (see paragraph 2.3). High resistance state is characterized by conductance below $10^{-6}\Omega^{-1}$ and by a strongly non-linear current-voltage characteristics (figure 26a), indicating the dominance of non ohmic conduction mechanisms, in agreement with the data reported also in [124].

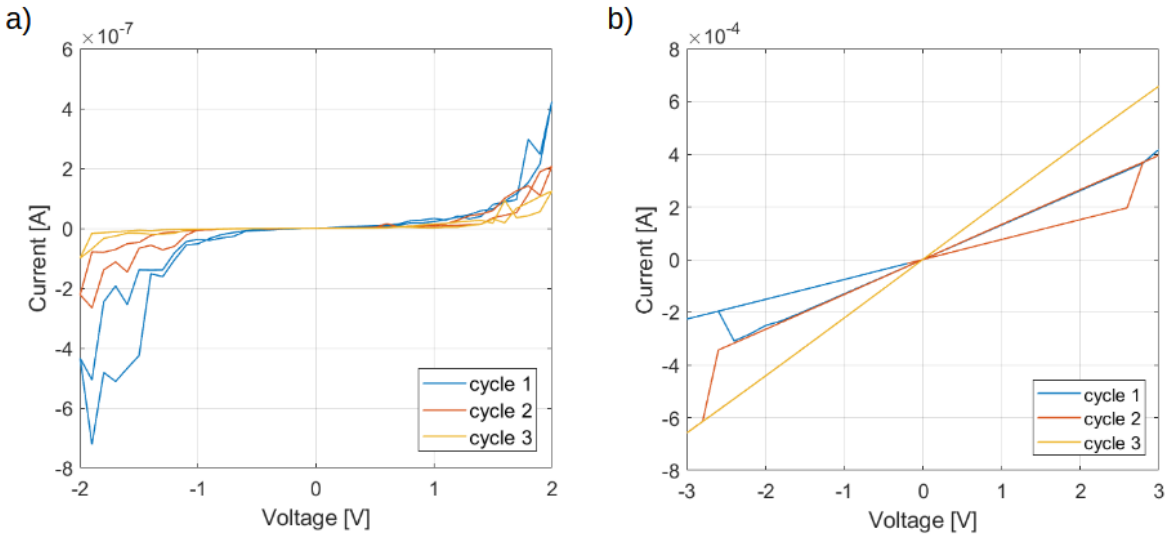

Figure 26: cyclic voltammetry performed on the same sample in high resistance state (a) and low resistance state (b). In (b) the IV curve is formed by multiple linear branches, corresponding to distinguished conductance levels. Ohmic conduction is present as long as the sample is stable in a conductive state and no RS events take place.

The existence of a well-defined high resistance state with non ohmic conduction has been previously reported also in Au/ZrO_x nanocomposite cluster assembled film and MCAFs [259], [260], [261], with same ranges of currents that I recorded.

In low resistance state, MCAFs current-voltage characteristics present multiple linear branches, indicating the existence of different ohmic conduction states. The conductance typically ranges between $10^{-3}\Omega^{-1}$ and $10^{-4}\Omega^{-1}$. In figure 26b, three separated linear branches are easily identifiable. RS events happening during the voltage ramps cause the transition from one branch to another.

For samples in low resistance state, no features are easily detectable for applied bias minor of roughly 0.5 V. However, by increasing the applied bias, some temperature inhomogeneities become detectable in the form of hotspots, roughly found on the sample axis perpendicular to current direction, and in correspondence of the groove (section 3.1.1). These observations suggest that RS in MCAF in low resistance states is mainly due to the formation and rupture of conductive paths electrically in parallel.

Interestingly, during prolonged stimulations with constant bias, hotspots can reversibly change temperature, and new hotspots can appear in new locations of the MCAF, thus indicating the modification of the conduction map due to RS events (see figure 27a). A thermal recording is freely accessible in the supporting information of ref. [127]. The temperature reached in the hotspots depends on the applied voltage. In this case of study, peak temperatures were in the order of tens °C above room temperature for stimulation at 3 V (highest bias

applied). However, hotspots often present a sharp peak of temperature in correspondence of a single pixel. In these cases, the size of the heating region is smaller than camera IFOV ($25\ \mu m$), and the measured temperature is systematically underestimated with respect to the actual local temperature.

Lock-in thermography [192] has been employed to investigate whether additional features could be detected in the conduction map beyond the clearly identifiable switching sites. However, all the relevant features are already visible in single frames of the thermal videos, albeit with a noisier background. This finding corroborates the hypothesis that hotspots emerge in regions where the current density is much higher than in the surrounding areas, as a result of the formation of conductive bottlenecks.

When MCAF explore high resistance states, no switching sites are detectable by means of standard IR thermal imaging, neither by lock-in thermography. This is due to the extremely low currents, and probable absence of continuous conductive paths across the sample, since quantum conductance is roughly two order of magnitude higher than MCAF conductance in this cases ($G_0 \sim 10^{-4}\Omega^{-1}$[262]). As discussed in section 2.3, MCAF are heated up due to joule heating, and the heat produced depends quadratically on the current density and only linearly on the resistivity. For this reason, under the same applied bias, more heat is produced in systems in low resistive states with respect to high resistance states. This also explains why the conduction map is particularly sensitive to the regions of the film with higher current densities.

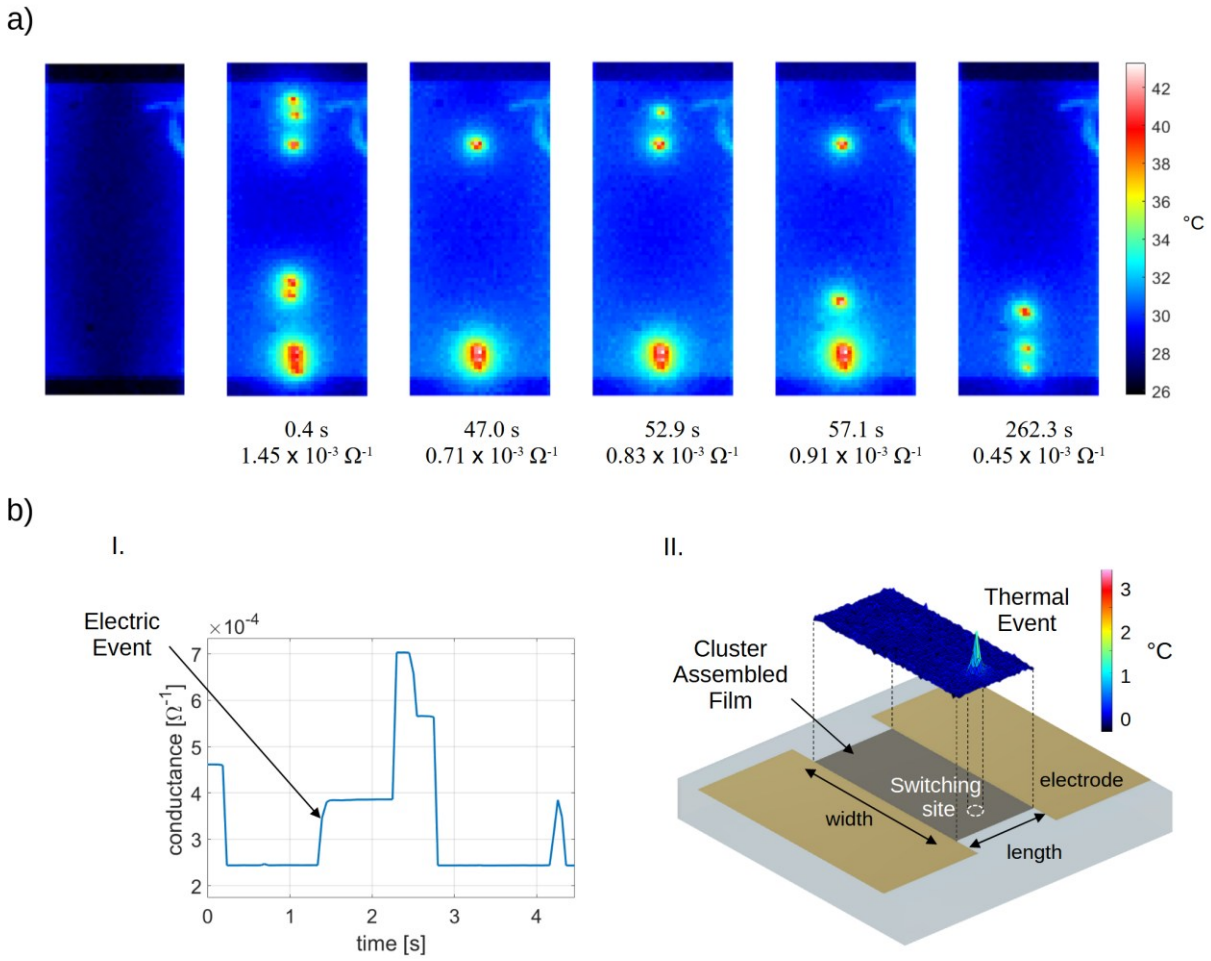

Figure 27: a) six frames recorded during a constant bias stimulation after forming. b) visual summary of the vocabulary. I. electric events refer to conductance variations due to RS. II. Thermal events refers to temperature variations due to RS. Adapted from [127].

Electrical characterization has been performed in the context of thermal characterization. For this reason, I distinguish between events that have been detected by means of thermal characterization, referred as Thermal events (TEs), and by means of electrical characterization, referred as Electric Events (EEs). All the locations of the sample undergoing TEs are defined as *switching sites* (see figure 27b for a visual summary of the vocabulary). The reader should be aware that the notion of switching site is strongly related to the spatial resolution of the thermal camera, since it is not possible to distinguish features below 25 μm (IFOV).

Films deposited with different geometries have been fabricated in this study (see paragraph 3.3.2), and for easiness in the descriptions I will adopt the following vocabulary (also reported in figure 27b): the spacing between electrodes is referred as sample *length*, while the dimension of the sample in direction perpendicular to current is referred as sample *width*.

In [108] I showed that during constant voltage stimulations MCAFs present spontaneous RS bursting activity, presenting strong statistical similarity with biological counterparts. In this context, I performed electric stimulation of electrically formed MCAFs at constant voltage bias, similarly to my previous work and other studies on analogue systems [104], [119], in order to monitor the evolution of the conductance map over time, and characterize the interactions between regions that are likely to produce the bursting dynamics reported in [108].

In the next two paragraphs I will present the analysis tools that I developed and validated with the aim to perform this study.

3.1.5 Principal Component Analysis for feature extraction in thermal video: evidence of Switching Sites

During few minutes of constant voltage stimulations, MCAFs easily produce tens or hundreds RS events. One of the most important pieces of information that I need to retrieve from thermal videos is the number, location and the size of the regions responsible for these events.

However, this information in not immediately accessible from thermal recordings. For this reason, I developed a feature extraction technique to retrieve it efficiently. Principal Component Analysis (PCA) has been employed for this purpose. In section 2.4.1 I presented a short review of the key concepts underlying this technique. Here I will show that PCA is a valuable tool for identifying important features about spatial occurrence of RS activity from thermal recordings.

The results of the application of PCA on a thermal video are presented in figure 28. Specifically, the first eight PCs are reported in figure 28a. The plot of the cumulative explained variance is shown in figure 28b. Notably, a vast portion of the of the variance in the dataset (over 90%) is explained by the first three PCs alone, indicating that PC decomposition provides an effective representation of the information contained in the video. Roundish features corresponding to the switching sites undergoing RS events during the stimulation are easily detectable in the first five PCs, while noise dominates the others. Some switching sites are present in more than one PC both due to synchronous RS activity in different switching sites and complex features in the distribution of the data points.

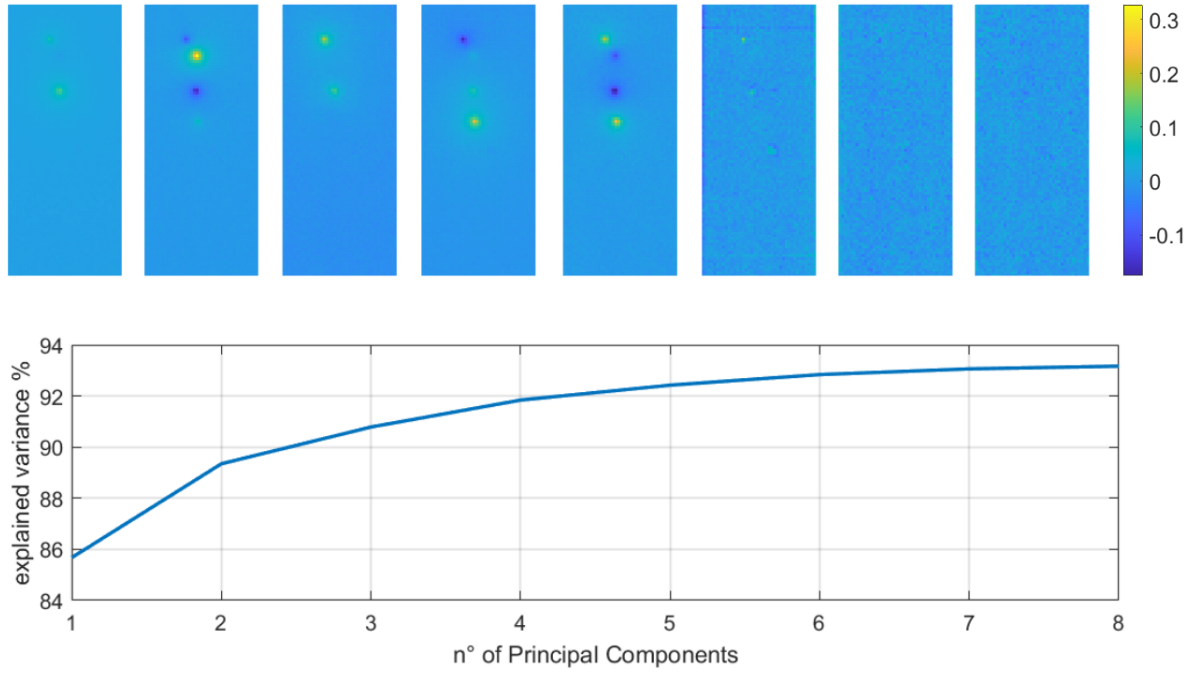

Figure 28: results of PCA performed on a thermal video (15000 frames) acquired during constant voltage stimulation at 2 V. a) first eight PCs. The modulus is dimensionless and normalized to unity. B) Percentage of cumulative explained variance for each PC. Notice that the first three PCs account for over 90% of the variance in the dataset.

In the following, I will use PCA especially for easiness in the comparison of RS spatial features in different thermal videos. PCA is widely used in neuroscience to characterize evoked spiking activity in biological neural networks [263], [264].

3.1.6 Resistive switching event detection

After the identification of the switching sites, I developed an algorithm for the automatic detection of TEs, in analogy with the algorithm implemented in [108] for EEs detection: absolute temperature variations recorded in differential frames [192] has been monitored and TEs have been detected by means of thresholding procedure.

Thermal images present a noise that is both introduced by the camera itself, that is quantified by the NETD (see section 2.3), and by thermal fluctuations and disturbances from the environment. Noise standard deviation computed on single pixels has been measured: $\sigma_{noise} \sim 150\, mK$. In Figure 29a I report the temperature recorded in a pixel corresponding to an active site during a constant bias stimulation. TEs are easily identifiable and are associate to thermal transients, often lasting for more than one sampling period. This effect is due to glass responsiveness to temperature variations (quantified by specific heat) and poses a limit over maximum achievable temporal resolution. Since thermal transients often last for more than one sampling period, the

differential time frames were computed using frames 40 ms apart. The thermal transients associated to TEs are also linked to another important effect, namely heat diffusion. In particular, if conduction is restored in a switching site, heat starts to be produced in a small region corresponding to the switching site itself but then diffuses through both MCAF and the substrate. Consequently, temperature rises not only in the switching site, but also in the surrounding regions until a steady state is reached everywhere. The speed of heat diffusion is limited by the thermal properties of the material (in this case, both specific heat and thermal conductivity, see section 2.1), causing regions farther from the switching site to experience temperature increase with significant time delay (see figure 29 I.). Analogous phenomenology takes place in the opposite scenario, i.e., when a conductive path is broken (see figure 29 II.). From my experimental evidence, the thermal transient in these system takes roughly hundreds of milliseconds to reach completion in regions distant tens or hundreds of micrometres from the switching site. This fact should be carefully considered when setting a threshold for TEs detection: a low threshold, set by including only noise standard deviation, leads to spurious event detection, due to long lasting thermal transients in the vicinity of the switching sites.

On the other hand, heat diffusion gives also the possibility to distinguish more effectively actual TEs from random noise: in fact, due to heat diffusion, TEs are always associated with coherent temperature variations on several adjacent pixels in the thermal image. For this reason, I performed denoising of the differential frames before thresholding by means of 2D wavelet decomposition and reconstruction with low-pass filter [265]: the elimination of high frequency components of the wavelet spectrum allows to improve the quality of the image, without affecting the most significant features, that are effectively captured by low frequency components.

In the following sections, I consider the location of a TE as the pixel where the maximum absolute temperature variation takes place.

A schematic summary of the detection algorithm is presented in figure 30a.

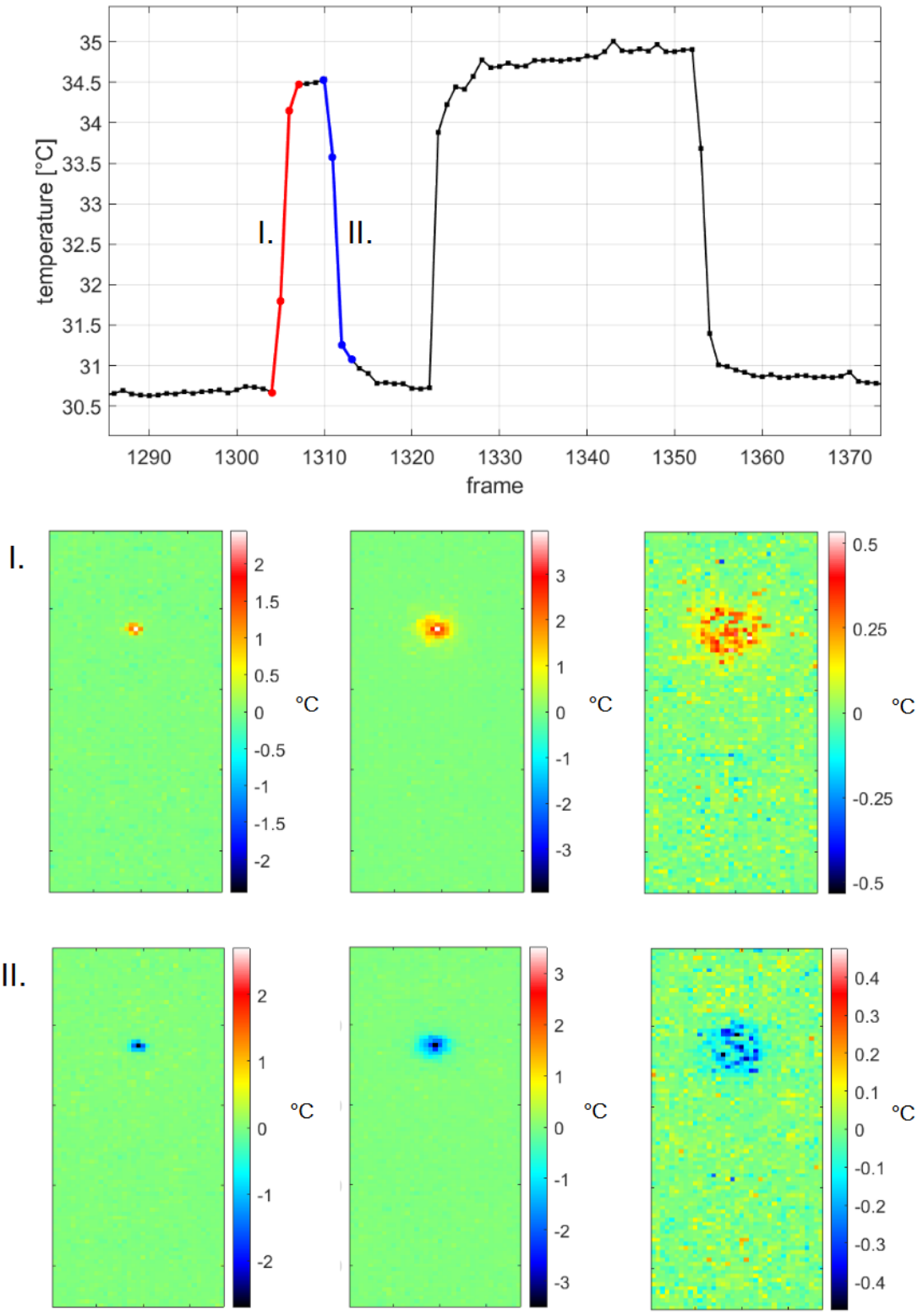

Figure 29 a) evolution of the temperature on a single pixel corresponding to a switching site during a constant voltage stimulation with baias 3 V. The sampling frequency is 50 Hz. The switching site produces a series of TEs. The differential thermal frames associated with heating and cooling are displayed in b) I. and II. respectively. Notice the different colorbars.

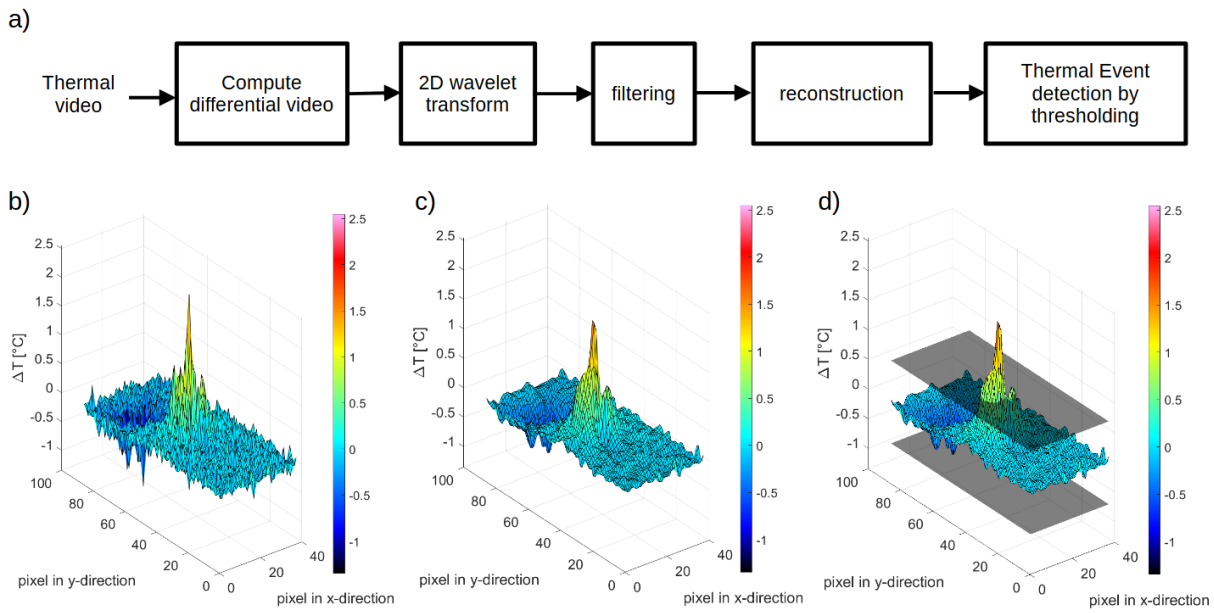

Figure 30: a) block diagram of the TEs detection algorithm. b-d) three stages of the image processing performed by the detection algorithm: (b) differential image of frames 40 ms apart (c) same image in (a) after denoising performed by wavelet decomposition and filtered reconstruction, (d) thresholding process for TE recognition. Surface representation has been adopted to highlight the effects of denoising. Adapted from [127]

In figure 31 the number of TEs detected per each pixel is superimposed with the first three PCs for comparison: as expected, TEs detected by the algorithm that I developed are clustered in correspondence of the switching sites identified by PCA, thus proving the effectiveness and complementarity of these two analyses.

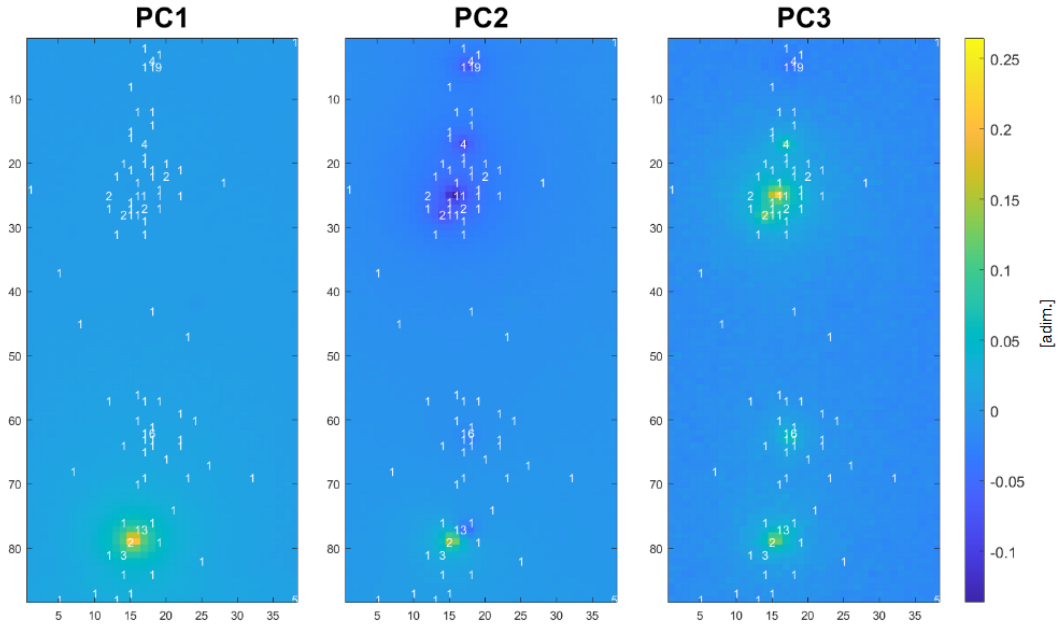

Figure 31: validation of TEs detection algorithm by means of comparison with PCA. The three first PCs obtained from the recording of a stimulation with bias 3 V are reported. The number of the detected Thermal Events (TEs) per pixel are indicated in white. Despite the presence of some spurious events (essentially due to heat diffusion after real TEs), it is easy to notice the clustering of TEs in correspondance of the switching sites found by PCA. Adapted from [127]

Furthermore, it is possible to notice that TEs are not equally distributed over the switching sites, with the number of events per site varying from few units to tens. These findings highlight that the number of TEs significantly exceeds the number of switching sites, thus indicating that conductive paths are recurrently broken and formed in the same locations.

The detection algorithm has been further validated by comparing the time series of TEs and EEs detected during several stimulations with constant bias. The time series of temperature and conductance variations associated to TEs and EEs in a representative case have been reported in figure 32a-b. As immediately apparent, there is a one-to-one correspondence between the two time series, thus proving that the detected TEs corresponds to actual RS phenomena.

In figure 32c I report the histogram of the conductance variations associated with EEs (I), and the temperature variations associated with TEs (II) for a representative stimulation. Both distributions are centred on zero and present symmetric features that are mostly due to the frequent exploration of different conductive states levels. Most of the conductance variations due to the exploration of different resistive levels produced multimodal and symmetric features in the resistance histogram, that are present also in the temperature histogram,

highlighting preferred ways for the network to structurally and electrically reorganize. This is a consequence of heating and cooling of the same ASs in multilevel RS.

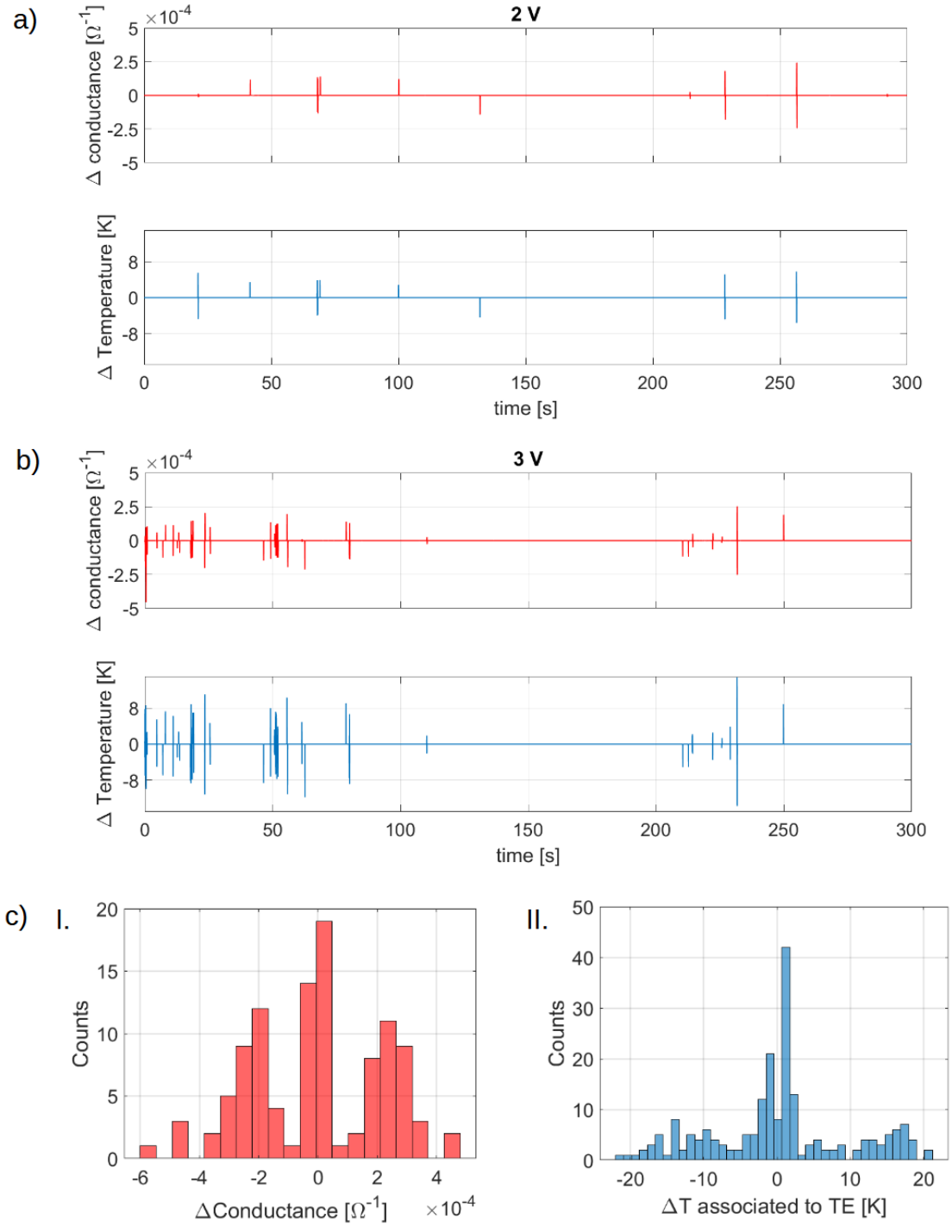

Figure 32: Conductance variations associated EEs (red), and temperature variations associated with TEs (blue) detected by the algorithm that I developed, for two applied biases, namely 2 V (a) and 3 V (b). c)

histogram of the conductance (I) and temperature (II) variations associated to electric events and thermal events during a stimulation with bias 3 V. Adapted from [127].

3.2 Resistive Switching temporal and spatial characterization by means of electric and microthermographic measurements

In this section I present the results of electrical and thermal characterization of RS activity with constant bias stimulations, with main focus on role of the applied bias, impact of the geometry of the deposit, over the number of switching sites and correlation between them. In the last paragraph of this section I also discuss the electrical responses to time varying stimuli. The described phenomenology will be particularly useful during the discussion of device optimization in section 3.3.

3.2.1 Role of the voltage bias

Results

The most suited voltage range for stimulation has been determined empirically from experimental observations. First of all, I noticed that RS is a threshold activated phenomenon, and the threshold was found to be in the range between 1 V and 2 V: at 1 V RS activity is almost completely absent, and no change in the conduction map are detectable in the thermal videos. On the other hand, for voltages above 4 V, the current density is sufficiently high to easily destroy any conductive path that is formed, leading to the exploration of high resistance states, where conduction cannot be easily tracked by IR-microthermography (as previously discussed in section 3.1.4).

I performed constant voltage measurements on samples with geometry (length = 1 mm, width = 2 mm), at three different voltage bias, namely 1 V, 2 V and 3 V. In this range of voltages RS is easily triggered but the samples do not explore high resistance states. Stimulations at 3 V usually present the highest number of RS events.

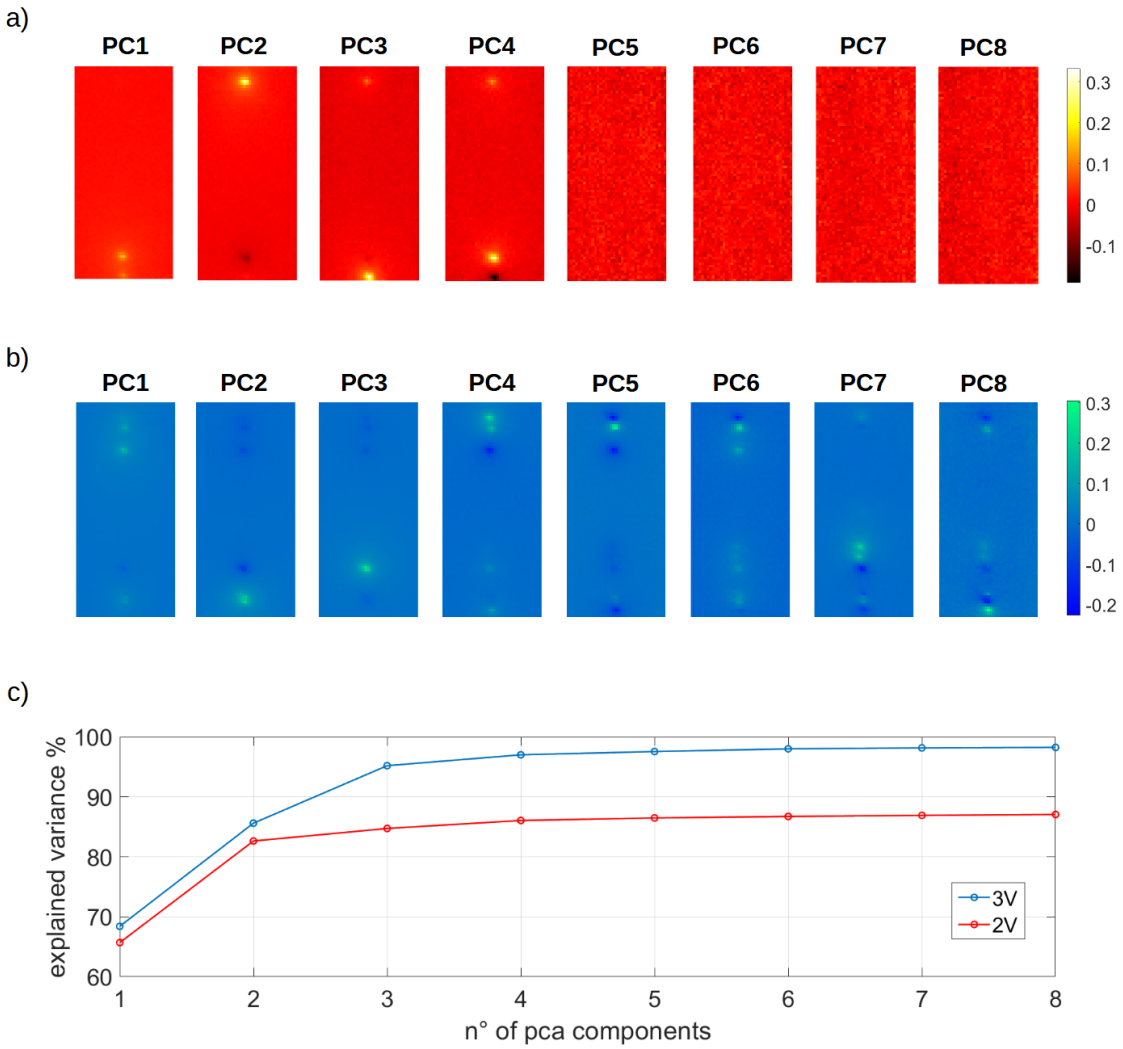

Figure 33: first eight principal components for two thermal videos, aquired with bias equal to 2 V (a) and 3 V (b). c) cumulative explained variance for each PC. From [127]

The first finding is that the number of switching sites participating in RS activity depends on the bias. In figure 33 I show the results of the application of PCA on thermal videos acquired from the same sample during stimulations with different bias, namely 2 V and 3 V. In both cases most of the variance in the dataset is explained by the first few PCs (figure 33c). However, comparison of the PCs for the two stimulations (figure 33a-b), clearly shows that a larger number of switching sites is triggered with higher voltage bias. The plot of the cumulative explained variance in figure 32c also support this evidence: in the case of 2 V stimulation, the explained variance reaches the elbow point much faster due to an inferior number of informative PCs.

Discussion

These findings highlight that different switching sites present different activation thresholds and will turn to be particularly important in the discussion of switching sites coordination (section 3.2.5). RS in MCAFs has been already reported to be a threshold activated phenomenon (see section 2.3), but it is noteworthy that the activation threshold changes according to the substrate. In [108] I already reported an analogous phenomenology on MCAF/SiOx systems with similar geometry, and the activation threshold was found to be above 5 V.

Metallic nanoparticle networks near the percolation threshold have been already reported to display threshold activated RS and multilevel RS strongly influenced by the applied bias [119].

3.2.2 Role of the cluster assembled film dimensions

In MCAF, the geometry of the deposit has a strong impact over the topology of the network, as already pointed out in simulative studies on analogous systems [266]. Furthermore, heat dissipation properties significantly change according to geometrical parameters [234], [235], [236], [237], thus promoting or suppressing thermal effects over electromigration during forming. For these reasons, it is of paramount importance to monitor the evolution of the RS activity with dimensionality. IR microthermography offers a unique possibility to characterize the fundamental mechanisms leading to complex RS dynamics and explore RS activity in samples at different length scales, starting from millimetric devices already well characterized also in previous studies [108], [138], [267], to micrometric ones.

I employed microlithography (chapter 2.2) to fabricate samples with different geometries. Since the direction of the electric current breaks the symmetry of the MCAF deposit, it is reasonable to expect significant differences in samples with different shapes. For this reason, sample *width* and *length* were independently reduced to micrometric scale (refer to figure 27 for the vocabulary), while keeping the remaining dimension on millimetre range. The minimum dimension has been fixed to $125\ \mu m$, for both width and length, i.e., above camera MFOV, in order to allow easy detection of switching sites.

As already discussed in chapter 2.2, the usage of cellulose lithographic mask allows to keep the minimum feature size (and so, the resolution of the edges) well below the minimal MCAF dimension for these specific geometries.

Results

Constant voltage stimulations have been performed as discussed in section 3.2.1, for both classes of samples. The shrinkage (miniaturization) of the sample along the direction perpendicular to current flow (i.e., length = $1\ mm$, width = $125\ \mu m$), leads to the reduction of the number of switching sites. In this class of samples, only one or two are clearly identifiable, as highlighted by PCA in figure 34a-c. On the contrary, samples with small length (i.e., length = $125\ \mu m$, width = $1\ mm$), still display a number of switching sites comparable to macroscopic samples presented in the previous paragraph (figure 34b-c). This difference is highlighted also in

the plot of the cumulative explained variance, in figure 34c: the elbow point is reached after three PCs in case of width = 125 μm, while a higher number of informative PCs are present in the case of length = 125 μm, as a conseque of higher number of switching sites.

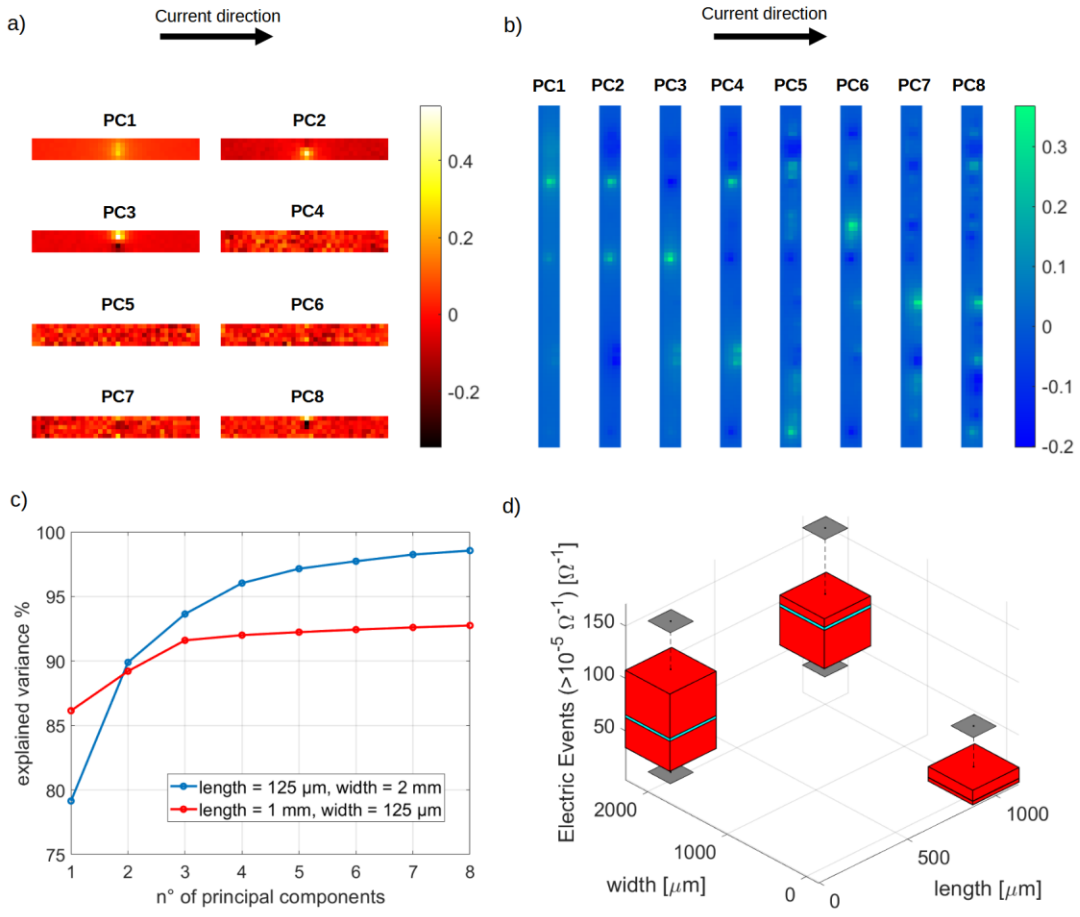

Figure 34: visual comparison of switching sites and RS activity in samples with different geometries. (a) PCs of a thermal recording of a sample of with geometry (length = 1 mm, width = 125 µm), during constant voltage stimulation (applied bias 3 V). Two switching sites are visible in the first three PCs. (b)) PCs of a thermal recording of a sample of with geometry (length = 125 µm, width = 2 mm), during constant voltage stimulation (applied bias 3 V). (c) Explained variance comparison. For the sample with geometry (length = 2 mm, width = 125 µm) the explained variance present a clear elbow point in correspondance to the third PC. On the contrary, for the sample with geometry (length = 2 mm, width = 125 µm) the explained variance continues to increase significantly for higher number of PCs, as a conseque of higher number of switching sites and TEs. (d) Comparison between EEs detected in samples with different geometries. Data refer to electrical stimulations at ±3 V. The red boxes represent the first and third quartiles, and the grey planes indicates minimum and maximum values. From [127].

Concurrently with the reduction in the number of active sites for width = 125 μm, I registered a reduction in RS activity with respect to the other classes of samples. In figure 33d I report the number of EEs with amplitude higher than $10^{-5}\ \Omega^{-1}$, that are easily detectable with thermal imaging, for all three classes of samples. The reduction in the number of EEs is consistent with the reduction of the width, and of course, of the number of switching sites.

Discussion

These results confirm the initial observation that multiple switching sites tend to form in parallel rather than in series, if enough space is provided perpendicularly to the direction of the current. This finding is particularly important, since highlights a significant difference between MCAF and other classes of nanostructured materials, such as nanowire networks, where electrical stimuli often lead to winner takes all (WTA) dynamics [170], [189], i.e., the formation of few, localized current pathways across the network. Interestingly, my findings are also in sharp contrast with the results in the simulative study by Heywood et al. ref. [266] for nanoparticle networks near the percolation threshold. While the decrease in the number of switching sites with reducing sample width is consistent with their findings, the simulations also predict that the number of switching regions should increase with sample length, since multiple switching regions rise in series along the same current paths. Keeping the same voltage bias, an immediate consequence is the reduction of RS events with increasing sample length, since the average voltage across each gap decreases, till falling below the threshold necessary to trigger RS. This characteristic has not been recorded in MCAFs, since there is no strong dependence between sample length and threshold voltage or number of RS events (figure 34d). Furthermore, according to [266], WTA should be expected with increasing sample length, since, assuming tunnelling as the dominant conduction mechanisms in the nanogaps, most of these will remain open in absence of sufficient bias, thus favouring the existence of few conductive paths. Once again, this is not the case of MCAF, since the number of current paths does not show a significant dependence on sample length.

The key difference between MCAF and other systems where nanogaps present a volatile behaviour, will be apparent also in the discussion about response controllability.

The fact that samples with different length produce RS activity almost in the same voltage range lead also to the observation that most of the voltage drop must take place across the groove, that, as expected, turns out to be the most resistive region of the film. However, the regions in the vicinity of the groove, that undergo strong structural modifications as well, as clearly indicated by IR imaging and AFM measurements (as discussed in section 3.1), can be responsible of minor RS events and introduce significant series resistance between electrodes and the switching sites.

3.2.3 Measuring Switching Sites coordination by means of the Spike Time Tiling Coefficient

Energy efficiency in biological neural networks has been widely recognized to be grounded in the collective dynamics driven by the complex connectivity that is established in these systems. Correlated spiking activity in particular, play a crucial role both in information processing and in self-organization of neuronal systems during development [268], [269]. For this reason, a wide literature in neuroscience focuses on studying the statistics of interactions between neurons along with information propagation across the networks. In neuroscience, temporal correlation of spatially separated neurophysiological events is referred to as functional connectivity [270], [271].

Typically, studies are performed in-vitro, by means of neuronal culture grown on micro-electrode arrays (MEA) or high-definition MEA (HD-MEA) that allow synchronous recording of the spiking activity of small clusters of neurons or even single neurons [272], [273], [274].

Interestingly, both in-vitro and in-vivo studies have shown that different degrees of functional connectivity can coexist in the same neuronal population: some clusters of neurons exhibit stronger correlations respect to others, reflecting a balance between integration and segregation, as suggested by G. Tononi [275], [276]. This complex behaviour is facilitated in presence of a functional topology of the system comprising different degrees of connectivity, an idea that has been formalized with the concept of *small world* networks [277]. This topology has been readily found in biological neural networks [278], [279], [280].

Furthermore, many neuronal populations in the brain have been found to operate near a critical regime [281]. In fact, other than being organized in a scale-free network, consistent with small-world topology, neurons present a spontaneous (non-evoked) spiking activity displaying statistical properties such as scale invariant avalanches of spiking activity that are a typical hallmarks of criticality [282]. The term Self Organized Criticality (SOC) is often used to refer to such dynamics in biological neural networks (but not only), to highlight the ability of these systems to self-tune in critical states. This dynamic state has been widely recognized to ensure optimal processing capabilities and signal propagation across the network ([283], see also [105] and references therein).

Recently, criticality has been demonstrated in nanostructured devices [105], [173], [180], [182], [284]. However, these results often rely on simulated systems, due to lack of possibility to access spatial information on RS activity in physical devices.

IR-microthermography allows to resolve RS event in space, thus giving the unique opportunity to perform this kind of studies on MCAFs. My focus in this study is to provide a first characterization of the functional connectivity in these systems by studying the correlations between different switching sites. Correlation studies are one of the basic tools also in the analysis of neural communications and signal processing [285], [286]. Criticality hypothesis cannot be verified in this study essentially due to short duration of the recordings. In

fact, tens or hundreds events typically taking place in my recording do not provide sufficient statistics to verify the presence of power law scaling in avalanche size and duration and fit the critical exponents [104], [287]. Future studies will address more specifically the question of criticality.

To investigate correlations in MCAFs, the Spike Time Tiling Coefficient (STTC) has been adopted. As already discussed in section 2.4.2, other metrics that are commonly used in neuroscience are not robust against the number of data, differences in firing rates and relative differences in firing rates between neurons. This could be detrimental for my analysis, since intrinsic sample to sample variability in the number of RS events is present and, in addition, switching sites in the same sample often present substantially different excitabilities and switching rates (see section 3.2.1). STTC provides a robust metric to measure correlations that overcome all the aforementioned limitations.

I will discuss the presence or absence of significant interactions between switching sites by computing the STTC for different intervals of Δt. STTC has been computed varying Δt from 0.02 s (i.e., thermal camera sampling period) to 20 s (sufficiently small with respect to the sampling period, i.e., 300 s). The comparison across pairs of switching sites naturally provides a quantitative measure of the correlations within the system.

3.2.4 Coordination over time and space

Results

In order to study the correlations between different regions of the samples, I identified the coordinates of the switching sites by means of PCA and I have performed TEs detection (section 3.2.2) storing temporal and spatial coordinates for each detected TE. Then, I have built binarized time series representing the RS activity for each switching site by assigning TEs to switching sites according to spatial proximity. Specifically, only TEs whose peak is recorded in correspondence of a switching site or within its nearest-neighbour pixels have been attributed to that specific switching site (see figure 35). The data obtained with this procedure can be seen as somehow analogous to multi-electrode array (MEA) recordings in neural cultures [273], [274].

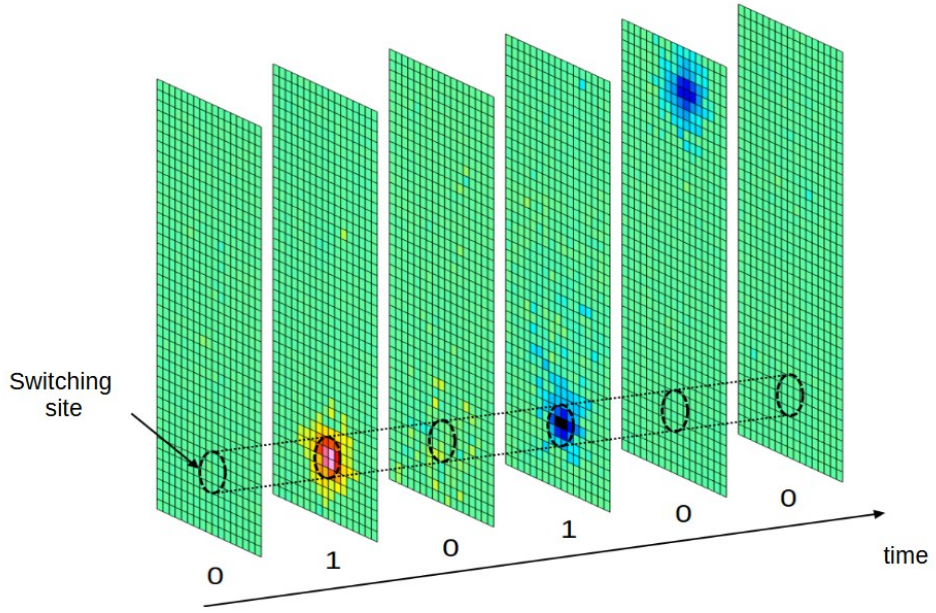

Figure 35: construction of the binarized time series of TEs in a single switching site. Differential frames where TEs have been detected in correspondence to the switching site are labelled with Boolean 1. From [127].

Before characterizing correlations between RS activity in different regions of MCAFs, I studied the temporal statistics of TEs in single switching sites, in order to draw a comparison with the statistics of the overall activity measured by the electric characterization alone [108]. Analogous studies have been carried out in biological neural networks [274].

I found that single switching sites display bursts of RS activity, similarly to what I have reported to the collective behaviour of the network [108]. Starting from this evidence, I exploited the unsupervised method presented in [288] for the identification of bursts and mean Inter Switch Interval (ISI) inside bursts. This burst detection method is unsupervised and adaptive, i.e., it identifies bursts without any a priori knowledge of ISIs timescales. This is carried out just relying on the statistics of the time series itself. The algorithm separates short ISIs (that are more likely to belong to bursts) and long ISIs (taking place during silence periods, i.e., intra-burst intervals) by a comparison with ISIs mean. This procedure is applied again to the set of short ISIs to exclude all intra-burst intervals with high confidence. Mean burst duration has been estimated in the range between hundreds of milliseconds to seconds. Mean ISI inside bursts is in the order of few hundred of milliseconds. A representative joint ISI distribution is displayed in figure 36, along with mean burst duration and mean ISI inside bursts found with the self-adaptive method.

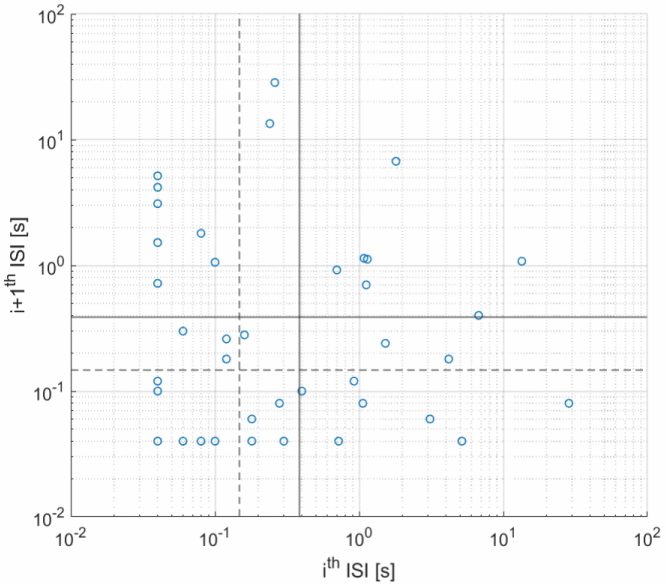

Figure 36: Joint Inter-Switch-Interval (ISI) distribution for a single switching site. Blue dots represent single TEs, and their coordinates are the ISIs between them. Solid line: mean burst duration. Dashed line: mean ISI within bursts, according to [288]. From [127].

I observed that RS in MCAF turs out to be a non-stationary process, since during the first tens seconds after the beginning of the stimulation RS events are much more frequent with respect to the rest of the measurements. The centre of mass (CM) of the conduction map (figure 37a) has been computed per each frame in order to provide coarse-grained information of the evolution of the conductance map during the stimulation. During the initial transient the CM exhibit pronounced and rapid displacements (figure 37b), indicating that RS activity is distributed across a large portion of the system. After this initial transient, the sample tends to reach a more stable conduction configuration and RS events become rarer, even if they can continue to rise till the end of the stimulation. Furthermore, after the initial transient, CM often displays sudden variations between two well defined positions, thus indicating the frequent occurrence of multiple RS events in the same location.

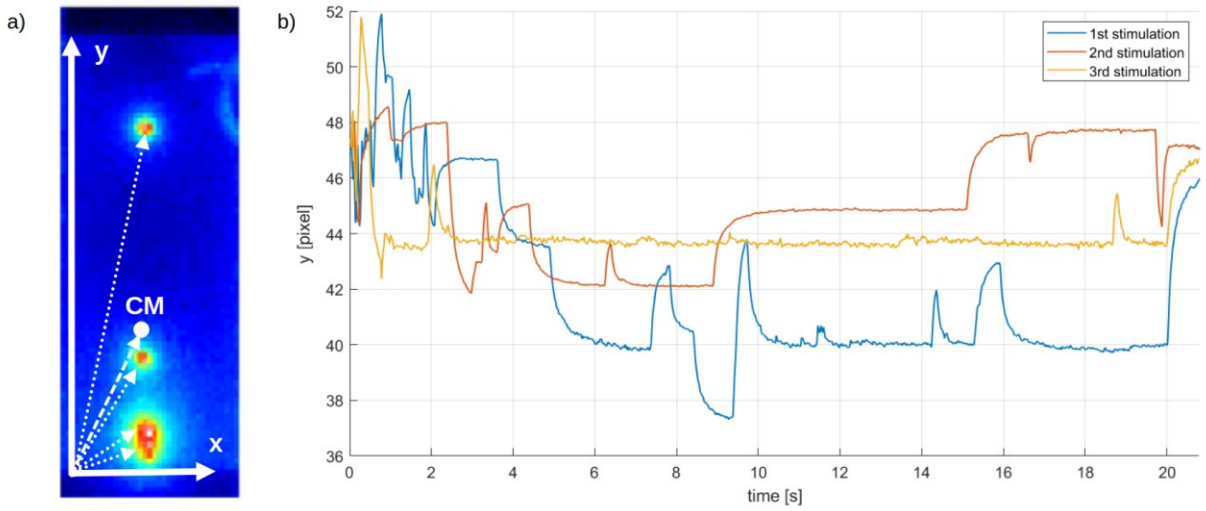

Figure 37: time evolution of the Centre of Mass (CM) of the conduction map. (a) The CM is computed as the sum of position of each pixel weighted by the absolute difference of the measured temperature from the mean. Higher weights are found in correspondence of conductive sites. (b) temporal evolution of the y coordinate of the CM during three consecutive stimulations. During the first seconds of electrical stimulation, the position of the CM undergoes sharp, chaotic variations due to intense RS activity. After this initial transient, the conduction map becomes more stable and RS events rarer. From [127].

STTC analysis could in principle be affected by the presence of two different dynamic regimes, since fictitious correlations can rise as a consequence of the temporal clustering of TEs in multiple switching sites at the beginning of the recording.

For this reason, these two dynamic regimes were disentangled by splitting the recordings in two intervals, namely, the first minute and the last four minutes, and computing the STTC separately for each. STTC has been computed for all the couples of switching sites, and results have been reported in figure 38 for a representative sample with geometry (length = 1 mm, width = 2 mm). The synchronicity window has been varied in the range 0.02 s (i.e., thermal camera sampling period) to 20 s, in order to explore the presence of switching sites coordination on different timescales.

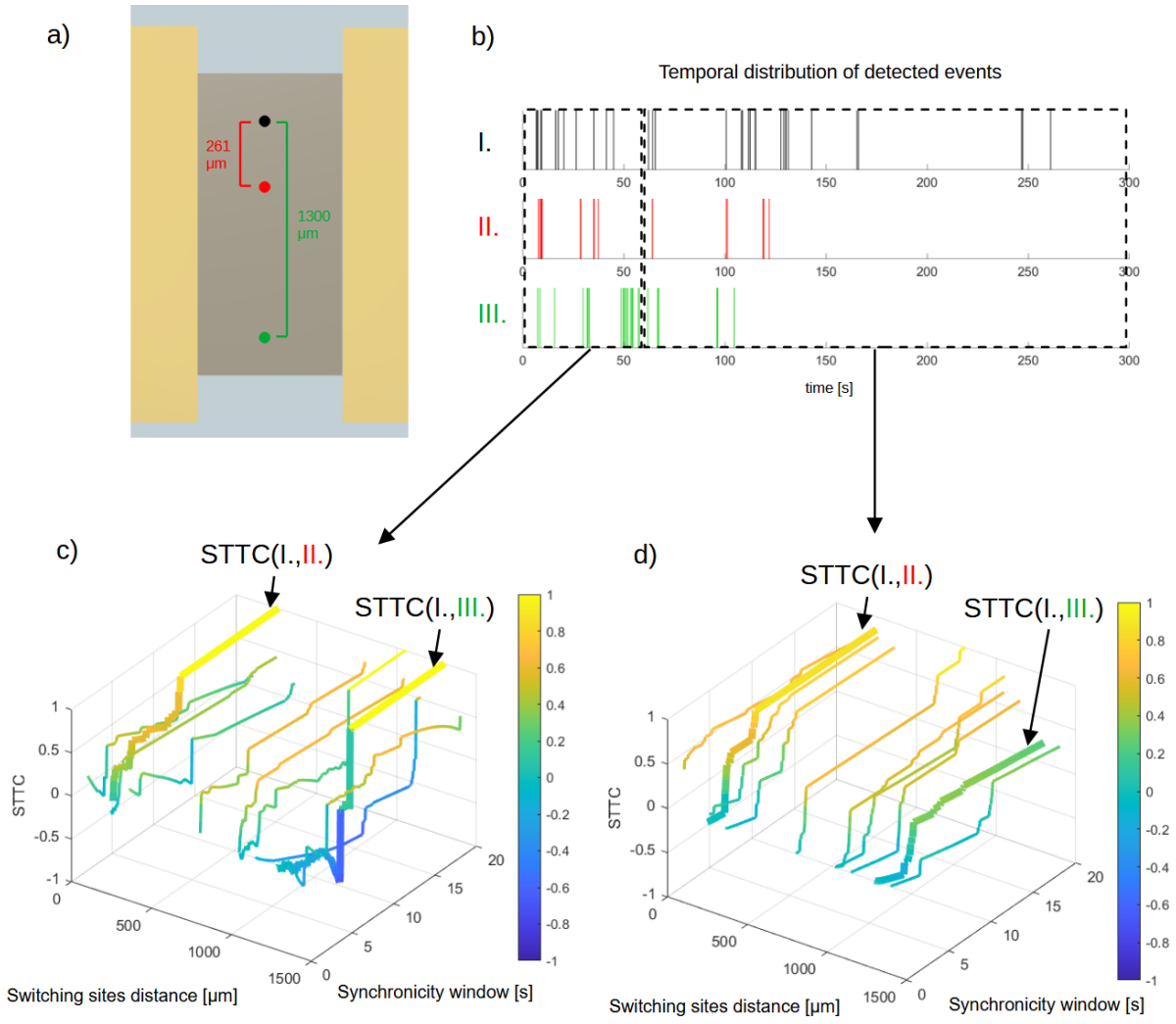

Figure 38: STTC computed for different values of the synchronicity window and distances between switching sites. (a) schematic representation of the MCAF with the locations of three switching sites. (b) Binarized time series of the RS activity of the switching sites in (a). STTC computed for (c) the first minute (interval from 0 s to 60 s) and (d) the last four minutes (interval from 60 s to 300 s) of the recording. Bold lines represent the STTC computed the time series in (b). The applied voltage is -3 V. From [127]

This analysis highlighted the absence of significant anticorrelation at every time scale, i.e., the occurrence of TEs in a switching site does not inhibit the occurrence of TEs in other switching sites. On the contrary, different degrees of coordination between switching sites are present: some switching sites display coordination on the same time scale of inter-burst activity, i.e., for synchronicity windows smaller than 1 s. In other couples of

switching sites, STTC rises significantly only by increasing the synchronicity window to several seconds or more.

Correlations are more often visible for small distance between switching sites, but this is not a rigid rule, since, in general, they have been observed also for switching sites located several hundred micrometres apart. From comparison of the analysis conducted in the two times intervals, it is possible to observe that close switching sites tend to show correlated RS activity for a longer time period, respect to sites far apart. In all the recordings, I observed a reduction in coordination during the last four minutes. This fact is consistent with the presence of burst of RS activity occurring in single switching sites. After the transient occurring at the beginning of a stimulation by a constant bias, the switching sites reach a more stable configuration and are less prone to produce RS events in response to current redistribution across the network. In this phase, RS activity is still present but tends to happen in single switching sites that produce temporally localized bursts, with less influences between spatially separated regions, similarly to the single-neuron spiking behaviour highlighted in Ref. [119].

The applied bias has a significant impact over the correlations. In figure 39 I report the results for two stimulations at 2 V (a) and 3 V (b) performed over the same sample for comparison. Other than triggering the activation of a larger number of switching sites (section 3.2.1), higher voltage bias produces much highly correlated activity, as evidenced by higher values of STTC.

Since network topology is strongly influenced by the geometry of the deposit, I also explored the impact of geometry over correlations between switching sites. STTC has been computed for all the couples of switching sites in the three different sample classes presented in section 3.2.2. Samples with small width, where typically only one or two switching sites can be detected (figure 39 c), tend to present higher STTC with respect to samples belonging to the other classes.

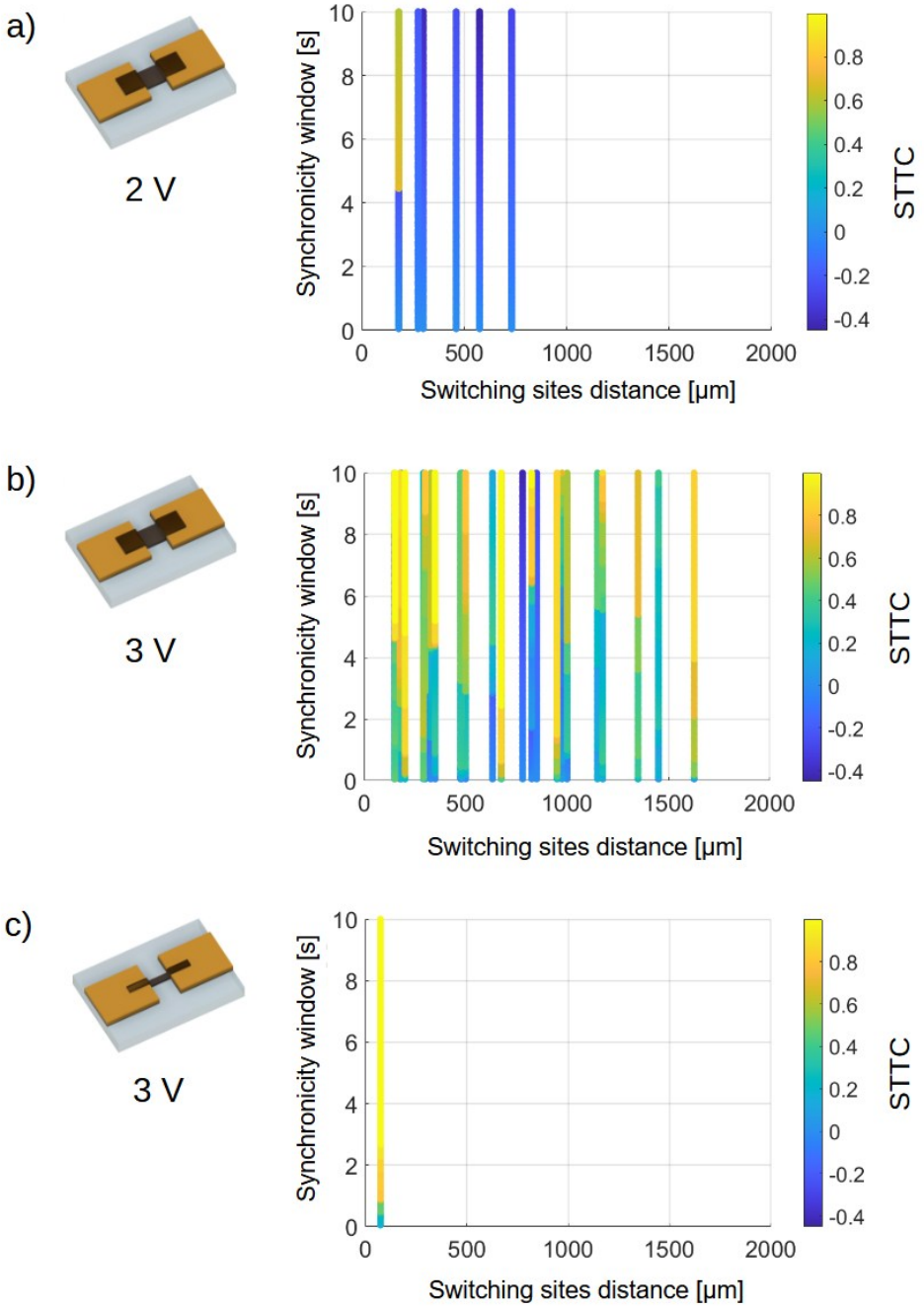

Figure 39: STTC computed by varying the applied voltage (a-b) on sample with fixed geometry (length = 1 mm, width = 2 mm) and varying geometry with fixed applied bias (b-c). From [127].

Discussion

Correlation between switching sites arises a consequence of the current redistribution following each RS event [159] (figure 40): when a conductive path is broken due to electromigration, the current (or, equivalently, the voltage) increases across other conductive paths, thus triggering additional RS events. However, it should be

noted that this phenomenology would not occur if the voltage drop were confined almost entirely in the vicinity of the groove. In such a scenario, there would be just a collection of switching elements electrically in parallel, subjected to the same constant voltage and no interactions would be possible. A significant series resistance is therefore required to enable effective current redistribution and promote interactions.

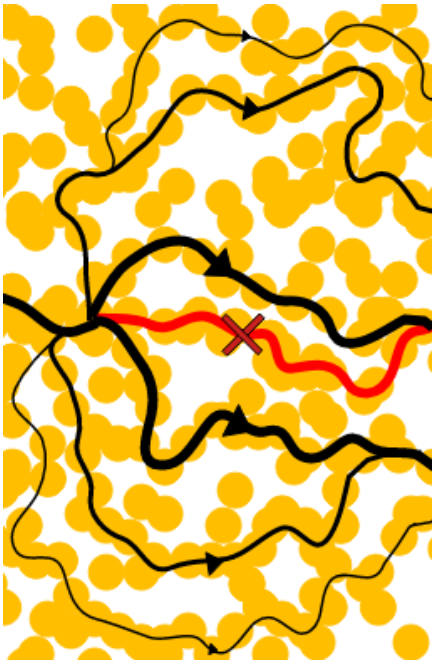

Figure 40: schematic representation of current redistribution caused by a RS event. A junction is broken (red cross) and the current is redistributed across the network. Black lines represent the increase of current density in several conductive paths. Lines thickness is proportional to the increase in current density.

This consideration is consistent with the observation that, although switching sites tend to be localized in correspondence to the groove, the wide area undergoing structural major modifications (section 3.1.2) provides a significant contribution in terms of series resistance. This can be expected, since, as deposited samples present resistances in the order of 100 Ω (less in case of small sample length), i.e., some percent of the resistance in low resistance state after forming. However, IR images clearly show that, during forming, dewetting occurs in a vast region of the sample, thus causing depercolation and a further increase in material resistivity.

In ref. [289] a phenomenology similar to the one observed in MCAFs has been reported: during the fabrication of multiple nanogaps in parallel, by means of feedback-controlled electromigration, the presence of significant series resistance is reported to trigger an uncontrollable cascade of breaking events, which was regarded as detrimental for the process. In MCAFs, by contrast, series resistance represents a key feature for inducing correlations between switching sites.

Importantly, it should be noted that differently from the case of the nanogaps discussed in ref. [289], MCAFs exhibit a reversible RS activity. In these systems, correlated switching events are not limited to cascades of ruptures, but rather involve an alternation of forming and breaking, that is typical of RS phenomena.

3.2.5 Response to time varying stimuli

The typical operation of MCAF based devices consists in two steps, namely random search and inference: during the random search a sequence of stimulations with over threshold voltage is applied in order to induce structural modifications in the film. Once a suitable conduction state is reached, it can be exploited for computational tasks during the inference phase. Reducing the duration of the stimulations during the random search is obviously beneficial, and pulsed stimulations have been employed in this phase [124]. To gain further insight into electrical behaviour of MCAF in actual device during random search, in this section I explore the electrical response of two terminal devices to pulsed stimuli.

As previously discussed in section 3.1.4, high voltage bias drives the samples in high resistance state with conductance below $10^{-6}\ \Omega^{-1}$ and no conductive paths detectable. The switch from high conductance state to low conductance state, due to the breaking of conductive path induced by joule heating and electromigration interplay is trivial to trigger. However, it is possible to switch the samples back to a high conductance state by applying smaller voltage biases. This behaviour is not trivial and has been already reported in [108] by me, and similar behaviour has been reported also on Pt cluster assembled films in ref. [260]. This phenomenology is the main subject of the current section.

I applied several stimulations in sequence on the same sample in order to trigger forming of conductive paths, and to provide uniform initial condition, I switch the sample back to the low conductance state before the beginning of the experiment. I applied the following stimulation protocol:

1) five pulses with amplitude 6 V and duration 250 ms, to drive the sample to the low conductance state. I refer to this procedure with the term *reset* operation, in analogy with memristor vocabulary.
2) thirty pulses with amplitude 2.5 V and duration 250 ms, to switch the sample back to a high conductance state. This protocol is the *set* operation.

For the set operation, two different protocols were tested. Specifically, I employed unipolar train pulses, where all pulses have the same polarity, and alternate train pulses, where each pulse has opposite polarity with respect to the previous one. The evolution of the conduction during the stimulation have been monitored with the thermal camera.

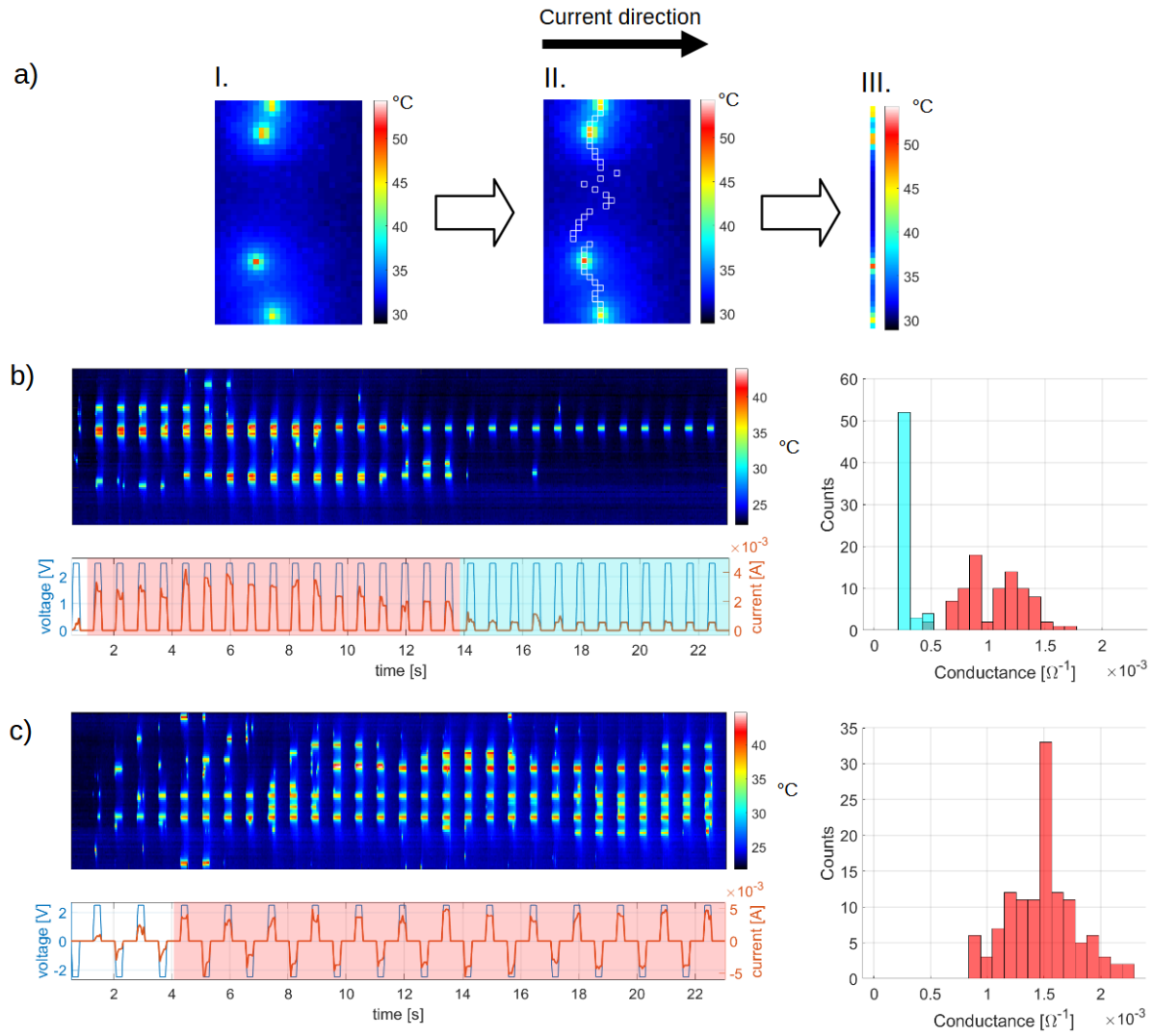

Figure 41 a) construction of the 2D map representing the evolution of the conductance during the stimulation. For each frame, a column vector has been built by stacking the temperature maxima of each row (white squares). The 2D maps in (b) and (c) have been obtained by concatenating the column vectors in horizontal direction, and represent the evolution of sample conductance for a unipolar and an alternate train pulse respectively. On the right, the distributions of the conductance measured during the stimulations. From [127]

Results

For an easier visualization of the evolution of the conduction map during stimulation, I summarize the information of each IR frame in a single column vector following the scheme in figure 41a (read caption).

Both protocols are able to retrieve the high conductance state. However, a significantly lower number of conductive paths is formed during the application of the unipolar pulse train (figure 41b), with respect to the alternate pulse train (figure 41c). Moreover, in the lase case, a high number of RS events are triggered: in fact,

a conspicuous number of paths are not stable in time, but even if they are not conductive at the end of the stimulation, they can switch multiple times during the stimulation. This phenomenology is reversible, and after every reset operation, set induces the transition to the high conductance state, by inducing the formation of multiple conductive paths.

Experiments were performed on five samples with width = 2 mm in order to exploit the camera spatial resolution, end the same phenomenology has been reported, even if some device-device variability is present, in the number of conductive paths that can be formed with this procedure and in the probability to form them. Sometimes I noticed that increasing voltage to 3 or 4 V can be effective to trigger the activation of more paths.

Discussion

The present phenomenology has strong analogies with the one reported for nanogaps [290]. These systems can reproducibly change their conductance, switching between high conductance and low conductance states. The physical mechanisms responsible for RS are likely to be similar to the case of MCAFs. Authors indicate field induced atom evaporation (EFIAE) and field induced atom diffusion (EFIAD) [291] as the main mechanisms driving the restoration of conduction. Since the absence of visible hotspots in the thermal images when samples are in low conductance state is consistent with the absence of ohmic conductive paths, and, consequently, of significant currents, these two *field* driven mechanisms are likely to be the actual responsible for this transition.

Restoration of conductance induced by field induced atom evaporation EFIAE and EFIAD has been found in metallic nanoparticles assemblies [292].

3.3 Programmability of MCAF response to electrical stimuli

In [293] Martini et al. suggest that it is possible to retrieve some degree of information about the Boolean function that will be implemented after specific sequences of writing operations (“controllability”). However, this form of “controllability” of the device, is conceptually different from the possibility to use specific writing operations to find specific target functions, i.e., “*programmability*”. Furthermore, simulations for device controllability and experimental results present some major discrepancies that are not yet fully understood. Obviously, only programmability allows to effectively optimize the writing protocol. In this section I want to address the question of receptron controllability from the opposite perspective, i.e., given a target function, is it possible to implement an efficient *programming* protocol? In section 3.2.5 I highlighted the existence of stereotyped responses to specific electric stimuli, relying on the collective response of many different switching sites. In this section I will optimize writing protocols to retrieve specific conductance states, and I will exploit the results of the optimization to drive multiterminal MCAF devices in specific resistive configurations using optimal stimulation protocols. These results indicate the possibility to establish efficient writing protocols for MCAF based devices.

3.3.1 Evidence of deterministic response to electric stimuli

In order to trigger the transition from high resistance state to low resistance state, I adopted alternate train pulses, since I found them particularly effective in restoring MCAF conduction (section 3.2.5). As I showed in the previous section, the transition is intrinsically stochastic, i.e., it is impossible to determine exactly a-priori the number and the location of switching sites that will switch in the conductive state. However, some switching sites are more likely to switch from non-conductive to conductive state, so it is often possible to reach the same conductive state multiple times during electrical stimulations. In this section I present the experiments that I performed for the optimization of the stimulation protocol, i.e., for the identification of the most significant parameters for the electric stimulus to effectively induce the transition.

I put the MCAF in high resistance state, similarly to the previous section, by applying unipolar pulse trains with amplitude 8 V. Then I applied an alternate pulse train with the aim to switch the sample back to the high conductance state. This protocol has been repeated varying three parameters in the pulse train, namely, pulse amplitude, pulse width (on-time), and number of pulses in the following ranges:

- amplitude: (1V – 4V)
- on-time: (250 ms – 1.75 s)
- number of pulses: (1-9)

the sample conductance has been measured at the end of each stimulation. Results are summarized in figure 42a-b. Repeating the whole series of experiments by shuffling their sequence of experiments, allows to rule out the influence of potential memory effects. It is immediately apparent that the effectiveness in triggering the transition is strongly dependent on the applied voltage bias, while there is a small dependence on the number of pulses, and the on-time is mostly unimportant in the range of time that has been explored.

This fact is clearly highlighted by the fitted response surface [294] shown in figure 42c: conductance after set operation has been fitted as a quadratic polynomial in all three variables, and the most apparent feature is strong non-linearity with respect to voltage. The maximum increase in electric conductance is predicted close to 2.5 V. A slight linear dependence on the number of pulses is also present, in accordance with findings of section 3.2.5, where a high number of alternate pulses allow to significantly increase sample conductance.

These results can be easily explained in the light of the previous findings: if voltage is too low, EFIAE and EFIAD cannot be triggered. On the other hand, if voltage is too high, high currents start to flow inside the newly formed conductive paths, thus inducing nearly immediate destruction via electromigration and joule heating interplay. This observation is also consistent with the results in section 3.2.2 where for voltages higher that 5 V, samples tend to explore only high resistance states, and no switching sites were detectable by means of microthermography.

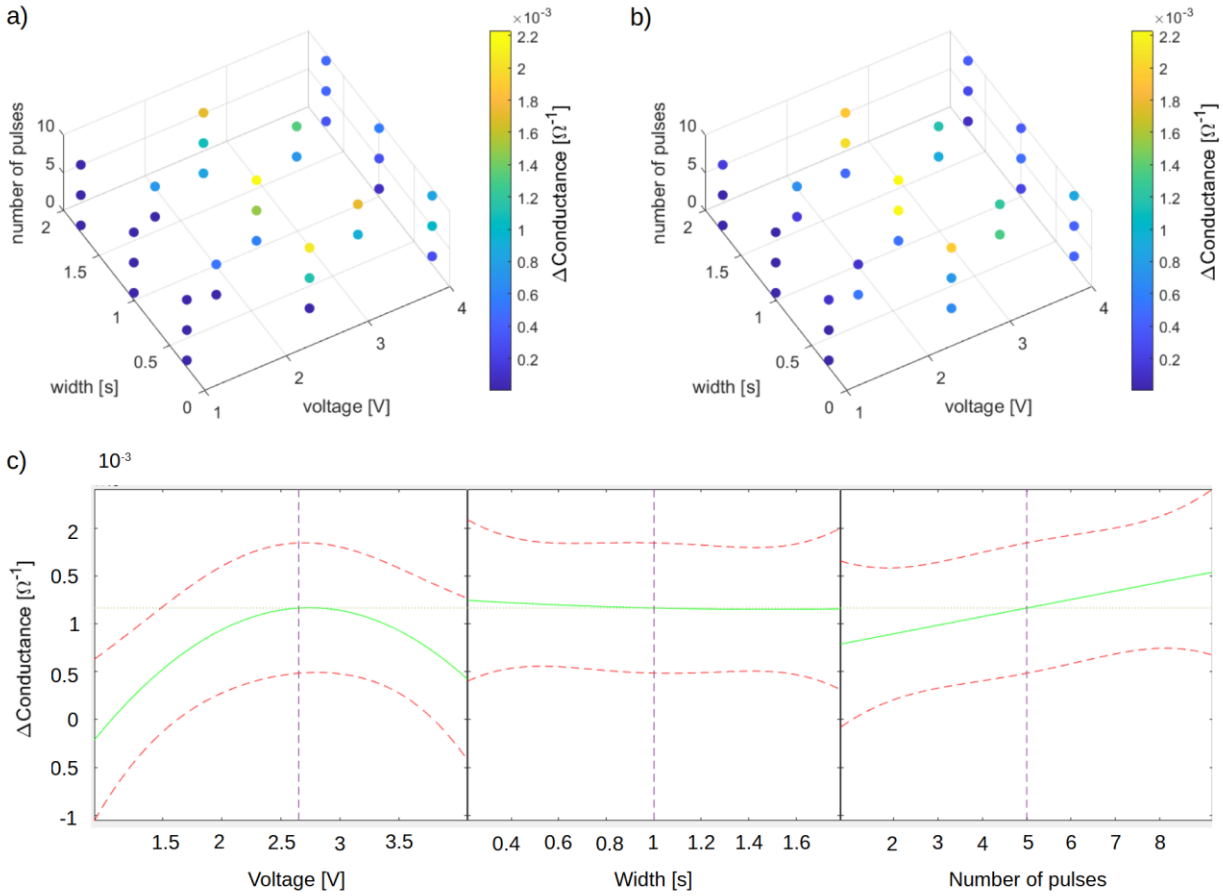

Figure 42: (a)-(b) two consecutive realizations of the experimental protocol, with different sequences of stimulations. Outcomes are similar, despite some variability due to the intrinsic stochasticity in path formation. c) surface response computed on the data represented in (a).

Notice that even if a sample can display different conductance maps after the repetition of the same stimulation protocol, the overall electrical response can be similar, if a sufficiently large number of switching sites is present. In fact, even if the electrical response of single switching sites can be significantly random and unreliable, the presence of a statistically significant number of switching sites allows to retrieve a deterministic behaviour. This phenomenology presents strong analogies with biological counterparts, where neurons are often unreliable and faulty, and high parallelization of the network allows to achieve fault tolerance.

After the optimization of the stimulation protocol that I presented in the previous paragraph, I characterized the electrical response of MCAF in standard working conditions, i.e., without any reset operation between writing operations. My goal is to characterize the electric response of MCAF depending both on *the applied stimulus* and the *current state* of the system. During an electrical stimulation, the conduction map strongly changes, and it is nearly impossible to infer the number of switching sites in conductive state at given instant. Martini et al. suggested [293], that the conduction state of MCAF after every writing operation can be described

in first approximation as a discrete-time Markov chain, i.e., a stochastic process where the transition probability between different states depends only on the current state of the system. It is obvious to consider the sample conductance as state variable of the system, and the following results will justify this assumption. In light of my previous findings, I performed other stimulations by only varying the most important parameter in the pulse train, namely, the bias, and without applying the reset train pulses. Having no way to set *a priori* a precise conductance state. The voltage bias is sorted random, and sample conductance freely varies during the experiment. I performed a series of thousands of stimulations due to the need to explore uniformly the state space. In figure 43 I plot the evolution of sample conductance after every single stimulation, as a function of the conductivity before stimulation and the applied voltage bias, that was varied in the range 0.5-6 V. The point cloud data can be better interpreted by fitting a surface with a non-parametric model. In particular, in figure 43b I show the result of fitting the data by using a Gaussian Process Regression (GPR) [295]. My GPR determines the expectation value at every coordinate in a space of parameters with discrete sampling using a Radial Basis Function kernel and iterative optimization of the scale parameter.

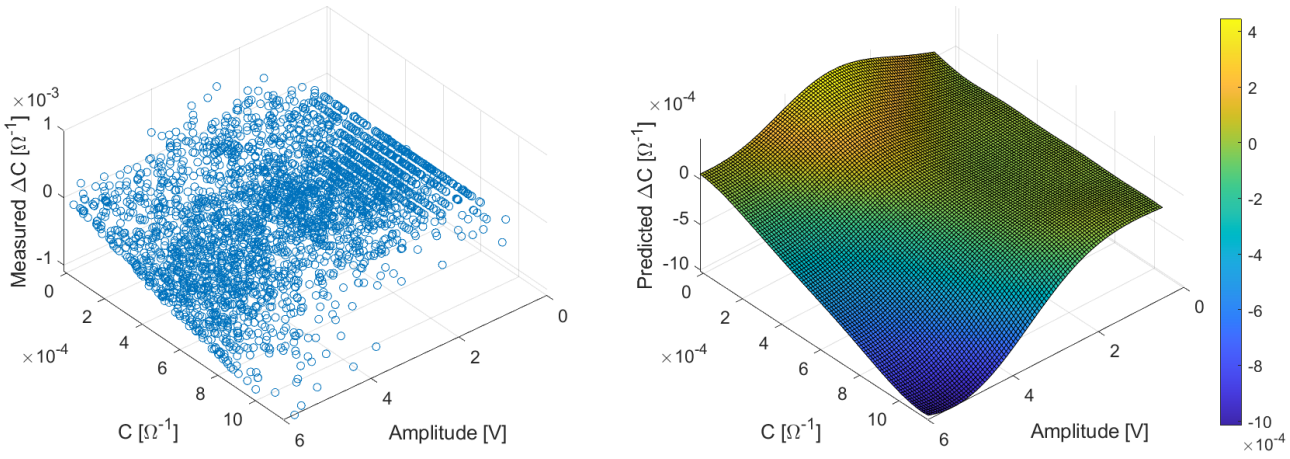

Figure 43: sample response map: a) scatter of experimental data points, b) fitted surface with GPR model.

Some interesting features are present in the electrical response of all the samples that I tested, and can be easily recognized in well defined regions of the response map:

1) In order to trigger some modification in the conductance, there is the need to apply a sufficiently intense stimulus (consistently with the fact that RS is a threshold phenomenon [121], [127]).
2) It is always possible to increase the conductance of a poorly conductive sample by applying pulses within a precise range of voltage (approximately 1 V to 3.5 V).
3) In the last case, the mean increase in conductance decreases as the sample conductance increases.
4) It is always possible to decrease sample conductance if the conductance is already not zero. This can be done by applying pulses with sufficiently high amplitude (> 4 V).
5) In the last case, the mean decrease in conductance, increases as the sample conductance increases.

I want to highlight that the response to voltage stimuli is strongly non-linear, thus giving me the possibility to effectively and reversely tune the conductivity. These features also reflect some important aspects of MCAF physics. The fact that the mean increment decreased with increasing conductance, can be easily explained by the fact that, despite the formation of a conductive path is a stochastic event, the number of available paths to be formed decrease as more of them have been already formed. Similarly, if the number of conductive paths is high, it is more likely to obtain a high decrease in conductance if the suited stimulus is provided.

It is reasonable to assume that the most important parameter driving sample evolution, along with the external electrical stimulus, is the conductance. For this reason, the conductance (or, alternatively, the number of AS in conductive state), is the state variable of the system.

Summarizing these findings: current paths are likely to form in samples in low conductance state when pulse trains with precise characteristics are delivered. Despite being paths formation a stochastic process, the increase in conductance is higher if starting conductance is low.

3.3.2 Ornstein–Uhlenbeck process: modelling the deterministic response

The phenomenology that has been presented before can be easily described by a phenomenological model, following the idea of G. Milano [296].

The time evolution of the MCAF can be represented by an Ornstein–Uhlenbeck process, i.e., a Markov process including a stochastic term, modelling noise and jumps due to RS.: the expression of a Ornstein–Uhlenbeck can be obtained by adding stochastic terms to a balance equation [297], [298].

$$\frac{dg}{dt} = \theta[\tilde{g} - g] + \sigma dW + \Gamma dq \tag{3.8}$$

where g is the state variable of the system, the stochastic terms σdW and Γdq account for noise and discrete jumps respectively, and the deterministic term $\theta[\tilde{g} - g]$ is responsible for the previously reported potentiation/depotentiation effects, and contains the state variable:

$$\theta[\tilde{g} - g] = \kappa_P(1 - g) - \kappa_D g = -(\kappa_P(V) + \kappa_D(V))g + \kappa_P(V) \tag{3.5}$$

Here, κ_P and κ_D are potentiation and depression rates, and include the physics of the RS phenomena, namely electromigration and EFIAE/EFIAD. The last ansatz is essentially the same that has been used in well-known memristor linear models (see [299], [300]), with state variables and potentiation/depression coefficients that

depend on the specific context. In the following paragraph we present an analogous model for the electrical response of MCAF, where the conductance is the state variable.

From previous studies, we know that in case of two terminal MCAF, the electrical conductance (state variable) increases with the number of conductive paths that are formed electrically in parallel, so considering all the formed current paths and their respective conductance C_{AS}^{i}, the total conductance after k writings is:

$$C_k = \sum_{i=1}^{n_{tot}} C_{AS}^{i} * AS_k^{i} \tag{3.9}$$

where I introduce the state of i-th path AS_k^{i} after k writings: $AS_k^{i} = 1$ if the path is conductive, 0 otherwise. Every conductive path presents a certain probability $p_{RESET}^{i}(V)$ to be broken after further electrical stimulation. So, it is possible to define the variation of conductance due to reset of the current paths:

$$C_k^{RESET} = -\sum_{i=1}^{n_{tot}} C_{AS}^{i} * AS_k^{i} * p_{RESET}^{i}(V) \tag{3.10}$$

Similarly, every path in non-conductive state can be formed with probability $p_i^{SET}(V)$, and I define the variation of conductance due to the formation of new current paths:

$$C_k^{SET} = \sum_{i=1}^{n_{tot}} C_{AS}^{i} * \left(1 - AS_k^{i}\right) * p_{SET}^{i}(V) \tag{3.11}$$

Even if both the conductance and the switching probability of each current path are different, it is possible to simplify these expressions introducing the mean values $C_{AS} = \langle C_{AS}^{i} \rangle$, $p_{SET,RESET}(V) = \langle p_{SET,RESET}^{i}(V) \rangle$:

$$\begin{aligned} C_k &= C_{AS} * n_k^{AS} \\ C_k^{RESET} &= -C_{AS} * n_k^{AS} * p_{RESET}(V) \\ C_k^{SET} &= C_{AS} * \left(n_{tot} - n_k^{AS}\right) * p_{SET}(V) \end{aligned} \tag{3.12}$$

This simplification holds if the number of AS is sufficiently high. The conductance at n-th writing step is:

$$C_n(C_{n-1}, V) = C_{n-1} + C_{n-1}^{RESET} + C_{n-1}^{SET} = \\ = C_{n-1} - (p^{RESET}(V) + p^{SET}(V)) * C_{n-1} + C_{AS} * n_{tot} * p^{SET}(V) \quad (3.13)$$

And the variation:

$$\Delta C_n = C_n(C_{n-1}, V) - C_{n-1} = -(p^{RESET}(V) + p^{SET}(V)) * C_{n-1} + C_{AS} * n_{AS} * p^{SET}(V) \quad (3.14)$$

Matches the expression for the deterministic term introduced by Milano [296]. The physics of the switching phenomena is entirely encapsulated in $p^{SET}(V)$ and $p^{RESET}(V)$, that take the role of potentiation and depression coefficients respectively.

Thermal images show that the linear dependence between active areas and MCAF conductance holds (figure 44). Minor deviations from linearity are there, especially in highly conductive states. This is due to increased temperature in nonconductive locations due to proximity to multiple active sites. Other minor deviations are due to non-resolvable features, e.g., the presence of multiple conductive paths in regions below camera IFOV.

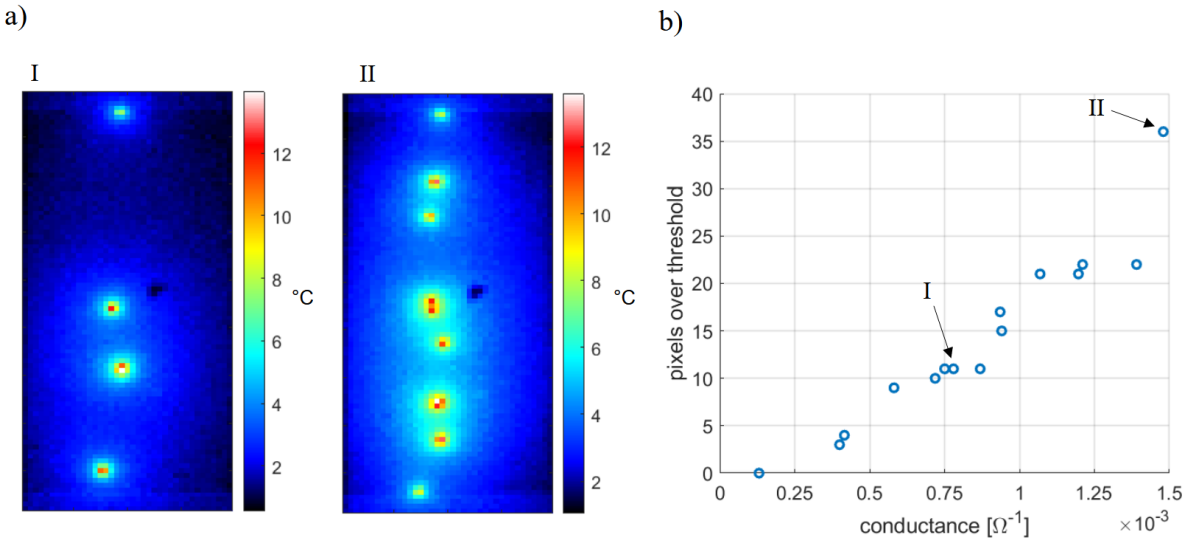

Figure 44 a) two frames of the same thermal video, corresponding to different conduction states of the sample stimulated with a constant bias of 3 V. The images are obtained subtracting a reference frame of the sample at room temperature before the stimulation, so they highlight the heating due to current flow. b) relationship

between sample conductance and dimension in pixels of the heated regions. A threshold of 8 °C has been chosen to find the heated regions. The experimental points are taken from different conductance state in the same stimulation. Lower thresholds tend to be more sensitive to heat diffusion and not to actual conductive regions, thus producing unreliable results.

3.4 Engineering MCAF based devices

Studying the electrical response of MCAF based multiterminal devices is more challenging due to the higher number of switching regions and interactions among them during electric stimulations. My goal is to show that using a simple forecast algorithm based on the information that I obtained in the context of this thesis it is possible to optimize the writing protocol, thus obtaining better performances with respect t random search.

Four terminal devices have been fabricated adopting semi-elliptical electrodes, in order to provide better uniformity in current distribution during forming (figure 45a). The deposit has circular shape with diameter of 2 mm, that is sufficient for the emergence of many different switching sites, with different degrees of correlation, thus producing an electric response that is more predictable and less prone to statistical fluctuations (refer to section 3.2.5). Forming has been carried out in two steps, following the same protocol of two terminal devices: with reference to figure 45, in the first step couples 2-3 and 1-4 were short circuited. After forming completion, the couple 2-3 is electrically formed as a two terminal device.

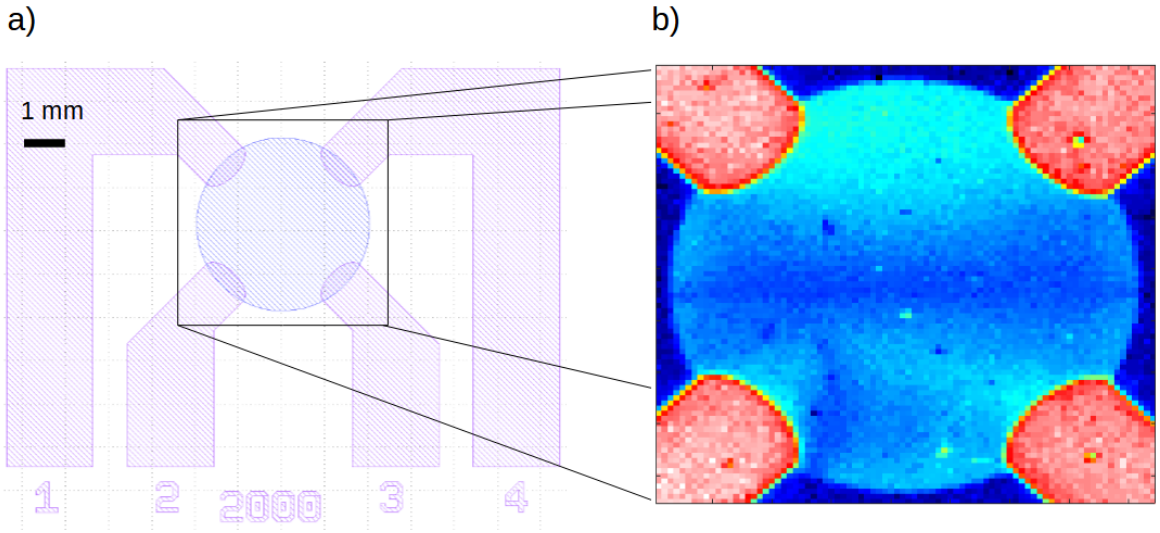

Figure 45: a) schematics of four terminal device. Pink regions are the electrodes, purple region the deposit obtained after lift-off. b) IR image of the device after forming. Darker regions highlight the major structural modifications and the grooves between different electrodes pairs.

After forming, three grooves with their respective switching sites are present between three electrode pairs. In the following discussion, I consider only the electrode pairs separated by a groove, as shown in figure 45a, namely 1-2, 2-3, 3-4. To describe this system, I employ a lumped-element resistor network model, where each resistor corresponds to a groove (figure 46a). Each groove has conductance $c_i, i = 1,2,3$ while electrodes are indicated with capital letters (see figure 46 for reference). The conductance measured between the three couples of electrodes are:

$$\begin{cases} C_{AB} = c_1 + \dfrac{c_2 c_3}{c_2 + c_3} \\ C_{BC} = c_2 + \dfrac{c_3 c_1}{c_3 + c_1} \\ C_{CA} = c_3 + \dfrac{c_1 c_2}{c_1 + c_2} \end{cases} \tag{3.15}$$

The inversion of the system can be easily done analytically (see Appendix 2), and allows to retrieve information about the conduction state of the grooves:

$$\begin{cases} c_1 = (C_{CA}C_{AB} + C_{AB}C_{BC} - C_{BC}C_{CA})D \\ c_2 = (C_{AB}C_{BC} + C_{BC}C_{AC} - C_{CA}C_{AB})D \\ c_3 = (C_{BC}C_{CA} + C_{CA}C_{AB} - C_{AB}C_{BC})D \end{cases} \tag{3.16}$$

where:

$$D = -2C_{AB}C_{BC}C_{CA}[C_{AB}^2C_{BC}^2 + C_{BC}^2C_{CA}^2 + C_{CA}^2C_{AB}^2 - 2(C_{AB}^2C_{BC}C_{CA} + C_{BC}^2C_{CA}C_{AB} + C_{CA}^2C_{AB}C_{BC})]^{-1}$$

the inversion holds only for physically realizable networks. Notice that this procedure is similar to an extremely simplified version of the ERT algorithm employed by Milano et al. in [183], [184].

Knowing the conductance state of the grooves, allows to use the information that I have collected studying the electrical response of two terminal devices to forecast the evolution of the conduction state of the entire system.

Obviously, it is crucial to deal with interactions between the evolution of different regions during the writing operation. In our simple case, if writing is done by applying the stimulus to an electrodes pair, and the third electrode is disconnected, two switching regions are electrically in series, and can effectively interact. The effect of interactions is reduced if the relative changes in conductance due to resistive switching are small, thus leading to small variations in the voltage drop. In this case, in first approximation, the switching regions evolve independently, according to the voltage drop on each of them.

Having an estimation for the evolution of the conductance state of the system allows to compare the effectiveness of different stimulation in reaching specific conductance configurations. A conductance configuration consists in a specific ordering of the conductance levels. Every configuration corresponds to a

specific target region in the states space of the system (see figure 46b). Due to the bijectivity in transformation eq. (3.16) it is possible to describe conductance state of the system in terms of the conductance of the lumped-element resistor model c_1, c_2, c_3, or in terms of the conductance measured between electrode pairs C_{AB}, C_{BC}, C_{CA}. However, the eq. (3.16) is a non-linear transformation that distorts the geometry of the space. For this reason, the second option does not provide a physically meaningful or directly interpretable estimate of how far the system is from a target configuration. In contrast, representing the system state in terms of resistor conductance allows to physically interpret the Euclidean distance in terms of excess or deficiency of conductance in switching regions. For this reason, I opted for the last solution to compare different stimulation outcomes (see figure 46b). The optimal stimulation is selected according to the following criterion: if all the forecasted data points are outside the target region, the optimal stimulation is the one associated to the forecasted point with smaller distance from the target surface, normalized with the modulus of the coordinates of the forecasted point. Normalization allows to avoid more frequent exploration of low conductance states, located near the origin (only relative proportions between coordinates matters, so a scale invariant parameter

should be used). If some forecasted data points belong to the target region, the most distant from target surface is selected. Once more, normalization is performed.

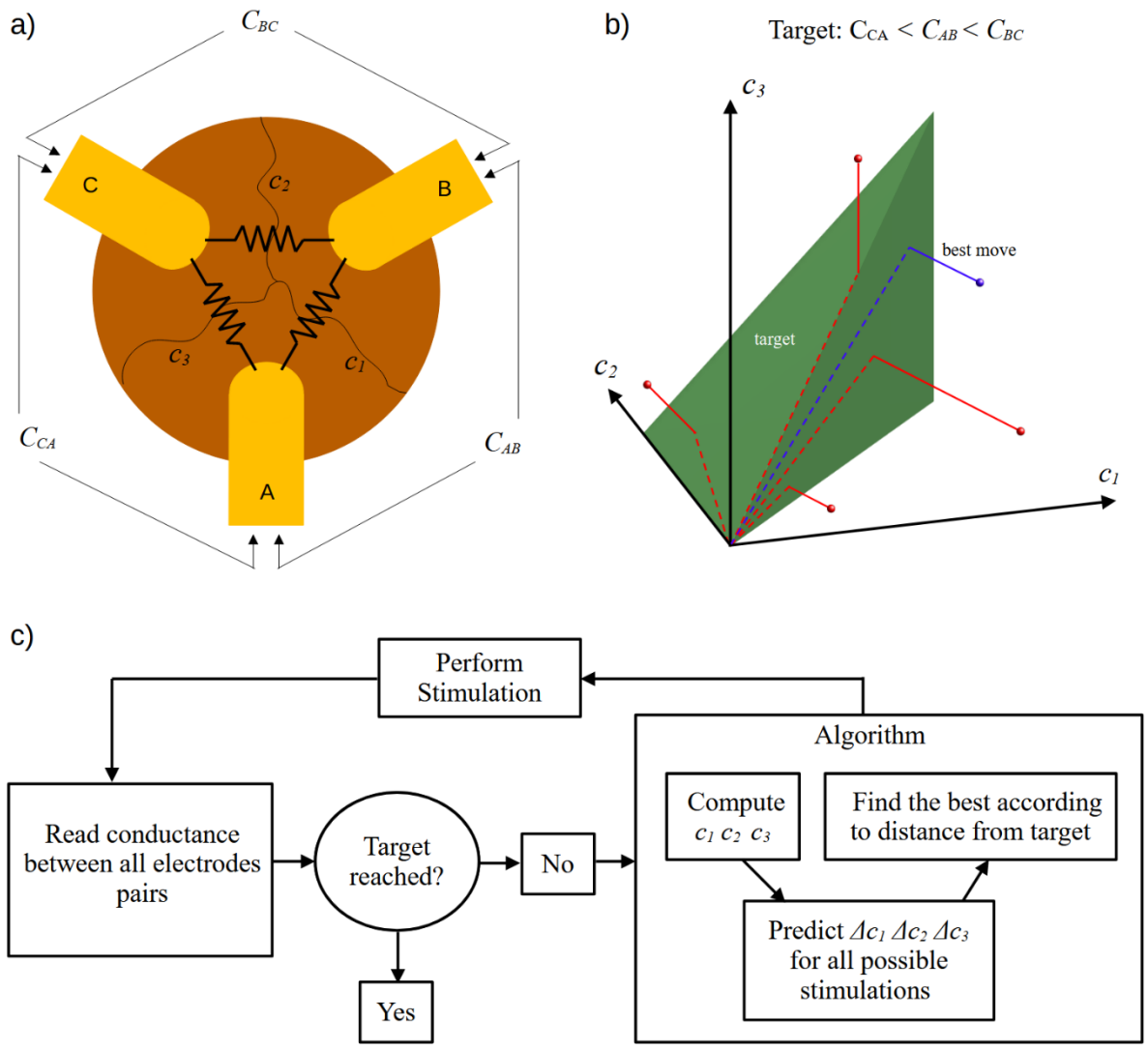

Figure 46: schematization of the multiterminal MCAF programming protocol: a) lumped-element model for three electrodes samples. b) target region corresponding to a specific order of conductance levels. Dots represent the predicted conduction state of the system after different stimulations. Dashed lines are the projections of the predictions over the target surface. The blue dot is the best move according to the rule presented in the main text. c) schematics of the algorithm.

The complete algorithm is schematically depicted in the diagram in figure 46c:

1) conductance between all electrode couples is measured.
2) Then, if target has been already reached, the search ends.
3) If target is not reached, resistors conductance in the lumped-element resistor model are computed, and for different stimulations, we compute the forecasted variations in conductance.

4) The best stimulation is selected according to the criterion described previously.
5) Stimulation is performed, and the algorithm goes back to 1).

I exploited this protocol to implement all the six different targets on three terminal devices in a precise sequence. I forecasted the outcomes for nine possible stimulations, namely three different bias voltages for each of the electrode couples. Then I repeated the experiment by random sorting the stimulation protocol (i.e., random sorting both electrode couple and voltage bias), similarly to [120], [121].

I found out that in samples presenting high conductance due to the presence of numerous conductive switching sites, this programming algorithm allows to implement all the targets more efficiently than the random search (see figure 47). Typically, the first requires half of the steps than the second.

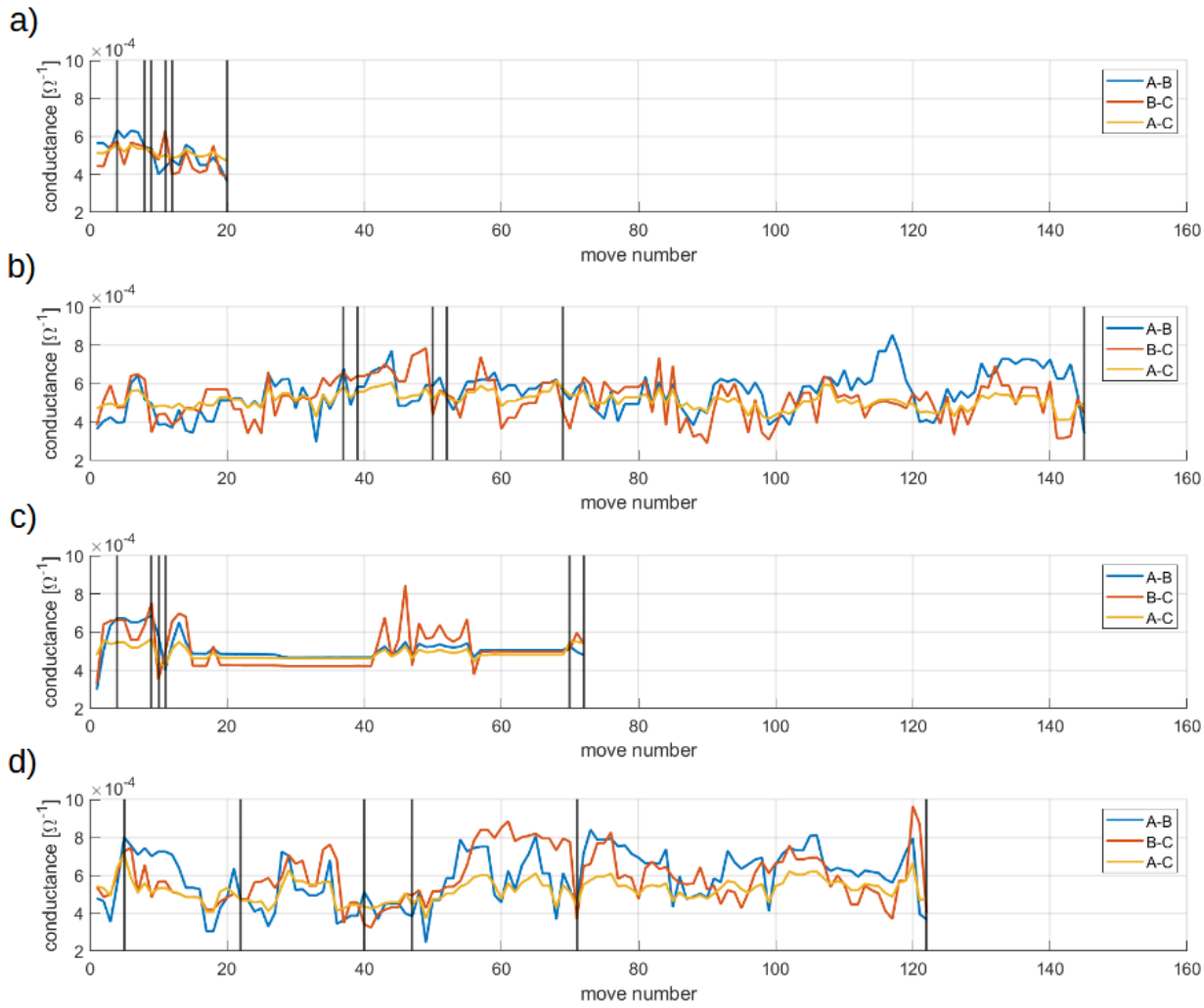

Figure 47: evolution of the measured conductance between the three electrodes couples during four series of stimulations. a-c) optimal voltage bias and stimulated couple are chosen according to the algorithm. b-d) voltage bias and stimulated couple are random sorted. Vertical black lines indicate the reaching of specific conductance configurations. The sequence of configurations to reach is the same in each case, but with different number of stimulations. A GPR model has been used to model groove responses.

If the samples are more prone to explore low conductance, the hypothesis regarding absence of interactions does not hold anymore, and the algorithm tends to fail more often.

As expected, (see section 1.5) some configurations are significantly more difficult to implement with respect to others: I often see the deterministic algorithm effectively implementing most combinations in few steps, while significantly longer times are required to implement the remaining. In figure 47c, for example, more

than sixty writing steps are required to implement the fifth configuration, while significantly fewer steps are required for all the others. A possible approach to overcome this issue is to explicitly account for these interactions inside the model. However, this strategy comes at the cost of introducing additional parameters, which not only significantly complicates the computation but also scale exponentially with the number of electrodes. As an alternative, one could reintroduce stochastic moves ad-hoc in the writing process, allowing the system to efficiently sample the state space and recover problematic configurations that a too simplistic model would otherwise fail to reach.

4 Conclusions

In this work I studied the complex electrical behaviour of metallic cluster assembled films (MCAFs) for specifically focusing on the possibility to engineer MCAF-based devices for neuromorphic computing applications. To achieve this goal, I employed a novel experimental strategy complementing electrical characterization with thermal imaging that allowed to map the conduction state of the nanostructured system. The information that I retrieved from IR imaging provided insights into the morphological modifications occurring during forming process. Furthermore, it allows to monitor in real time the evolution of the functional connectivity of the network during electrical stimulations.

This novel analysis allowed me to identify some specific regions of the film that are responsible for resistive switching (RS) activity, i.e., the switching sites. MCAF response to stimuli is orchestrated by the interactions between different switching sites, and different level of correlation are present, thus reflecting a complex functional topology with significant analogies with the biological counterparts.

I further demonstrated that the geometry of the deposit has a strong impact on both the number of switching sites and correlations, suggesting that device geometry can be exploited as a design parameter to implement task-specific functionalities.

Despite RS is intrinsically a stochastic phenomenon, MCAFs showed a stereotyped response to fast electrical stimuli. From my experimental evidence, I suggest that the mechanisms of Electric Field Induced Evaporation and Electric Field Induced Diffusion contribute to this phenomenon, thereby advancing our understanding of fundamental mechanisms underlying RS.

Starting from all the evidence that I collected in this study, I addressed the question of controllability of MCAF-based devices, that is crucial for the optimization of receptron training protocols. I explored different possible stimulation protocols, and I optimized the transition from low conductance state to high conductance state. The effectiveness of the protocol depends primarily on the applied voltage, confirming the existence of a voltage-activated mechanism for the set operation.

I carried out additional simulations and experimental characterizations to investigate the possibility of tuning the voltage bias in order to modulate the device response according to its current conductive state and a desired target conduction state. A model that effectively captures the key features of MCAF response has been developed. Moreover, the feasibility of employing efficient programming protocols has been demonstrated, offering a valuable option for optimized training strategies.

Controllability relies on the peculiar features of MCAFs. Individual switching sites are intrinsically unreliable and stochastic. However, significant number of switching sites, with non-trivial interaction orchestrating the complex dynamics, allows to display a reproducible and deterministic response. This emergent behaviour

presents significant analogies with biological neural networks, where reliable functionality arises from the interplay of inherently noisy elements.

Appendix: Optimization of electrodes geometry in multiterminal devices

As already pointed out for two terminal devices with different geometries (see section 3.2), the size of the region undergoing major structural modifications during forming process has a strong impact on the richness and statistics of RS, as long as non-linear conduction properties: in fact, along with sample geometry, it is responsible for both the quantity of switching sites and functional topology of the MCAF. For these reasons, to engineer the electrical response of MCAF and improve reproducibility, it is of paramount importance to finely control MCAF forming process and exploit this procedure to reliably drive samples to predetermined conductive configurations. In this paragraph I address the topic of electrode design for controllable and reproducible MCAF forming process by means of simulative studies. Reliability and reproducibility issues are quite often met in the fabrication of innovative devices for neuromorphic computing applications. A paradigmatic example can be found in many classes of filamentary memristors: the initial forming process presents a certain degree of stochasticity, leading to unpredictable growth of the conductive filament and subsequent inter-device variability in electrical characteristics and performances. In this cases, electrodes design optimization has been systematically performed with the aim to obtain a localized electric field that drives a more controllable and reproducible filament growth [301], [302]. In my case of study, MCAF functionality for unconventional computing applications relies on the presence of a high number of current paths and switching regions electrically in parallel. For this reason, my perspective is substantially different from [301], [302]: my goal is to induce structural modifications on an extended region of the deposit.

Joule heating and electromigration jointly trigger all the processes that lead to morphological and structural modifications (see Materials and Methods) and need to be carefully taken into account. Current density is the direct responsible for both joule heating (see equation 2, in Materials and Methods), and electromigration, and for this reason it is important to retrieve information about current distribution in the devices. Current density in any location $\vec{x}$ of the system is linked to the electric field by the well-known Ohm law:

$$\vec{j} = \bar{\bar{\sigma}} \cdot \vec{E} \tag{A1.1}$$

Where the superscripts denote the vectorial and tensorial nature of the current density/electric field and conductivity respectively, and we do not explicit the dependence on the position in $\vec{E} = \vec{E}(\vec{x})$ and $\bar{\bar{\sigma}} = \bar{\bar{\sigma}}(\vec{x})$. In a steady state conduction problem, magnetic transients are absent, the electric field is irrotational, and can be retrieved from the gradient of the electric potential:

$$\vec{E} = -\vec{\nabla}V \tag{A1.2}$$

If no charge accumulation is present (as it should be in a good conductor in steady conduction), the current density is solenoidal

$$\vec{\nabla} \cdot \vec{j} = 0 \tag{A1.3}$$

And from (A1.2) and (A1.3):

$$\vec{\nabla} \cdot \left(\bar{\bar{\sigma}} \cdot \vec{\nabla}V\right) = 0 \tag{A1.4}$$

In case of uniform and isotropic conductivity, this equation reduces to the more familiar Laplace equation.

$$\vec{\nabla}^2 V = 0 \tag{A1.5}$$

the conduction problem turns out to be scale-invariant under geometrical similarity, since equation (A1.4) can be easily rewritten in terms of dimensionless quantities $\bar{\bar{\sigma}}' = \bar{\bar{\sigma}}/\sigma_0$, $\vec{x}' = \vec{x}/L_0$ $\vec{\nabla'} = L_0\vec{\nabla}$, and $V' = V/V_0$:

$$\vec{\nabla'} \cdot \left(\bar{\bar{\sigma}}' \cdot \vec{\nabla}'V'\right) = 0 \tag{A1.6}$$

Where σ_0, L_0 and V_0 are reference values for conductivity, length and electric potential. Current density can be easily retrieved as:

$$\vec{j} = -\frac{\sigma_0 V_0}{L_0}\vec{\nabla}'V' \tag{A1.7}$$

In the last part of this section, results are presented in dimensionless units for a more general description.

In summary, the problem of finding the current density reduces to the solution of (A1.5) (or (A1.6)) over the sample domain, where the boundary conditions are defined by the location of the electrodes and the specific stimulation protocol. Once again, I adopted MATLAB built-in partial differential equation (PDE) toolbox to find an approximate solution of the (A1.5) in different simulated systems, by means of Finite Element Method

(FEM), as previously mentioned in Chapter 2. A triangular mesh has been employed. Being MCAF quasi 2D materials, I employed planar models to describe conduction. The geometry of the conductive regions at the nanoscale is obviously complex and non-easily accessible. For this reason I adopted a coarse grained model with the value $\sigma = 5 * 10^5\ \Omega^{-1}$ for electric conductivity in agreement with those reported in literature [144], [145]. Thickness was set to $20\ nm$, and the sheet resistance was computed accordingly for the 2D model. The minimum diameter of the mesh has been set to $20\ \mu m$, i.e., sufficiently large with respect to the nanometric features for coarse grained assumption to hold. Thickness inhomogeneities could be present in real samples, thus compromising the validity of the model, but spatial uniformity in cluster deposition using SCBD and PMCS has been already demonstrated on millimetric surfaces.

First of all, I address the case of two terminal devices described at the beginning of this chapter, that turn out to be also the easiest system to address. In figure 48a is reported see a schematization of the rectangular MCAF deposit. In the following, I will use a colour code to schematize the boundary conditions: red and blue lines represent the interfaces with the electrodes that are set to high and low potential respectively. All the other boundaries, depicted with black lines, are insulating, as they should be, since no current flows towards the substrate or the atmosphere. This property is described by the Neumann condition $\vec{\nabla} V = 0$ in the direction perpendicular to the border.

The solution of (A1.4) in the devices represented in figure 48a can be easily obtained also analytically: the current density field is uniform over the sample (figure 48b).

Things become much more complicated if the dimension of the electrodes are shrunk with respect to the dimension MCAF deposit, with the aim to fabricate multiterminal devices: in this case, planar, straight electrodes cannot be used anymore, and the shape of the electrode-MCAF interface has a strong influence over the current distribution inside the sample. Three main effects have been identified to be responsible for strong current density inhomogeneities:

1. first, if the shape of the electrode includes sharp vertexes, these are responsible for further, strong increase of the electric field (and electric current) due to apex-field enhancement [303].
2. Electrodes separation is another parameter that should be carefully considered. If electrodes are close to each other, the current tends to be localized, thus improving uniformity near the edges but strongly limiting the distribution thorough the rest of the sample. On the other hand, if electrodes are far apart, the current is effectively distributed across the sample.
3. Finally, relatively small electrodes will collect electric current that is distributed over a much larger sample, thus leading to a strong increase in current density in proximity of the electrode-MCAF interface: using relatively large electrodes is always beneficial. However, the dimension of the electrodes in multielectrode devices is generally limited by geometrical constraints.

All these three factors tend to localize the structural modifications due to the forming process to the immediate vicinity of the electrodes or in a narrow gap between them. For these reasons, optimal design solutions should take into account the interplay of electrode shape and electrodes separation in producing current inhomogeneities in all the domain, in order to mitigate both the effect discussed in (1) and (2).

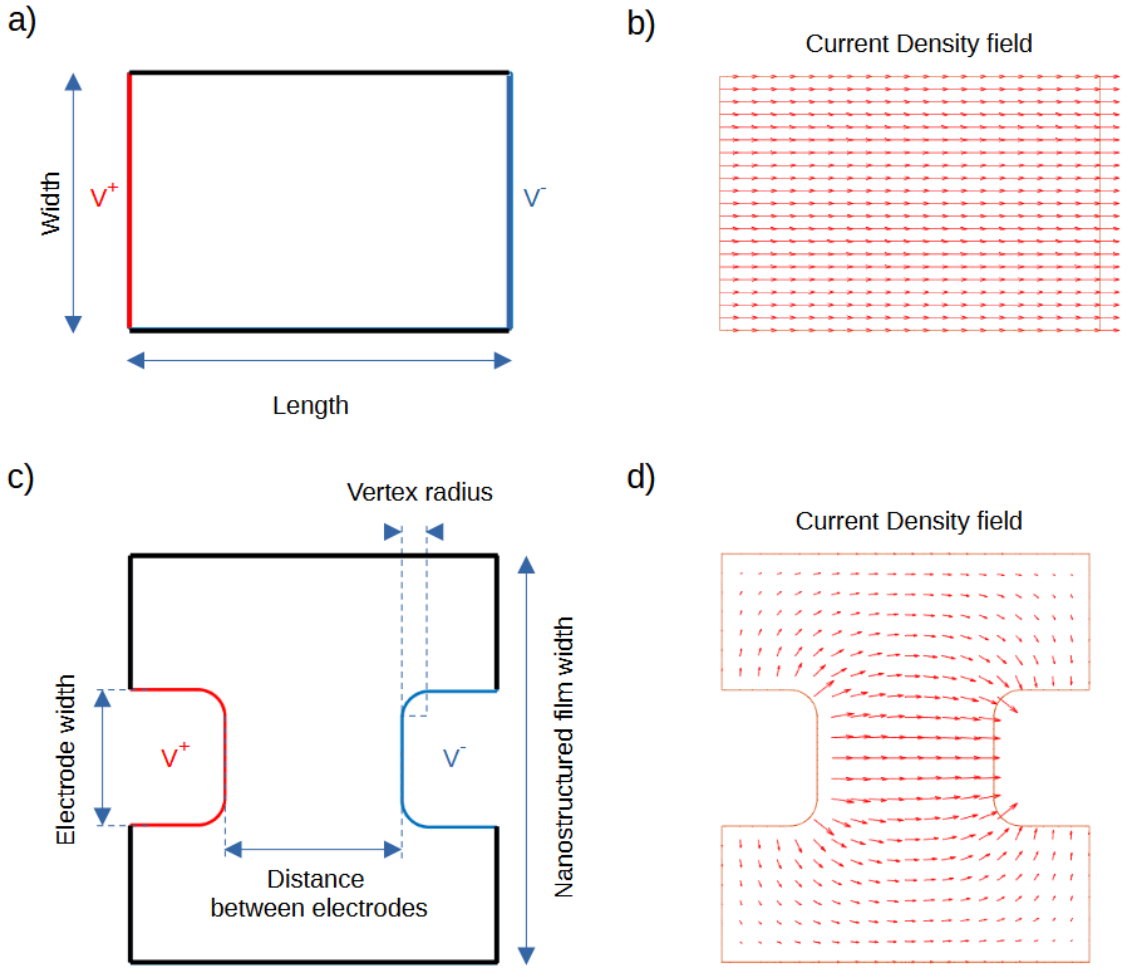

Figure 48: a) schematization of the geometry and boundary condition for a two-terminal sample with straight electrode interfaces. Surfaces at high and low potential are represented in red and blue respectively. black edges are insulating. b) current density field computed by means of FEM algorithm. Referring to the nomenclature in figure 1a, the physical parameters are the following: length = 1.8 mm, *width = 1.2* mm, $V^+=10$ V, $V^-=0$ V. *c) schematization of the geometry and boundary condition for a two-terminal sample with square electrode interfaces, and round vertexes. d) current density field computed by means of FEM algorithm. Referring to the nomenclature in figure 1a, the physical parameters are the following: distance between electrodes = 0.65* mm, *electrode width = 0.5* mm, *vertex radius = 0.1* mm, $V^+=10$ V, $V^-=0$ V.

Rounded edges are generally employed to dampen field enhancement effect (see figures in [124], chapter 3) described at point (1). However, care should be also taken to mitigate the effects of current confinement. In order to clarify this point, consider the optimization of the system depicted in figure 48c, where squared electrodes with round edges have been employed, and the same colour code of figure 48a for the boundary conditions has been used (see caption). Later on, I will refer to this configuration as a *squared geometry*. Two limiting scenarios could be met. First, vertex radius is small, and a large portion of the electrode edge is straight. In this case, good current uniformity can be achieved in the central region, but the field enhancement still leads to an increase of the current density near the vertexes (figure 49a). In the opposite situation, vertex radius is large, and the shape of the electrode collapses into a semicircle. In this case, the apexes of the electrodes are closer to each other with respect to all the other regions of the two interfaces, inducing current localization and giving rise to a local increment of the current density in the region between the tips (figure 49b), as explained at point (2). This effect is likely to induce the strong modifications reported in [124] near the tip of the round electrodes (figure 3-7). Notice that the distance between the electrode is the same in figure 49a and figure 49b, and the reported effects are only due geometry of the electrodes.

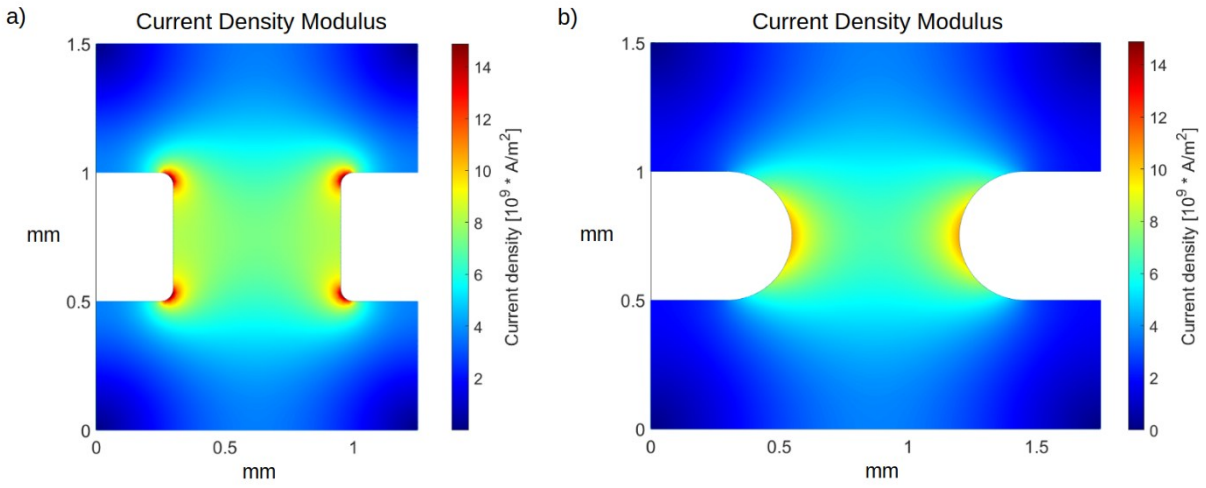

Figure 49: current density modulus for two different electrode geometries: a) vertex radius = 0.1 mm. Field enhancement causes strong increment of current density in proximity of the vertexes. b) vertex radius = 0.24 mm. The current density is higher near electrodes apex, due to current confinement.

In the squared geometry configuration, the shape of the electrodes can be engineered for having less pronounced current density inhomogeneities by optimizing the vertex radius according to electrodes separation. In the following discussion, results are presented referring to the dimensionless formulation (A1.6). In particular, the two geometrical parameters, namely, vertex radius and electrodes separation, have been normalized using the electrode width as reference (L_0 in (6)). I will refer to these dimensionless quantities as vertex radius and electrode separation for simplicity, keeping in mind that they have been normalized. I solved

equation (A1.4) in a series of realization of the system described in figure 1c by varying the vertex radius from 0.02 to 0.5 (round profile), and electrodes separation from 0.4 to 4.

Current density uniformity in these simulations can be assessed by comparing the current density modulus at the centre of the domain (A, in figure 50a) with the maximum (MAX) value across the entire mesh (that, in any case, is located in proximity of the electrode, as shown in figure 49a and b). To further quantify uniformity along the axis perpendicular to the stimulation direction, I also consider the current density at the intersection between the vertical axis of the domain and the prolongation of the electrode edge (B, in figure 50a).

In figure 50b-d I report the results of the simulations, expressed in terms of ratio between current densities j_{MAX}, j_A, j_B at the location MAX, A, B, respectively.

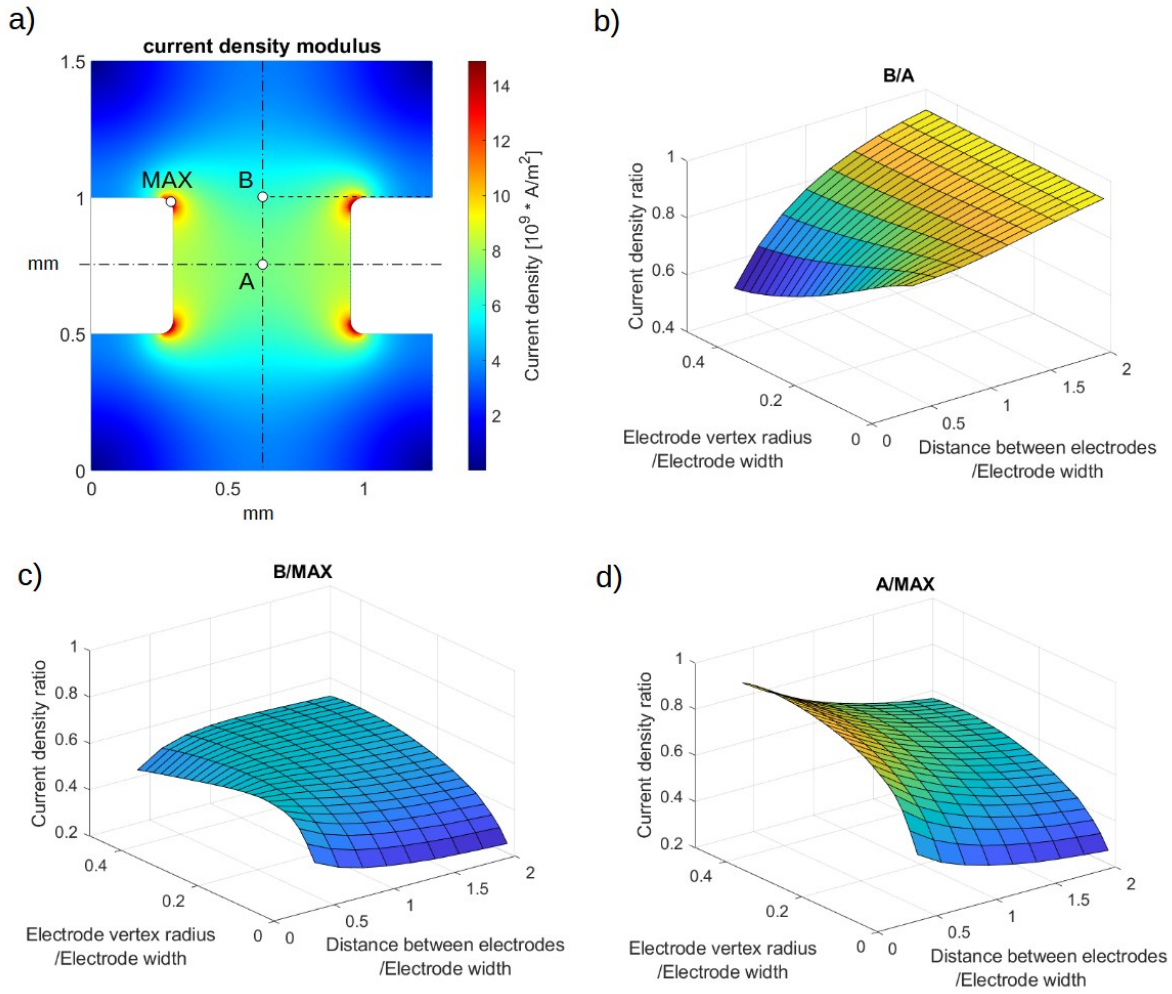

Figure 50: a) current density modulus in simulated system with vertex radius = 0.05 mm, distance between electrodes = 0.65 mm, bias = 10 V. The locations A and B that we monitor in the following analysis are displayed. The location of maximum current density is displayed as well. b) ratio of current densities in B and

A. c) ratio between current density in B and maximum current density. d) ratio between current densities in B and maximum current density.

First of all, it is possible to observe, from comparison of figures 50b-d that high distance (>1.5) between electrodes leads to minor current confinement, or conversely, effective current distribution across the domain: in this situation, the current density in location A and B is similar (j_B/j_A exceeds 0.9, figure 50b) irrespective of electrodes geometry. However, the current density is higher near the electrodes, as immediately apparent since $j_B/j_{MAX} < 0.7$ and $j_A/j_{MAX} < 0.7$ (figure 50c-d). Having a small vertex radius leads to a drastic increment of the current density near the vertexes due to field enhancement, thus causing a drop in the ratio j_A/j_{MAX} and j_B/j_{MAX}.

If the electrodes are close to each other, the current tends to be highly confined: in fact, the ratio j_A/j_{MAX} increases significantly with decreasing electrodes separation while j_A/j_{MAX} remains constant or even decreases, thus indicating current localization in the direction of the horizontal axis in figure 50a. Current confinement is reflected in the significantly lower values of j_B/j_A for electrodes separation < 0.8. Current inhomogeneity is exacerbated for large vertex radius, as expected from the previous considerations. Conversely, it is possible to notice that a small vertex radius can effectively mitigate this effect, as $j_B/j_A > 0.75$ is always achievable with vertex radius <0.1.

Finally, it should be noted that current confinement due to round tips typically produces less intense current density peaks with respect to field enhancement due to sharp edges, as it is also apparent by comparing figure 49a and figure 49b. This consideration partially justifies the common practice to deal only with field enhancement.

It is possible to summarize these results in the following way: if electrodes separation is large (>1, for reference) the current tends to be highly uniform in the central region the domain, almost irrespective of the shape of the electrodes. In these cases, a roundish geometry is preferred, for limiting field enhancement near the electrode edges. If electrodes separation is small (<1), the current is unavoidably more confined in the gap between the electrodes. In these cases, uniformity in the central region can be improved by adopting a small vertex radius.

A valuable alternative shape for electrodes consists of a rectangle where one side is substituted by a semi-elliptical arc, continuously connected to the neighbouring edges (figure 51a). I will refer to this configuration as a *semi-elliptical geometry*. Ellipses naturally conjugate different curvatures, thus helping in balancing field enhancement with the effect of proximity. Once again, the shape of the electrodes can be optimized to improve current uniformity. I performed simulations in the vein of that we have just presented for the squared geometry.

In this case, I tune the shape by varying the dimension of the ellipses semiaxis (see figure 51a for reference), in place of the vertex radius. The distance between the electrodes is defined as the distance between the closer

edges, as in figure 48c. Both these quantities have been normalized by the electrode width, as we already done in the former case.

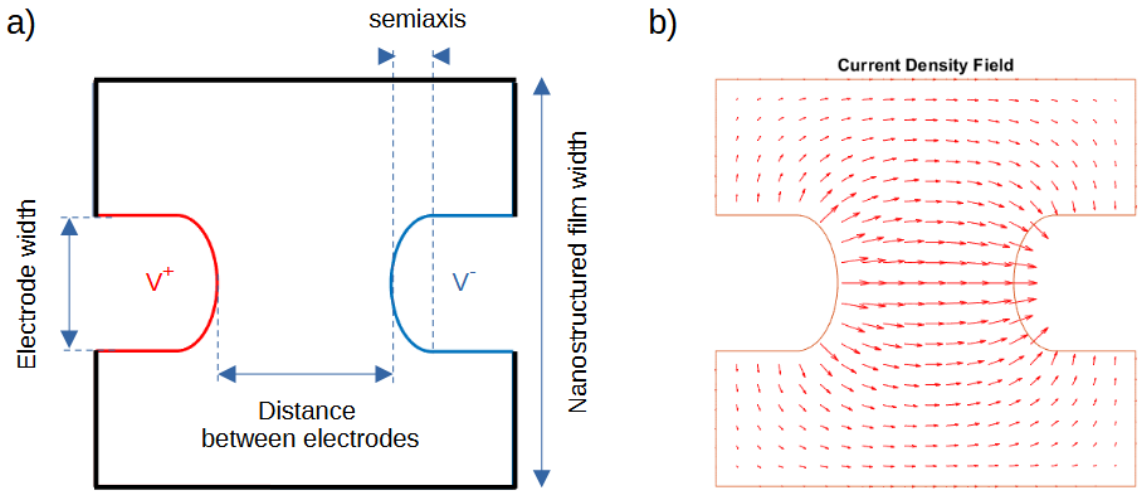

Figure 51: a) sketch of the domain with semi-elliptical electrode geometry. Surfaces at high and low potential are represented in red and blue respectively. black edges are insulating. b) current density field computed by means of FEM algorithm.

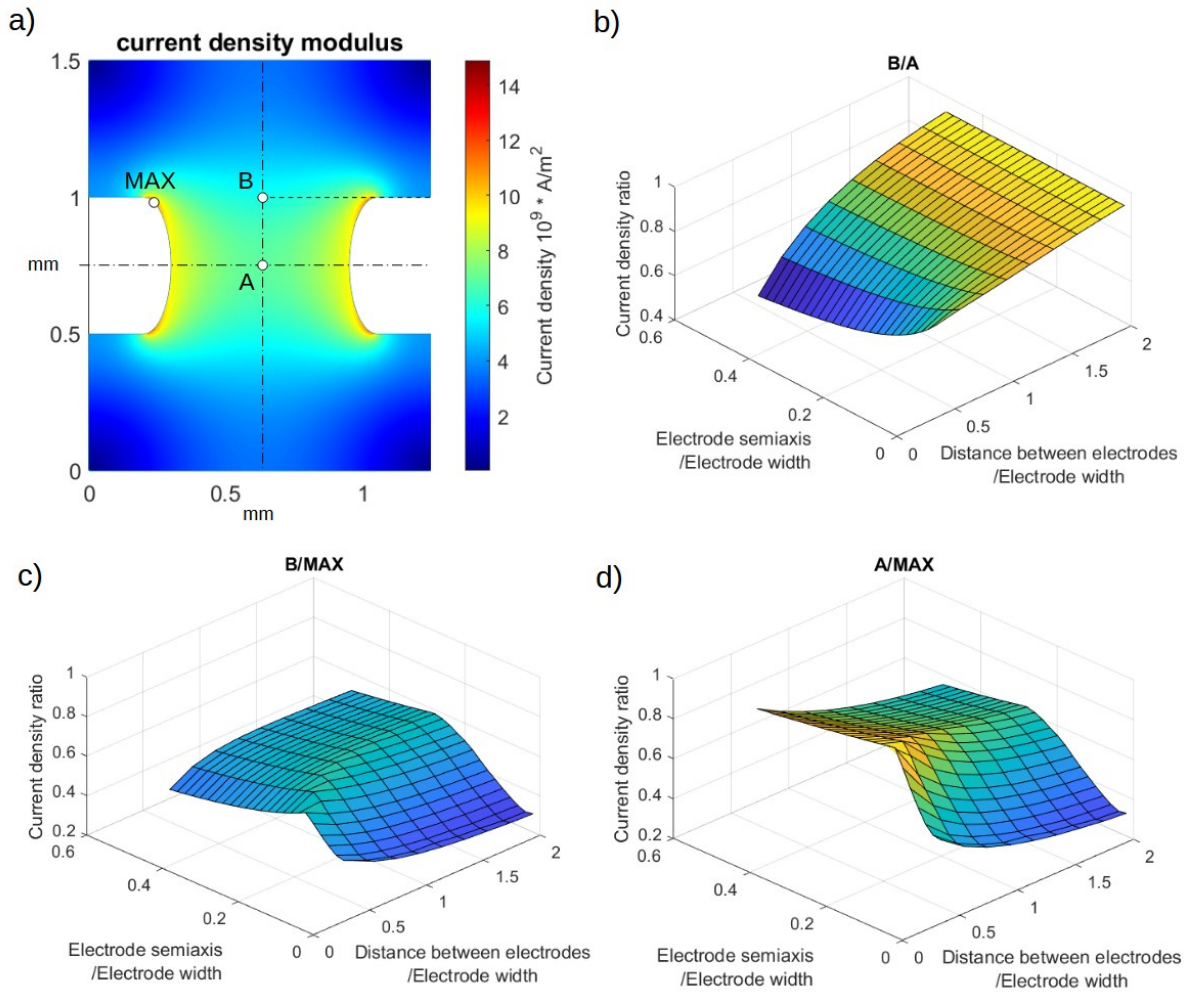

Figure 52: a) current density modulus in simulated system with electrode semiaxis = 0.1 mm, distance between electrodes = 0.65 mm, bias = 10 V. The locations A and B that we monitor in the following analysis are displayed. The location of maximum current density is displayed as well. b) ratio of current densities in B and A. c) ratio between current density in B and maximum current density. d) ratio between current densities in B and maximum current density.

Once again, I monitored the modulus of the current density at the two locations A, B (figure 52a), as well as the maximum current density over the domain.

The same qualitative features that emerge from the results of the previous simulations are still present with the new geometry, with simple replacement vertex radius ↔ semiaxis: for large electrodes separation, there is an effective current distribution across the domain ($j_B/j_A > 0.9$ for electrodes separation > 1.5) irrespective of electrodes geometry. Small electrode semiaxis are always responsible for an increase of field enhancement effects and cause a drop in the ratios j_B/j_{MAX} and j_A/j_{MAX}. However, for small electrode separation, current

tend to be localized, and uniformity can be improved by using small semiaxis (namely, more "straight" electrodes).

By comparison with previous results, it is easy to notice that the semi-elliptical geometry can significantly improve the overall current uniformity. In figure 53a-b I plot j_B/j_{MAX} and j_A/j_{MAX} as a function of vertex radius for squared geometry and semiaxis for semi-elliptical geometry, for fixed distance between electrodes. Both j_B/j_{MAX} and j_A/j_{MAX} have a maximum for semiaxis ~ 0.25. This result can be achieved thanks to the optimal balance between field enhancement and current localization. In figure 53c, simulation results for three different geometries are shown: in I. semiaxis is small (0.1, normalized), and field enhancement is the dominant mechanism that leads to current inhomogeneities near the electrodes boundaries. In II. the contributions of field enhancement and current localization are almost perfectly matched, as clearly visible from almost perfect uniformity in the current density near the electrode boundaries. In III., due to the almost round geometry, current confinement dominates.

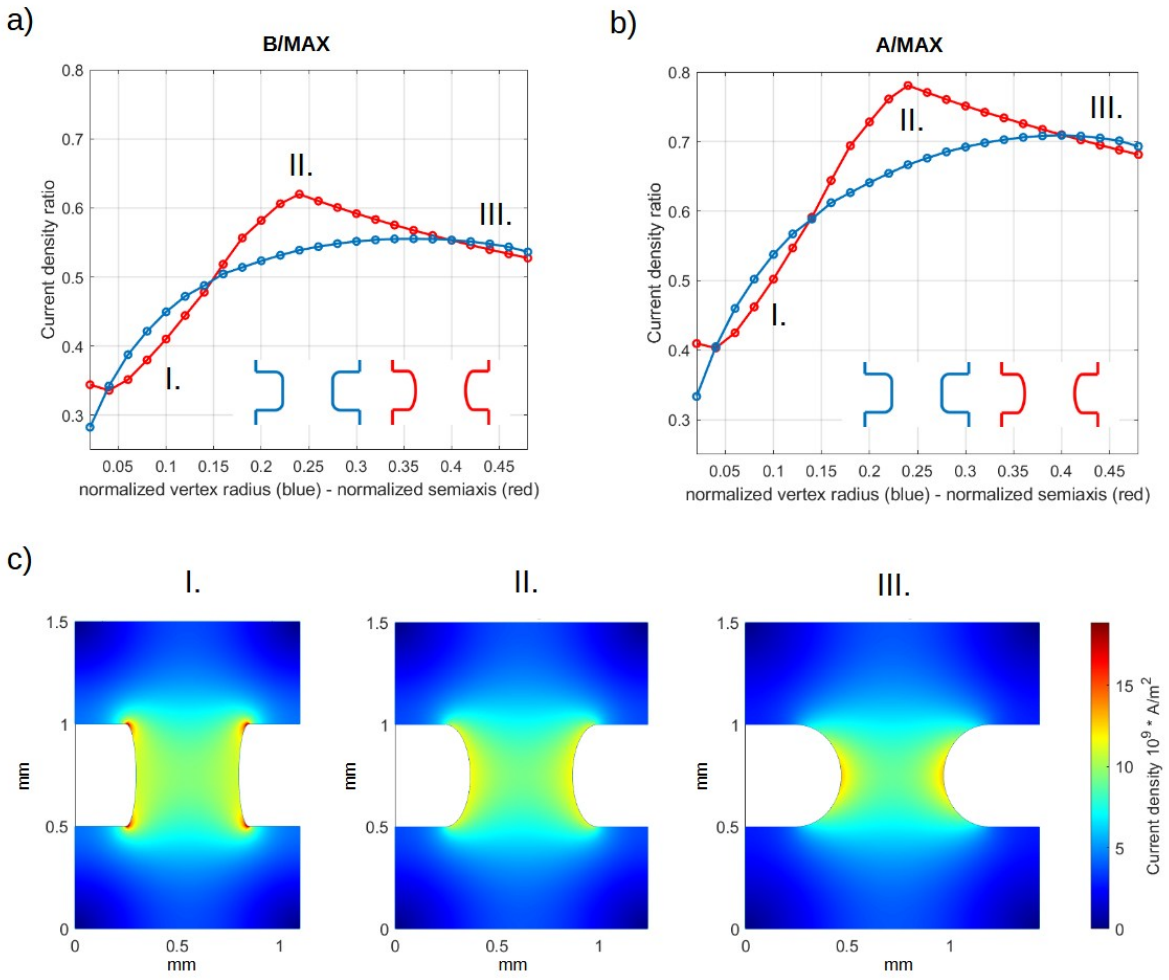

Figure 53: comparison between results found for the two simulated geometries, namely squared with round vertexes and semi-ellipse. The distance between the electrodes is fixed to 1, for easier visualization. a) ratio between current density in B and maximum current density. b) ratio between current density in A and maximum current density. c) current density modulus for three different geometries: I. semiaxis = 0.05 mm (0.1, normalized), II. semiaxis = 0.12 mm (0.24, normalized), III. semiaxis = 0.22 mm (0.44, normalized).

Now I summarize the main results that I have obtained in this section. I addressed the problem of electrodes geometry optimization for reliable forming process. Specifically, our goal is to avoid localized or strongly inhomogeneous structural modifications. I noticed that two main mechanisms can induce structural strong current density inhomogeneities, namely, field enhancement, due to the presence of sharp edges, and current confinement. I found both electrodes geometry and separation have an impact in determining current distribution in our system. In case of large electrodes separation (> electrode width), current confinement is reduced, and the most detrimental effect is field enhancement. In the optimized semi-elliptical geometry, field enhancement is subdominant for ellipse eccentricity roughly > 0.5.

Appendix 2: Solution of the inverse problem for a triangular resistor network

In this appendix I present the explicit solution for the groove conductance from the system (3.15). Using the same notation adopted in the main text, the conductance measured between different couples of electrodes is expressed in terms of the conductance of the grooves (unknown) as:

$$\begin{cases} C_{AB} = c_1 + \dfrac{c_2 c_3}{c_2 + c_3} = \dfrac{c_1 c_2 + c_2 c_3 + c_2 c_3}{c_2 + c_3} = \dfrac{S}{c_2 + c_3} \\ C_{BC} = c_2 + \dfrac{c_3 c_1}{c_3 + c_1} = \dfrac{c_1 c_2 + c_2 c_3 + c_2 c_3}{c_1 + c_3} = \dfrac{S}{c_1 + c_3} \\ C_{CA} = c_3 + \dfrac{c_1 c_2}{c_1 + c_2} = \dfrac{c_1 c_2 + c_2 c_3 + c_2 c_3}{c_1 + c_2} = \dfrac{S}{c_1 + c_2} \end{cases} \qquad (A2.1)$$

Where $S = c_1 c_2 + c_2 c_3 + c_1 c_3$, and for a physically realizable network must be $c_i > 0$, $i = 1, \dots, 3$.

Notice that:

$$\begin{gathered} C_{AB} C_{CA} + C_{AB} C_{BC} - C_{BC} C_{CA} = \\ = S^2 \left[\frac{1}{(c_2 + c_3)(c_1 + c_2)} + \frac{1}{(c_2 + c_3)(c_1 + c_3)} - \frac{1}{(c_1 + c_3)(c_1 + c_2)} \right] = \\ = \frac{S^2 [(c_1 + c_3) + (c_1 + c_2) - (c_2 + c_3)]}{(c_2 + c_3)(c_1 + c_2)(c_1 + c_3)} = \frac{2S^2}{\Delta} c_1 \end{gathered} \qquad (A2.2)$$

Where:

$$\Delta = (c_2 + c_3)(c_1 + c_2)(c_1 + c_3) \qquad (A2.3)$$

And we can proceed in analogous way for c_2 and c_3:

$$\begin{cases} C_{AB} C_{CA} + C_{AB} C_{BC} - C_{BC} C_{CA} = \dfrac{2S^2}{\Delta} c_1 \\ C_{AB} C_{BC} + C_{BC} C_{CA} - C_{AB} C_{CA} = \dfrac{2S^2}{\Delta} c_2 \\ C_{BC} C_{CA} + C_{AB} C_{CA} - C_{AB} C_{BC} = \dfrac{2S^2}{\Delta} c_3 \end{cases} \qquad (A2.4)$$

In order to isolate every c_i, we need to express the term $\frac{2S^2}{\Delta}$ in terms of C_{AB}, C_{BC}, C_{CA}.

Notice that:

$$\begin{gathered} 2S = c_1c_2 + c_2c_3 + c_1c_3 + c_1c_2 + c_2c_3 + c_1c_3 = \\ = 2[(c_1 + c_2)(c_2 + c_3) + (c_2 + c_3)(c_1 + c_3) + (c_1 + c_2)(c_1 + c_3)] + \\ -(c_1 + c_2)^2 - (c_2 + c_3)^2 - (c_1 + c_3)^2 = \\ = S^2\left[\frac{2}{C_{BC}C_{CA}} + \frac{2}{C_{AB}C_{BC}} + \frac{2}{C_{CA}C_{AB}} - \frac{1}{C_{CA}^2} - \frac{1}{C_{AB}^2} - \frac{1}{C_{BC}^2}\right] \end{gathered} \tag{A2.5}$$

Where we used the definition of C_{AB}, C_{BC}, C_{CA} in $(A2.1)$. Being $S > 0$, it follows that:

$$\begin{gathered} S = 2\left[\frac{2}{C_{BC}C_{CA}} + \frac{2}{C_{AB}C_{BC}} + \frac{2}{C_{CA}C_{AB}} - \frac{1}{C_{CA}^2} - \frac{1}{C_{AB}^2} - \frac{1}{C_{BC}^2}\right]^{-1} = \\ = 2(C_{AB}C_{BC}C_{CA})^2(2C_{AB}^2C_{BC}C_{CA} + 2C_{AB}C_{BC}^2C_{CA} + 2C_{AB}C_{BC}C_{CA}^2 \\ - C_{AB}^2C_{BC}^2 - C_{CA}^2C_{BC}^2 - C_{AB}^2C_{CA}^2)^{-1} \end{gathered} \tag{A2.6}$$

And:

$$\Delta = (c_1 + c_2)(c_2 + c_3)(c_1 + c_3) = \frac{S^3}{C_{CA}C_{AB}C_{BC}} \tag{A2.7}$$

So, defining:

$$\begin{gathered} D = \frac{2S^2}{\Delta} = 2\frac{C_{CA}C_{AB}C_{BC}}{S} = \\ = -\frac{C_{AB}^2C_{BC}^2 + C_{CA}^2C_{BC}^2 + C_{AB}^2C_{CA}^2 - 2C_{AB}^2C_{BC}C_{CA} - 2C_{AB}C_{BC}^2C_{CA} - 2C_{AB}C_{BC}C_{CA}^2}{C_{AB}C_{BC}C_{CA}} \end{gathered} \tag{A2.8}$$

From $(A2.4)$ we find the expressions for the grooves conductance:

$$\begin{cases} c_1 = (C_{AB}C_{CA} + C_{AB}C_{BC} - C_{BC}C_{CA})D \\ c_2 = (C_{AB}C_{BC} + C_{BC}C_{CA} - C_{AB}C_{CA})D \\ c_3 = (C_{BC}C_{CA} + C_{AB}C_{CA} - C_{AB}C_{BC})D \end{cases} \tag{A2.9}$$

That matches with the expression (3.16) in the main text.

References

[1] J. Abbate, «Getting small: a short history of the personal computer», *Proc. IEEE*, vol. 87, fasc. 9, pp. 1695–1698, set. 1999, doi: 10.1109/5.784256.

[2] S. Li, L. D. Xu, e S. Zhao, «The internet of things: a survey», *Inf Syst Front*, vol. 17, fasc. 2, pp. 243–259, apr. 2015, doi: 10.1007/s10796-014-9492-7.

[3] J. Sepúlveda, «FROM BIG DATA TO SMART DATA. OPPORTUNITIES FOR ENTREPRENEURS USING DATA SPACE ECOSYSTEM APPROACH», *JER*, vol. 1, fasc. 2, pp. 87–96, dic. 2023, doi: 10.29073/jer.v1i2.19.

[4] M. Butaboev, B. Qodirov, e X. Askarov, «Big Data as the oil of the digital economy», *BIO Web Conf.*, vol. 186, p. 02009, 2025, doi: 10.1051/bioconf/202518602009.

[5] K. Cao, Y. Liu, G. Meng, e Q. Sun, «An Overview on Edge Computing Research», *IEEE Access*, vol. 8, pp. 85714–85728, 2020, doi: 10.1109/ACCESS.2020.2991734.

[6] Subramanian Sendil Kumar, Sneha Singireddy, Botlagunta Preethish Nanan, Mahesh Recharla, Anil Lokesh Gadi, e Srinivasarao Paleti, «Optimizing Edge Computing for Big Data Processing in Smart Cities», *Metall Mater Eng*, vol. 31, fasc. 3, pp. 31–39, mar. 2025, doi: 10.63278/1317.

[7] C. Chakraborty, M. Bhattacharya, S. Pal, e S.-S. Lee, «From machine learning to deep learning: Advances of the recent data-driven paradigm shift in medicine and healthcare», *Current Research in Biotechnology*, vol. 7, p. 100164, 2024, doi: 10.1016/j.crbiot.2023.100164.

[8] A. De Vries, «The growing energy footprint of artificial intelligence», *Joule*, vol. 7, fasc. 10, pp. 2191–2194, ott. 2023, doi: 10.1016/j.joule.2023.09.004.

[9] J. Sun, J. Sun, X. Li, Y. Sun, Q. Hong, e C. Wang, «A Review of Recent Developments in Neuromorphic Computing Based on Emerging Memory Devices», *Nonlinear Dyn*, set. 2025, doi: 10.1007/s11071-025-11727-7.

[10] A. Vahl, G. Milano, Z. Kuncic, S. A. Brown, e P. Milani, «Brain-inspired computing with self-assembled networks of nano-objects», *Journal of Physics D: Applied Physics*, vol. 57, fasc. 50, p. 503001, dic. 2024, doi: 10.1088/1361-6463/ad7a82.

[11] G. Hamm, «2024 United States Data Center Energy Usage Report», Lawrence Berkely National Laboratory, 2025. doi: 10.71468/P1WC7Q.

[12] B. J. Copeland e Z. Fan, «Turing and Von Neumann: From Logic to the Computer», *Philosophies*, vol. 8, fasc. 2, p. 22, mar. 2023, doi: 10.3390/philosophies8020022.

[13] A. M. Turing, «On Computable Numbers, with an Application to the Entscheidungsproblem», *Proceedings of the London Mathematical Society*, vol. s2-42, fasc. 1, pp. 230–265, 1937, doi: 10.1112/plms/s2-42.1.230.

[14] J. E. Hopcroft, «Turing Machines», *Scientific American*, vol. 250, fasc. 5, pp. 86-E9, 1984.

[15] J. E. Savage, *Models of Computation: Exploring the Power of Computing*. Addison-Wesley., 1998.

[16] M. Wolf, *High-Performance Embedded Computing*. Elsevier, 2014. doi: 10.1016/C2012-0-07058-5.

[17] E. Roche e Y. Schabes, A c. di, *Finite-State Language Processing*. The MIT Press, 1997. doi: 10.7551/mitpress/3007.001.0001.

[18] A. Danchin e A. A. Fenton, «From Analog to Digital Computing: Is Homo sapiens' Brain on Its Way to Become a Turing Machine?», *Front. Ecol. Evol.*, vol. 10, p. 796413, mag. 2022, doi: 10.3389/fevo.2022.796413.

[19] G. O'Brien e J. Opie, «The role of representation in computation», *Cogn Process*, vol. 10, fasc. 1, pp. 53–62, feb. 2009, doi: 10.1007/s10339-008-0227-x.

[20] H. Jaeger, «Towards a generalized theory comprising digital, neuromorphic and unconventional computing», *Neuromorphic Computing and Engineering*, vol. 1, fasc. 1, p. 012002, lug. 2021, doi: 10.1088/2634-4386/abf151.

[21] H. Jaeger, B. Noheda, e W. G. Van Der Wiel, «Toward a formal theory for computing machines made out of whatever physics offers», *Nat Commun*, vol. 14, fasc. 1, p. 4911, ago. 2023, doi: 10.1038/s41467-023-40533-1.

[22] I. I. Arikpo, F. U. Ogban, e I. E. Eteng, «Von neumann architecture and modern computers», *Global Journal of Mathematical Sciences*, vol. 6, fasc. 2, pp. 97–103, 2007, doi: 10.4314/gjmas.v6i2.21415.

[23] W. Aspray, *John von Neumann and the origins of modern computing*, 2. print. in History of computing. Cambridge, Mass.: MIT Press, 1992.

[24] H. D. Huskey, «EDVAC», in *Encyclopedia of Computer Science*, GBR: John Wiley and Sons Ltd., 2003, pp. 626–628.

[25] J. L. Hennessy, *Computer architecture: a quantitative approach*, Sixth edition. Cambridge, MA: Morgan Kaufmann Publishers, 2019.

[26] R. Eigenmann e D. J. Lilja, «Von neumann computers», *Wiley Encyclopedia of Electrical and Electronics Engineering*, vol. 23, pp. 387–400, 1998.

[27] N. C. Thompson e S. Spanuth, «The decline of computers as a general purpose technology», *Commun. ACM*, vol. 64, fasc. 3, pp. 64–72, mar. 2021, doi: 10.1145/3430936.

[28] J. Bardeen e W. H. Brattain, «The Transistor, A Semi-Conductor Triode», *Phys. Rev.*, vol. 74, fasc. 2, pp. 230–231, lug. 1948, doi: 10.1103/PhysRev.74.230.

[29] A. Singh e S. Singh, «Evolution of CMOS technology», *International Journal of Engineering Research & Technology (IJERT)*, vol. 5, fasc. 02, 2016.

[30] K. R. Raghunathan, «History of Microcontrollers: First 50 Years», *IEEE Micro*, vol. 41, fasc. 6, pp. 97–104, nov. 2021, doi: 10.1109/MM.2021.3114754.

[31] J. Dongarra, «Trends in high - performance computing», *IEEE Circuits Devices Mag.*, vol. 22, fasc. 1, pp. 22–27, gen. 2006, doi: 10.1109/MCD.2006.1598076.

[32] B. Davari, «CMOS technology: Present and future», in *1999 Symposium on VLSI Circuits. Digest of Papers (IEEE Cat. No.99CH36326)*, Kyoto, Japan: Japan Soc. Appl. Phys, 1999, pp. 5–10. doi: 10.1109/VLSIC.1999.797216.

[33] M. T. Bohr e I. A. Young, «CMOS Scaling Trends and Beyond», *IEEE Micro*, vol. 37, fasc. 6, pp. 20–29, nov. 2017, doi: 10.1109/MM.2017.4241347.

[34] S. E. Thompson e S. Parthasarathy, «Moore's law: the future of Si microelectronics», *Materials Today*, vol. 9, fasc. 6, pp. 20–25, giu. 2006, doi: 10.1016/S1369-7021(06)71539-5.

[35] V. V. Zhirnov, R. K. Cavin, J. A. Hutchby, e G. I. Bourianoff, «Limits to binary logic switch scaling-a gedanken model», *Proc. IEEE*, vol. 9, fasc. 11, pp. 1934–1939, nov. 2003, doi: 10.1109/JPROC.2003.818324.

[36] R. H. Dennard, F. H. Gaensslen, H.-N. Yu, V. L. Rideout, E. Bassous, e A. R. LeBlanc, «Design of ion-implanted MOSFET's with very small physical dimensions», *IEEE J. Solid-State Circuits*, vol. 9, fasc. 5, pp. 256–268, ott. 1974, doi: 10.1109/JSSC.1974.1050511.

[37] O. Mosoiu, L. Gherman, e V. Bucinschi, «INFORMATION RESOURCES MANAGEMENT BASED ON FEEDBACK THEORY», presentato al eLSE 2016, Bucharest, RO, apr. 2016, pp. 115–121. doi: 10.12753/2066-026X-16-017.

[38] M. L. Rieger, «Retrospective on VLSI value scaling and lithography», *J. Micro/Nanolith. MEMS MOEMS*, vol. 18, fasc. 04, p. 1, nov. 2019, doi: 10.1117/1.JMM.18.4.040902.

[39] G. E. Moore, «Cramming more components onto integrated circuits, Reprinted from Electronics, volume 38, number 8, April 19, 1965, pp.114 ff.», *IEEE Solid-State Circuits Soc. Newsl.*, vol. 11, fasc. 3, pp. 33–35, set. 2006, doi: 10.1109/N-SSC.2006.4785860.

[40] Y. Deng, P. Liu, Z. Zhang, J. Jin, P. Xu, e L. Yan, «3D package thermal analysis and thermal optimization», *Case Studies in Thermal Engineering*, vol. 64, p. 105465, dic. 2024, doi: 10.1016/j.csite.2024.105465.

[41] D. Mamaluy e X. Gao, «The fundamental downscaling limit of field effect transistors», *Applied Physics Letters*, vol. 106, fasc. 19, p. 193503, mag. 2015, doi: 10.1063/1.4919871.

[42] R. S. Williams, «What's Next? [The end of Moore's law]», *Comput. Sci. Eng.*, vol. 19, fasc. 2, pp. 7–13, mar. 2017, doi: 10.1109/MCSE.2017.31.

[43] Y. Yuan, «3D packaging and Moore's Law», *J. Phys.: Conf. Ser.*, vol. 2798, fasc. 1, p. 012048, lug. 2024, doi: 10.1088/1742-6596/2798/1/012048.

[44] D. Brooks e M. Martonosi, «Dynamic thermal management for high-performance microprocessors», in *Proceedings HPCA Seventh International Symposium on High-Performance Computer Architecture*, Monterrey, Mexico: IEEE Comput. Soc, 2001, pp. 171–182. doi: 10.1109/HPCA.2001.903261.

[45] R. Landauer, «Irreversibility and Heat Generation in the Computing Process», *IBM J. Res. & Dev.*, vol. 5, fasc. 3, pp. 183–191, lug. 1961, doi: 10.1147/rd.53.0183.

[46] J. W. Elliott, M. T. Lebon, e A. J. Robinson, «Optimising integrated heat spreaders with distributed heat transfer coefficients: A case study for CPU cooling», *Case Studies in Thermal Engineering*, vol. 38, p. 102354, ott. 2022, doi: 10.1016/j.csite.2022.102354.

[47] X. Zou, S. Xu, X. Chen, L. Yan, e Y. Han, «Breaking the von Neumann bottleneck: architecture-level processing-in-memory technology», *Sci. China Inf. Sci.*, vol. 64, fasc. 6, p. 160404, giu. 2021, doi: 10.1007/s11432-020-3227-1.

[48] O. Mutlu, S. Ghose, J. Gómez-Luna, e R. Ausavarungnirun, «A Modern Primer on Processing in Memory», in *Emerging Computing: From Devices to Systems*, M. M. S. Aly e A. Chattopadhyay, A c. di, in Computer Architecture and Design Methodologies. , Singapore: Springer Nature Singapore, 2023, pp. 171–243. doi: 10.1007/978-981-16-7487-7_7.

[49] S. Mittal, «A Survey of ReRAM-Based Architectures for Processing-In-Memory and Neural Networks», *MAKE*, vol. 1, fasc. 1, pp. 75–114, apr. 2018, doi: 10.3390/make1010005.

[50] C. A. Mack, «Fifty Years of Moore's Law», *IEEE Trans. Semicond. Manufact.*, vol. 24, fasc. 2, pp. 202–207, mag. 2011, doi: 10.1109/TSM.2010.2096437.

[51] M. LaPedus, «What is the cost of fabs and R&D at 22-nm?», *EE Times*, febbraio 2009.

[52] A. Allan, D. Edenfeld, W. H. Joyner, A. B. Kahng, M. Rodgers, e Y. Zorian, «2001 technology roadmap for semiconductors», *Computer*, vol. 35, fasc. 1, pp. 42–53, gen. 2002, doi: 10.1109/2.976918.

[53] E. Masanet, A. Shehabi, N. Lei, S. Smith, e J. Koomey, «Recalibrating global data center energy-use estimates», *Science*, vol. 367, fasc. 6481, pp. 984–986, feb. 2020, doi: 10.1126/science.aba3758.

[54] I. Zhou *et al.*, «Internet of Things 2.0: Concepts, Applications, and Future Directions», *IEEE Access*, vol. 9, pp. 70961–71012, 2021, doi: 10.1109/ACCESS.2021.3078549.
[55] Y. Shi, «Big Data and Big Data Analytics», in *Advances in Big Data Analytics*, Singapore: Springer Nature Singapore, 2022, pp. 3–21. doi: 10.1007/978-981-16-3607-3_1.
[56] S. Sagiroglu e D. Sinanc, «Big data: A review», in *2013 International Conference on Collaboration Technologies and Systems (CTS)*, San Diego, CA, USA: IEEE, mag. 2013, pp. 42–47. doi: 10.1109/CTS.2013.6567202.
[57] C. Mead, «Neuromorphic electronic systems», *Proc. IEEE*, vol. 78, fasc. 10, pp. 1629–1636, ott. 1990, doi: 10.1109/5.58356.
[58] H. Zeng e J. R. Sanes, «Neuronal cell-type classification: challenges, opportunities and the path forward», *Nat Rev Neurosci*, vol. 18, fasc. 9, pp. 530–546, set. 2017, doi: 10.1038/nrn.2017.85.
[59] R. Carpenter e B. Reddi, *Neurophysiology*, 0 ed. CRC Press, 2012. doi: 10.1201/b13510.
[60] T. C. Südhof, «Towards an Understanding of Synapse Formation», *Neuron*, vol. 100, fasc. 2, pp. 276–293, ott. 2018, doi: 10.1016/j.neuron.2018.09.040.
[61] A. M. Craig e G. Banker, «Neuronal Polarity», *Annu. Rev. Neurosci.*, vol. 17, fasc. 1, pp. 267–310, mar. 1994, doi: 10.1146/annurev.ne.17.030194.001411.
[62] S. Tahirovic e F. Bradke, «Neuronal Polarity», *Cold Spring Harbor Perspectives in Biology*, vol. 1, fasc. 3, pp. a001644–a001644, set. 2009, doi: 10.1101/cshperspect.a001644.
[63] R. R. Borges *et al.*, «Synaptic Plasticity and Spike Synchronisation in Neuronal Networks», *Braz J Phys*, vol. 47, fasc. 6, pp. 678–688, dic. 2017, doi: 10.1007/s13538-017-0529-5.
[64] M. W. Reimann, J. G. King, E. B. Muller, S. Ramaswamy, e H. Markram, «An algorithm to predict the connectome of neural microcircuits», *Front. Comput. Neurosci.*, vol. 9, ott. 2015, doi: 10.3389/fncom.2015.00120.
[65] M. W. Barnett e P. M. Larkman, «The action potential», *Pract Neurol*, vol. 7, fasc. 3, p. 192, giu. 2007.
[66] F. Borghi, T. R. Nieus, D. E. Galli, e P. Milani, «Brain-like hardware, do we need it?», *Front. Neurosci.*, vol. 18, p. 1465789, dic. 2024, doi: 10.3389/fnins.2024.1465789.
[67] D. Livingstone, A c. di, *Artificial neural networks: methods and applications*. in Methods in molecular biology, no. 458. Totowa, NJ: Humana Press, 2008.
[68] O. I. Abiodun, A. Jantan, A. E. Omolara, K. V. Dada, N. A. Mohamed, e H. Arshad, «State-of-the-art in artificial neural network applications: A survey», *Heliyon*, vol. 4, fasc. 11, p. e00938, nov. 2018, doi: 10.1016/j.heliyon.2018.e00938.
[69] W. S. McCulloch e W. Pitts, «A logical calculus of the ideas immanent in nervous activity», *Bulletin of Mathematical Biophysics*, vol. 5, fasc. 4, pp. 115–133, dic. 1943, doi: 10.1007/BF02478259.
[70] A. J. Al-Mahasneh, S. G. Anavatti, e M. A. Garratt, «The development of neural networks applications from perceptron to deep learning», in *2017 International Conference on Advanced Mechatronics, Intelligent Manufacture, and Industrial Automation (ICAMIMIA)*, Surabaya: IEEE, ott. 2017, pp. 1–6. doi: 10.1109/ICAMIMIA.2017.8387619.
[71] F. Rosenblatt, «The perceptron: A probabilistic model for information storage and organization in the brain.», *Psychological Review*, vol. 65, fasc. 6, pp. 386–408, 1958, doi: 10.1037/h0042519.

[72] M. Minsky e S. A. Papert, *Perceptrons: An Introduction to Computational Geometry*. The MIT Press, 2017. doi: 10.7551/mitpress/11301.001.0001.
[73] D. E. Rumelhart, G. E. Hinton, e R. J. Williams, «Learning representations by back-propagating errors», *Nature*, vol. 323, fasc. 6088, pp. 533–536, ott. 1986, doi: 10.1038/323533a0.
[74] J. Wu, Y. Wang, Z. Li, L. Lu, e Q. Li, «A Review of Computing with Spiking Neural Networks», *CMC*, vol. 78, fasc. 3, pp. 2909–2939, 2024, doi: 10.32604/cmc.2024.047240.
[75] K. Yamazaki, V.-K. Vo-Ho, D. Bulsara, e N. Le, «Spiking Neural Networks and Their Applications: A Review», *Brain Sciences*, vol. 12, fasc. 7, p. 863, giu. 2022, doi: 10.3390/brainsci12070863.
[76] T. Baji, «Evolution of the GPU Device widely used in AI and Massive Parallel Processing», in *2018 IEEE 2nd Electron Devices Technology and Manufacturing Conference (EDTM)*, Kobe: IEEE, mar. 2018, pp. 7–9. doi: 10.1109/EDTM.2018.8421507.
[77] B. Chopra, «ENHANCING MACHINE LEARNING PERFORMANCE: THE ROLE OF GPU-BASED AI COMPUTE ARCHITECTURES», *J. Knowl. Learn. Sci. Technol.*, vol. 3, fasc. 3, pp. 20–32, lug. 2024, doi: 10.60087/jklst.vol3.n3.p20-32.
[78] V. S. Sharma, S. Mahajan, A. Nayyar, e A. Kant Pandit, *Deep Learning in Engineering, Energy and Finance: Principals and Applications*, 1ª ed. Boca Raton: CRC Press, 2024. doi: 10.1201/9781003564874.
[79] D. Ielmini e G. Pedretti, «Device and Circuit Architectures for In-Memory Computing», *Advanced Intelligent Systems*, vol. 2, fasc. 7, p. 2000040, lug. 2020, doi: 10.1002/aisy.202000040.
[80] DeepSeek-AI *et al.*, «DeepSeek-V3 Technical Report», 2024, *arXiv*. doi: 10.48550/ARXIV.2412.19437.
[81] B. Cottier, R. Rahman, L. Fattorini, N. Maslej, T. Besiroglu, e D. Owen, «The rising costs of training frontier AI models», 2024, *arXiv*. doi: 10.48550/ARXIV.2405.21015.
[82] E. K. Oermann e D. Kondziolka, «On Chatbots and Generative Artificial Intelligence», *Neurosurgery*, vol. 92, fasc. 4, pp. 665–666, apr. 2023, doi: 10.1227/neu.0000000000002415.
[83] R. Verdecchia, J. Sallou, e L. Cruz, «A systematic review of Green AI», *WIREs Data Min & Knowl*, vol. 13, fasc. 4, p. e1507, lug. 2023, doi: 10.1002/widm.1507.
[84] C. E. Tripp *et al.*, «Measuring the Energy Consumption and Efficiency of Deep Neural Networks: An Empirical Analysis and Design Recommendations», 2024, *arXiv*. doi: 10.48550/ARXIV.2403.08151.
[85] Nestor Masle, «Artificial Intelligence Index Report 2025». ” AI Index Steering Committee, Institute for Human-Centered AI, Stanford University, Stanford, CA, aprile 2025.
[86] I. Boybat *et al.*, «Neuromorphic computing with multi-memristive synapses», *Nat Commun*, vol. 9, fasc. 1, p. 2514, giu. 2018, doi: 10.1038/s41467-018-04933-y.
[87] B. A. Richards e T. P. Lillicrap, «The Brain-Computer Metaphor Debate Is Useless: A Matter of Semantics», *Front. Comput. Sci.*, vol. 4, p. 810358, feb. 2022, doi: 10.3389/fcomp.2022.810358.
[88] G. Indiveri *et al.*, «Neuromorphic Silicon Neuron Circuits», *Front. Neurosci*, vol. 5, 2011, doi: 10.3389/fnins.2011.00073.
[89] D. Decastri e F. Borghi, «Advances in Neuromorphic Computing Devices: Insights on Both Conventional and Unconventional Architectures», *NANOTEC*, vol. 19, feb. 2025, doi: 10.2174/0118722105335459241210043513.

[90] P. Mannocci *et al.*, «In-memory computing with emerging memory devices: Status and outlook», *APL Machine Learning*, vol. 1, fasc. 1, p. 010902, mar. 2023, doi: 10.1063/5.0136403.
[91] Y. Xiao *et al.*, «A review of memristor: material and structure design, device performance, applications and prospects», *Science and Technology of Advanced Materials*, vol. 24, fasc. 1, p. 2162323, dic. 2023, doi: 10.1080/14686996.2022.2162323.
[92] F. Yang, J. Ma, e F. Wu, «Review on memristor application in neural circuit and network», *Chaos, Solitons & Fractals*, vol. 187, p. 115361, ott. 2024, doi: 10.1016/j.chaos.2024.115361.
[93] L. Chua, «Memristor-The missing circuit element», *IEEE Trans. Circuit Theory*, vol. 18, fasc. 5, pp. 507–519, 1971, doi: 10.1109/TCT.1971.1083337.
[94] L. O. Chua e G. C. Sirakoulis, *Handbook of memristor networks*. Cham: Springer, 2019.
[95] F. Zahoor, T. Z. Azni Zulkifli, e F. A. Khanday, «Resistive Random Access Memory (RRAM): an Overview of Materials, Switching Mechanism, Performance, Multilevel Cell (mlc) Storage, Modeling, and Applications», *Nanoscale Res Lett*, vol. 15, fasc. 1, p. 90, dic. 2020, doi: 10.1186/s11671-020-03299-9.
[96] Q. Xia e J. J. Yang, «Memristive crossbar arrays for brain-inspired computing», *Nat. Mater.*, vol. 18, fasc. 4, pp. 309–323, apr. 2019, doi: 10.1038/s41563-019-0291-x.
[97] H. Li *et al.*, «Memristive Crossbar Arrays for Storage and Computing Applications», *Advanced Intelligent Systems*, vol. 3, fasc. 9, p. 2100017, set. 2021, doi: 10.1002/aisy.202100017.
[98] Q. Xia e J. J. Yang, «Memristive crossbar arrays for brain-inspired computing», *Nat. Mater.*, vol. 18, fasc. 4, pp. 309–323, apr. 2019, doi: 10.1038/s41563-019-0291-x.
[99] Z. Liu *et al.*, «Neural signal analysis with memristor arrays towards high-efficiency brain–machine interfaces», *Nat Commun*, vol. 11, fasc. 1, p. 4234, ago. 2020, doi: 10.1038/s41467-020-18105-4.
[100] S.-Y. Min e W.-J. Cho, «High-Performance Resistive Switching in Solution-Derived IGZO:N Memristors by Microwave-Assisted Nitridation», *Nanomaterials*, vol. 11, fasc. 5, p. 1081, apr. 2021, doi: 10.3390/nano11051081.
[101] O. Sporns, G. Tononi, e R. Kötter, «The Human Connectome: A Structural Description of the Human Brain», *PLoS Comp Biol*, vol. 1, fasc. 4, p. e42, 2005, doi: 10.1371/journal.pcbi.0010042.
[102] D. Clark, «Teramac: pointing the way to real-world nanotechnology», *IEEE Comput. Sci. Eng.*, vol. 5, fasc. 3, pp. 88–90, set. 1998, doi: 10.1109/99.714606.
[103] K.-P. Zauner, «From Prescriptive Programming of Solid-State Devices to Orchestrated Self-organisation of Informed Matter», in *Unconventional Programming Paradigms*, vol. 3566, J.-P. Banâtre, P. Fradet, J.-L. Giavitto, e O. Michel, A c. di, in Lecture Notes in Computer Science, vol. 3566. , Berlin, Heidelberg: Springer Berlin Heidelberg, 2005, pp. 47–55. doi: 10.1007/11527800_4.
[104] M. D. Pike *et al.*, «Atomic Scale Dynamics Drive Brain-like Avalanches in Percolating Nanostructured Networks», *Nano Letters*, vol. 20, fasc. 5, pp. 3935–3942, mag. 2020, doi: 10.1021/acs.nanolett.0c01096.
[105] J. B. Mallinson, S. Shirai, S. K. Acharya, S. K. Bose, E. Galli, e S. A. Brown, «Avalanches and criticality in self-organized nanoscale networks», *Science Advances*, vol. 5, fasc. 11, p. eaaw8438, nov. 2019, doi: 10.1126/sciadv.aaw8438.

[106] C. Minnai, A. Bellacicca, S. A. Brown, e P. Milani, «Facile fabrication of complex networks of memristive devices», *Sci Rep*, vol. 7, fasc. 1, ago. 2017, doi: 10.1038/s41598-017-08244-y.
[107] C. Minnai, «The nanocoherer: an electrically and mechanically resettable resistive switching device based on gold clusters assembled on paper», *Nano Futures*, 2018.
[108] M. Mirigliano *et al.*, «Complex electrical spiking activity in resistive switching nanostructured Au two-terminal devices», *Nanotechnology*, vol. 31, fasc. 23, p. 234001, mar. 2020, doi: 10.1088/1361-6528/ab76ec.
[109] A. Diaz-Alvarez *et al.*, «Emergent dynamics of neuromorphic nanowire networks», *Sci Rep*, vol. 9, fasc. 1, p. 14920, ott. 2019, doi: 10.1038/s41598-019-51330-6.
[110] Z. Kuncic e T. Nakayama, «Neuromorphic nanowire networks: principles, progress and future prospects for neuro-inspired information processing», *Advances in Physics: X*, vol. 6, fasc. 1, p. 1894234, gen. 2021, doi: 10.1080/23746149.2021.1894234.
[111] G. Milano *et al.*, «Brain-Inspired Structural Plasticity through Reweighting and Rewiring in Multi-Terminal Self-Organizing Memristive Nanowire Networks», *Advanced Intelligent Systems*, vol. 2, fasc. 8, p. 2000096, ago. 2020, doi: 10.1002/aisy.202000096.
[112] G. Tanaka *et al.*, «Recent advances in physical reservoir computing: A review», *Neural Networks*, vol. 115, pp. 100–123, lug. 2019, doi: 10.1016/j.neunet.2019.03.005.
[113] H. Jaeger e H. Haas, «Harnessing Nonlinearity: Predicting Chaotic Systems and Saving Energy in Wireless Communication», *Science*, vol. 304, fasc. 5667, pp. 78–80, apr. 2004, doi: 10.1126/science.1091277.
[114] M. Lukoševičius e H. Jaeger, «Reservoir computing approaches to recurrent neural network training», *Computer Science Review*, vol. 3, fasc. 3, pp. 127–149, ago. 2009, doi: 10.1016/j.cosrev.2009.03.005.
[115] G. Milano *et al.*, «In materia reservoir computing with a fully memristive architecture based on self-organizing nanowire networks», *Nat. Mater.*, vol. 21, fasc. 2, pp. 195–202, feb. 2022, doi: 10.1038/s41563-021-01099-9.
[116] G. Milano, K. Montano, e C. Ricciardi, «In materia implementation strategies of physical reservoir computing with memristive nanonetworks», *J. Phys. D: Appl. Phys.*, vol. 56, fasc. 8, p. 084005, feb. 2023, doi: 10.1088/1361-6463/acb7ff.
[117] G. Milano, M. Agliuzza, N. De Leo, e C. Ricciardi, «Speech recognition through physical reservoir computing with neuromorphic nanowire networks», in *2022 International Joint Conference on Neural Networks (IJCNN)*, Padua, Italy: IEEE, lug. 2022, pp. 1–6. doi: 10.1109/IJCNN55064.2022.9892078.
[118] S. J. Studholme e S. A. Brown, «Integer Factorization with Stochastic Spiking in Percolating Networks of Nanoparticles», *ACS Nano*, vol. 18, fasc. 41, pp. 28060–28069, ott. 2024, doi: 10.1021/acsnano.4c07200.
[119] S. K. Acharya *et al.*, «Stochastic Spiking Behavior in Neuromorphic Networks Enables True Random Number Generation», *ACS Appl. Mater. Interfaces*, vol. 13, fasc. 44, pp. 52861–52870, nov. 2021, doi: 10.1021/acsami.1c13668.
[120] M. Mirigliano *et al.*, «A binary classifier based on a reconfigurable dense network of metallic nanojunctions», *Neuromorphic Computing and Engineering*, vol. 1, fasc. 2, p. 024007, dic. 2021, doi: 10.1088/2634-4386/ac29c9.
[121] G. Martini, M. Mirigliano, B. Paroli, e P. Milani, «The Receptron: a device for the implementation of information processing systems based on complex nanostructured systems», *Japanese Journal of Applied Physics*, vol. 61, fasc. SM, p. SM0801, giu. 2022, doi: 10.35848/1347-4065/ac665c.

[122] F. Profumo, F. Borghi, T. Angì, M. Maschietto, S. Vassanelli, e P. Milani, «Highly Efficient Classification of Time-Series Based on Resistive Switching Cluster-Assembled Materials», *Advanced Intelligent Systems*, 2025, doi: 10.1002/aisy.202401150.

[123] M. Mirigliano, S. Radice, A. Falqui, A. Casu, F. Cavaliere, e P. Milani, «Anomalous electrical conduction and negative temperature coefficient of resistance in nanostructured gold resistive switching films», *Scientific Reports*, vol. 10, fasc. 1, p. 19613, nov. 2020, doi: 10.1038/s41598-020-76632-y.

[124] G. Martini, «Reprogrammable threshold logic gates based on random nanostructured networks for algebraic and logic Boolean computation», PhD Thesis, Università degli Studi di Milano.

[125] B. Paroli, G. Martini, M. A. C. Potenza, M. Siano, M. Mirigliano, e P. Milani, «Solving classification tasks by a receptron based on nonlinear optical speckle fields», *Neural Networks*, vol. 166, pp. 634–644, set. 2023, doi: 10.1016/j.neunet.2023.08.001.

[126] B. Paroli, F. Borghi, M. A. C. Potenza, e P. Milani, «The receptron is a nonlinear threshold logic gate with intrinsic multi-dimensional selective capabilities for analog inputs», 2025, *arXiv*. doi: 10.48550/ARXIV.2506.19642.

[127] Davide Decastri *et al.*, «Programmable Functional Connectivity and Synchronous Activity in Resistive Switching Self-Assembled Nanostructured Networks», *Small Structures*, set. 2025, doi: https://doi.org/10.1002/sstr.202500330.

[128] E. Barborini, P. Piseri, e P. Milani, «A pulsed microplasma source of high intensity supersonic carbon cluster beams», *Journal of Physics D: Applied Physics*, vol. 32, fasc. 21, p. L105, nov. 1999, doi: 10.1088/0022-3727/32/21/102.

[129] P. Milani, P. G. C. Piseri, e E. Barborini, «Apparatus for production of nanosized particulate matter by vaporization of solid materials», US6392188B1, maggio 2002 Consultato: 31 maggio 2024. [Online]. Disponibile su: https://patents.google.com/patent/US6392188B1/en?oq=US6392188B1

[130] H. V. Tafreshi, P. Piseri, G. Benedek, e P. Milani, «The Role of Gas Dynamics in Operation Conditions of a Pulsed Microplasma Cluster Source for Nanostructured Thin Films Deposition», *J. Nanosci. Nanotech.*, vol. 6, fasc. 4, pp. 1140–1149, apr. 2006, doi: 10.1166/jnn.2006.139.

[131] K. Wegner, P. Piseri, H. V. Tafreshi, e P. Milani, «Cluster beam deposition: a tool for nanoscale science and technology», *Journal of Physics D: Applied Physics*, vol. 39, fasc. 22, pp. R439–R459, nov. 2006, doi: 10.1088/0022-3727/39/22/R02.

[132] P. Milani e S. Iannotta, *Cluster Beam Synthesis of Nanostructured Materials*. in Springer Series in Cluster Physics. Berlin, Heidelberg: Springer Berlin Heidelberg, 1999. doi: 10.1007/978-3-642-59899-9.

[133] H. V. Tafreshi, G. Benedek, P. Piseri, S. Vinati, E. Barborini, e P. Milani, «Aerodynamic focusing of clusters into a high intensity and low divergence supersonic beam», *The European Physical Journal Applied Physics*, vol. 16, fasc. 2, pp. 149–156, nov. 2001, doi: 10.1051/epjap:2001204.

[134] P. Piseri, H. V. Tafreshi, e P. Milani, «Manipulation of nanoparticles in supersonic beams for the production of nanostructured materials», *Current Opinion in Solid State and Materials Science*, vol. 8, fasc. 3–4, pp. 195–202, giu. 2004, doi: 10.1016/j.cossms.2004.08.002.

[135] P. Liu, P. J. Ziemann, D. B. Kittelson, e P. H. McMurry, «Generating Particle Beams of Controlled Dimensions and Divergence: I. Theory of Particle Motion in Aerodynamic

Lenses and Nozzle Expansions», *Aerosol Science and Technology*, vol. 22, fasc. 3, pp. 293–313, gen. 1995, doi: 10.1080/02786829408959748.

[136] P. Liu, P. J. Ziemann, D. B. Kittelson, e P. H. McMurry, «Generating Particle Beams of Controlled Dimensions and Divergence: II. Experimental Evaluation of Particle Motion in Aerodynamic Lenses and Nozzle Expansions», *Aerosol Science and Technology*, vol. 22, fasc. 3, pp. 314–324, gen. 1995, doi: 10.1080/02786829408959749.

[137] F. Di Fonzo *et al.*, «Focused nanoparticle-beam deposition of patterned microstructures», *Applied Physics Letters*, vol. 77, fasc. 6, pp. 910–912, ago. 2000, doi: 10.1063/1.1306638.

[138] G. Nadalini, F. Borghi, T. Košutová, A. Falqui, N. Ludwig, e P. Milani, «Engineering the structural and electrical interplay of nanostructured Au resistive switching networks by controlling the forming process», *Sci Rep*, vol. 13, fasc. 1, p. 19713, nov. 2023, doi: 10.1038/s41598-023-46990-4.

[139] G. Nadalini, A. Dallinger, D. Sottocorno, F. Greco, F. Borghi, e P. Milani, «Soft Electronic Switches and Adaptive Logic Gates Based on Nanostructured Gold Networks», *Adv Elect Materials*, vol. 11, fasc. 7, p. 2400717, mag. 2025, doi: 10.1002/aelm.202400717.

[140] C. Ghisleri *et al.*, «Patterning of gold–polydimethylsiloxane (Au–PDMS) nanocomposites by supersonic cluster beam implantation», *Journal of Physics D: Applied Physics*, vol. 47, fasc. 1, p. 015301, dic. 2013, doi: 10.1088/0022-3727/47/1/015301.

[141] N. Bouras, M. A. Madjoubi, M. Kolli, S. Benterki, e M. Hamidouche, «Thermal and mechanical characterization of borosilicate glass», *Physics Procedia*, vol. 2, fasc. 3, pp. 1135–1140, nov. 2009, doi: 10.1016/j.phpro.2009.11.074.

[142] M. López-Suárez, C. Melis, L. Colombo, e W. Tarantino, «Multiscale modeling of resistive switching in gold nanogranular films», 17 ottobre 2022, *arXiv*: arXiv:2210.09379. Consultato: 28 febbraio 2024. [Online]. Disponibile su: http://arxiv.org/abs/2210.09379

[143] T. N. Narasimhan, «Fourier's heat conduction equation: History, influence, and connections», *Proc. Indian Acad. Sci. (Earth Planet Sci.)*, vol. 108, fasc. 3, pp. 117–148, set. 1999, doi: 10.1007/bf02842327.

[144] F. Borghi, M. Mirigliano, D. Dellasega, e P. Milani, «Influence of the nanostructure on the electric transport properties of resistive switching cluster-assembled gold films», *Applied Surface Science*, vol. 582, p. 152485, apr. 2022, doi: 10.1016/j.apsusc.2022.152485.

[145] M. Mirigliano, F. Borghi, A. Podestà, A. Antidormi, L. Colombo, e P. Milani, «Non-ohmic behavior and resistive switching of Au cluster-assembled films beyond the percolation threshold», *Nanoscale Advances*, vol. 1, fasc. 8, pp. 3119–3130, 2019, doi: 10.1039/C9NA00256A.

[146] G. Dhatt, G. Touzot, e E. Lefrançois, *Finite Element Method*, 1ª ed. Wiley, 2012. doi: 10.1002/9781118569764.

[147] P. Piseri, A. Podestà, E. Barborini, e P. Milani, «Production and characterization of highly intense and collimated cluster beams by inertial focusing in supersonic expansions», *Review of Scientific Instruments*, vol. 72, fasc. 5, pp. 2261–2267, mag. 2001, doi: 10.1063/1.1361082.

[148] «Introduction to Microfabrication Techniques», in *Microfluidic Techniques*, New Jersey: Humana Press, pp. 3–16. doi: 10.1385/1-59259-997-4:3.

[149] «Lithography Technology for Micro- and Nanofabrication», in *Advances in Experimental Medicine and Biology*, Singapore: Springer Singapore, 2021, pp. 217–233. doi: 10.1007/978-981-33-6158-4_9.

[150] L. Levine, «Wire bonding - Documento - Gale Business: Insights». Consultato: 23 luglio 2025. [Online]. Disponibile su: https://go.gale.com/ps/i.do?p=GBIB&u=milano&id=GALE%7CA441586319&v=2.1&it=r

[151] Z. W. Zhong, «Overview of wire bonding using copper wire or insulated wire», *Microelectronics Reliability*, vol. 51, fasc. 1, pp. 4–12, gen. 2011, doi: 10.1016/j.microrel.2010.06.003.

[152] G. Harman e J. Albers, «The Ultrasonic Welding Mechanism as Applied to Aluminum- and Gold-Wire Bonding in Microelectronics», *IEEE Trans. Parts, Hybrids, Packag.*, vol. 13, fasc. 4, pp. 406–412, dic. 1977, doi: 10.1109/tphp.1977.1135225.

[153] S. Kirkpatrick, «Percolation and Conduction», *Rev. Mod. Phys.*, vol. 45, fasc. 4, pp. 574–588, ott. 1973, doi: 10.1103/revmodphys.45.574.

[154] D. Stauffer e A. Aharony, *Introduction To Percolation Theory*, 0 ed. Taylor & Francis, 2018. doi: 10.1201/9781315274386.

[155] F. Borghi, M. Milani, L. G. Bettini, A. Podestà, e P. Milani, «Quantitative characterization of the interfacial morphology and bulk porosity of nanoporous cluster-assembled carbon thin films», *Applied Surface Science*, vol. 479, pp. 395–402, 2019.

[156] F. Borghi, A. Podestà, C. Piazzoni, e P. Milani, «Growth Mechanism of Cluster-Assembled Surfaces: From Submonolayer to Thin-Film Regime», *Physical Review Applied*, vol. 9, fasc. 4, p. 044016, apr. 2018, doi: 10.1103/PhysRevApplied.9.044016.

[157] F. Bisio *et al.*, «Optical properties of cluster-assembled nanoporous gold films», *Phys. Rev. B*, vol. 80, fasc. 20, nov. 2009, doi: 10.1103/physrevb.80.205428.

[158] E. Barborini *et al.*, «The influence of nanoscale morphology on the resistivity of cluster-assembled nanostructured metallic thin films», *New J. Phys.*, vol. 12, fasc. 7, p. 073001, lug. 2010, doi: 10.1088/1367-2630/12/7/073001.

[159] M. Mirigliano e P. Milani, «Electrical conduction in nanogranular cluster-assembled metallic films», *Advances in Physics: X*, vol. 6, fasc. 1, p. 1908847, gen. 2021, doi: 10.1080/23746149.2021.1908847.

[160] G. Benetti *et al.*, «Bottom-Up Mechanical Nanometrology of Granular Ag Nanoparticles Thin Films», *J. Phys. Chem. C*, vol. 121, fasc. 40, pp. 22434–22441, ott. 2017, doi: 10.1021/acs.jpcc.7b05795.

[161] E. H. Sondheimer, «The mean free path of electrons in metals», *Advances in Physics*, vol. 1, fasc. 1, pp. 1–42, gen. 1952, doi: 10.1080/00018735200101151.

[162] C. Basaran, *Introduction to Unified Mechanics Theory with Applications*. Cham: Springer International Publishing, 2022. doi: 10.1007/978-3-031-18621-9.

[163] C. Durkan e M. E. Welland, «Analysis of failure mechanisms in electrically stressed gold nanowires», *Ultramicroscopy*, vol. 82, fasc. 1–4, pp. 125–133, feb. 2000, doi: 10.1016/s0304-3991(99)00133-3.

[164] A. Mukherjee, K. Ankit, M. Selzer, e B. Nestler, «Electromigration-Induced Surface Drift and Slit Propagation in Polycrystalline Interconnects: Insights from Phase-Field Simulations», *Phys. Rev. Applied*, vol. 9, fasc. 4, apr. 2018, doi: 10.1103/physrevapplied.9.044004.

[165] A. Podestà *et al.*, «Cluster-Assembled Nanostructured Titanium Oxide Films with Tailored Wettability», *J. Phys. Chem. C*, vol. 113, fasc. 42, pp. 18264–18269, ott. 2009, doi: 10.1021/jp905930r.

[166] A. Casu, A. Chiodoni, Y. P. Ivanov, G. Divitini, P. Milani, e A. Falqui, «*In Situ* TEM Investigation of Thermally Induced Modifications of Cluster-Assembled Gold Films Undergoing Resistive Switching: Implications for Nanostructured Neuromorphic Devices»,

ACS Appl. Nano Mater., vol. 7, fasc. 7, pp. 7203–7212, apr. 2024, doi: 10.1021/acsanm.3c06261.

[167] D. Cipollini, F. Profumo, L. Schomaker, P. Milani, e F. Borghi, «Conduction mechanisms in a planar nanocomposite resistive switching device based on cluster-assembled Au/ZrOx films», *Front. Mater.*, vol. 11, p. 1385792, giu. 2024, doi: 10.3389/fmats.2024.1385792.

[168] S. A. Brown, S. FOSTNER, e S. K. BOSE, «Neuromorphic network», WO2017003303A1, gennaio 2017 Consultato: 30 maggio 2024. [Online]. Disponibile su: https://patents.google.com/patent/WO2017003303A1/en?oq=WO2017003303A1

[169] A. V. Avizienis *et al.*, «Neuromorphic Atomic Switch Networks», *PLoS ONE*, vol. 7, fasc. 8, p. e42772, ago. 2012, doi: 10.1371/journal.pone.0042772.

[170] H. G. Manning *et al.*, «Emergence of winner-takes-all connectivity paths in random nanowire networks», *Nat Commun*, vol. 9, fasc. 1, p. 3219, ago. 2018, doi: 10.1038/s41467-018-05517-6.

[171] F. Niekiel, P. Schweizer, S. M. Kraschewski, B. Butz, e E. Spiecker, «The process of solid-state dewetting of Au thin films studied by in situ scanning transmission electron microscopy», *Acta Materialia*, vol. 90, pp. 118–132, mag. 2015, doi: 10.1016/j.actamat.2015.01.072.

[172] M. Karsai, K. Kaski, A.-L. Barabási, e J. Kertész, «Universal features of correlated bursty behaviour», *Scientific Reports*, vol. 2, fasc. 1, p. 397, mag. 2012, doi: 10.1038/srep00397.

[173] A. Z. Stieg, A. V. Avizienis, H. O. Sillin, C. Martin-Olmos, M. Aono, e J. K. Gimzewski, «Emergent Criticality in Complex Turing B-Type Atomic Switch Networks», *Advanced Materials*, vol. 24, fasc. 2, pp. 286–293, gen. 2012, doi: 10.1002/adma.201103053.

[174] A. Mazzoni, F. D. Broccard, E. Garcia-Perez, P. Bonifazi, M. E. Ruaro, e V. Torre, «On the Dynamics of the Spontaneous Activity in Neuronal Networks», *PLoS ONE*, vol. 2, fasc. 5, p. e439, mag. 2007, doi: 10.1371/journal.pone.0000439.

[175] L. De Arcangelis e H. J. Herrmann, «Learning as a phenomenon occurring in a critical state», *Proc. Natl. Acad. Sci. U.S.A.*, vol. 107, fasc. 9, pp. 3977–3981, mar. 2010, doi: 10.1073/pnas.0912289107.

[176] L. Cocchi, L. L. Gollo, A. Zalesky, e M. Breakspear, «Criticality in the brain: A synthesis of neurobiology, models and cognition», *Progress in Neurobiology*, vol. 158, pp. 132–152, nov. 2017, doi: 10.1016/j.pneurobio.2017.07.002.

[177] W. L. Shew e D. Plenz, «The Functional Benefits of Criticality in the Cortex», *Neuroscientist*, vol. 19, fasc. 1, pp. 88–100, feb. 2013, doi: 10.1177/1073858412445487.

[178] D. J. Watts e S. H. Strogatz, «Collective dynamics of 'small-world' networks», vol. 393, 1998.

[179] F. Profumo, F. Borghi, A. Falqui, e P. Milani, «Potentiation and depression behaviour in a two-terminal memristor based on nanostructured bilayer ZrO x/Au films», *Journal of Physics D: Applied Physics*, vol. 56, fasc. 35, p. 355301, 2023.

[180] N. Carstens, B. Adejube, T. Strunskus, F. Faupel, S. Brown, e A. Vahl, «Brain-like critical dynamics and long-range temporal correlations in percolating networks of silver nanoparticles and functionality preservation after integration of insulating matrix», *Nanoscale Advances*, vol. 4, fasc. 15, pp. 3149–3160, 2022, doi: 10.1039/D2NA00121G.

[181] Tektronix, «2606B System SourceMeter® SMU Instrument DATASHEET». [Online]. Disponibile su: https://www.tek.com/en/datasheet/keithley-2606b-system-sourcemeter-smu-instrument

[182] O. Gronenberg *et al.*, «In Situ Imaging of Dynamic Current Paths in a Neuromorphic Nanoparticle Network with Critical Spiking Behavior», *Adv Funct Materials*, vol. 34, fasc. 28, lug. 2024, doi: 10.1002/adfm.202312989.
[183] A. Cultrera, G. Milano, N. De Leo, C. Ricciardi, L. Boarino, e L. Callegaro, «Recommended implementation of electrical resistance tomography for conductivity mapping of metallic nanowire networks using voltage excitation», *Sci Rep*, vol. 11, fasc. 1, p. 13167, giu. 2021, doi: 10.1038/s41598-021-92208-w.
[184] G. Milano, A. Cultrera, L. Boarino, L. Callegaro, e C. Ricciardi, «Tomography of memory engrams in self-organizing nanowire connectomes», *Nature Communications*, vol. 14, fasc. 1, p. 5723, set. 2023, doi: 10.1038/s41467-023-40939-x.
[185] L. Borcea, «Electrical impedance tomography», *Inverse Problems*, vol. 18, fasc. 6, pp. R99–R136, dic. 2002, doi: 10.1088/0266-5611/18/6/201.
[186] M. Wang, Q. Wang, e B. Karki, «Arts of electrical impedance tomographic sensing», *Phil. Trans. R. Soc. A.*, vol. 374, fasc. 2070, p. 20150329, giu. 2016, doi: 10.1098/rsta.2015.0329.
[187] K. Hollstein, D. Entholzner, G. Zhu, K. Weide-Zaage, e G. Benstetter, «Developing a micro-thermography system for thermal characterization of LED packages», *Microelectronic Engineering*, vol. 254, p. 111694, feb. 2022, doi: 10.1016/j.mee.2021.111694.
[188] K. S. Chang *et al.*, «Precise Temperature Mapping of GaN-Based LEDs by Quantitative Infrared Micro-Thermography», *Sensors*, vol. 12, fasc. 4, pp. 4648–4660, apr. 2012, doi: 10.3390/s120404648.
[189] Q. Li *et al.*, «Dynamic Electrical Pathway Tuning in Neuromorphic Nanowire Networks», *Adv Funct Materials*, vol. 30, fasc. 43, p. 2003679, ott. 2020, doi: 10.1002/adfm.202003679.
[190] T. Sannicolo *et al.*, «Direct Imaging of the Onset of Electrical Conduction in Silver Nanowire Networks by Infrared Thermography: Evidence of Geometrical Quantized Percolation», *Nano Lett.*, vol. 16, fasc. 11, pp. 7046–7053, nov. 2016, doi: 10.1021/acs.nanolett.6b03270.
[191] Zurich Instruments, «Principles of lock-in detection and the state of the art». 2023.
[192] M. Vollmer e K.-P. Möllmann, *Infrared thermal imaging: fundamentals, research and applications*, Second edition. Weinheim, Germany: Wiley-VCH Verlag GmbH & Co. KGaA, 2018.
[193] A. Rogalski, «Infrared detectors: an overview», *Infrared Physics & Technology*, vol. 43, fasc. 3–5, pp. 187–210, giu. 2002, doi: 10.1016/S1350-4495(02)00140-8.
[194] A. Rogalski, «Infrared detectors: status and trends», *Progress in Quantum Electronics*, vol. 27, fasc. 2–3, pp. 59–210, gen. 2003, doi: 10.1016/S0079-6727(02)00024-1.
[195] P. L. Richards, «Bolometers for infrared and millimeter waves», *Journal of Applied Physics*, vol. 76, fasc. 1, pp. 1–24, lug. 1994, doi: 10.1063/1.357128.
[196] P. V. K. Yadav, I. Yadav, B. Ajitha, A. Rajasekar, S. Gupta, e Y. Ashok Kumar Reddy, «Advancements of uncooled infrared microbolometer materials: A review», *Sensors and Actuators A: Physical*, vol. 342, p. 113611, ago. 2022, doi: 10.1016/j.sna.2022.113611.
[197] E. E. Haller, «Physics and design of advanced IR bolometers and photoconductors», *Infrared Physics*, vol. 25, fasc. 1–2, pp. 257–266, feb. 1985, doi: 10.1016/0020-0891(85)90088-0.
[198] M. Planck, «Zur Theorie des Gesetzes der Energieverteilung im Normalspektrum.», *Verh. Dtsch. Phys. Ges. 2*.

[199] H. B. Callen, *Thermodynamics and an Introduction to Thermostatistics*, 2nd edition. Wiley, 1985.
[200] J. Haglund, F. Jeppsson, e K. J. Schönborn, A c. di, *Thermal Cameras in Science Education*. in Innovations in Science Education and Technology. Cham: Springer International Publishing, 2022. doi: 10.1007/978-3-030-85288-7.
[201] FLIR Systems, «FLIR A655sc 25° Datasheet». [Online]. Disponibile su: https://support.flir.com/DsDownload/Assets/55001-0302-en-US.html
[202] J. M. Jones, P. E. Mason, e A. Williams, «A compilation of data on the radiant emissivity of some materials at high temperatures», *Journal of the Energy Institute*, vol. 92, fasc. 3, pp. 523–534, giu. 2019, doi: 10.1016/j.joei.2018.04.006.
[203] J. Khadka, S. Ganorkar, e D. Lee, «Investigation of thermal emissivity and electrical resistivity of highly reflective nano-grained metal films», *Applied Thermal Engineering*, vol. 268, p. 125854, giu. 2025, doi: 10.1016/j.applthermaleng.2025.125854.
[204] R. Kitamura, L. Pilon, e M. Jonasz, «Optical constants of silica glass from extreme ultraviolet to far infrared at near room temperature», *Appl. Opt.*, vol. 46, fasc. 33, p. 8118, nov. 2007, doi: 10.1364/ao.46.008118.
[205] R. G. Olson, «A note on Leslie's cube in the study of radiant heat», *Annals of Science*, vol. 25, fasc. 3, pp. 203–208, set. 1969, doi: 10.1080/00033796900200111.
[206] T. L. Bergman, A. S. Lavine, F. P. Incropera, e D. P. DeWitt, *Fundamentals of Heat and Mass Transfer, 8th Edition*, 8th ed. John Wiley & Sons (Wiley), 2020.
[207] J. Frolec, T. Králík, V. Musilová, P. Hanzelka, A. Srnka, e J. Jelínek, «A database of metallic materials emissivities and absorptivities for cryogenics», *Cryogenics*, vol. 97, pp. 85–99, gen. 2019, doi: 10.1016/j.cryogenics.2018.12.003.
[208] >Print FLIR Systems, «How Does Emissivity Affect Thermal Imaging?» Consultato: 24 luglio 2025. [Online]. Disponibile su: https://www.flir.com/discover/professional-tools/how-does-emissivity-affect-thermal-imaging/
[209] E. Hagen e H. Rubens, «Über Beziehungen des Reflexions- und Emissionsvermögens der Metalle zu ihrem elektrischen Leitvermögen», *Annalen der Physik*, vol. 316, fasc. 8, pp. 873–901, gen. 1903, doi: 10.1002/andp.19033160811.
[210] A. Alabastri *et al.*, «Molding of Plasmonic Resonances in Metallic Nanostructures: Dependence of the Non-Linear Electric Permittivity on System Size and Temperature», *Materials*, vol. 6, fasc. 11, pp. 4879–4910, ott. 2013, doi: 10.3390/ma6114879.
[211] M. Zhang *et al.*, «Experimental and theoretical modeling study on the infrared properties of ZrB2 thin film», *Thin Solid Films*, vol. 709, p. 138140, set. 2020, doi: 10.1016/j.tsf.2020.138140.
[212] S. Edalatpour e M. Francoeur, «Size effect on the emissivity of thin films», *Journal of Quantitative Spectroscopy and Radiative Transfer*, vol. 118, pp. 75–85, mar. 2013, doi: 10.1016/j.jqsrt.2012.12.012.
[213] P. J. Van Zwol *et al.*, «Emissivity of freestanding membranes with thin metal coatings», *Journal of Applied Physics*, vol. 118, fasc. 21, dic. 2015, doi: 10.1063/1.4936851.
[214] E. Petryayeva e U. J. Krull, «Localized surface plasmon resonance: Nanostructures, bioassays and biosensing—A review», *Analytica Chimica Acta*, vol. 706, fasc. 1, pp. 8–24, nov. 2011, doi: 10.1016/j.aca.2011.08.020.
[215] W. Sabuga e R. Todtenhaupt, «Effect of roughness on the emissivity of the precious metals silver, gold, palladium, platinum, rhodium, and iridium», *High Temp.-High Press.*, vol. 33, fasc. 3, pp. 261–269, 2001, doi: 10.1068/htwu371.

[216] C. Zhu, M. J. Hobbs, e J. R. Willmott, «An accurate instrument for emissivity measurements by direct and indirect methods», *Meas. Sci. Technol.*, vol. 31, fasc. 4, p. 044007, gen. 2020, doi: 10.1088/1361-6501/ab5e9b.

[217] M. Siroux, E. Tang-Kwor, e S. Matteï, «A periodic technique for emissivity measurements of insulating materials at moderate temperature», *Meas. Sci. Technol.*, vol. 9, fasc. 12, pp. 1956–1962, dic. 1998, doi: 10.1088/0957-0233/9/12/005.

[218] L. Del Campo, R. B. Pérez-Sáez, X. Esquisabel, I. Fernández, e M. J. Tello, «New experimental device for infrared spectral directional emissivity measurements in a controlled environment», *Review of Scientific Instruments*, vol. 77, fasc. 11, nov. 2006, doi: 10.1063/1.2393157.

[219] I. Vishnevetsky, E. Rotenberg, A. Kribus, e D. Yakir, «Method for accurate measurement of infrared emissivity for opaque low-reflectance materials», *Appl. Opt.*, vol. 58, fasc. 17, p. 4599, giu. 2019, doi: 10.1364/ao.58.004599.

[220] V. A. Golyk, M. Krüger, e M. Kardar, «Heat radiation from long cylindrical objects», *Phys. Rev. E*, vol. 85, fasc. 4, p. 046603, apr. 2012, doi: 10.1103/PhysRevE.85.046603.

[221] I. Jolliffe, «Principal Component Analysis», in *International Encyclopedia of Statistical Science*, M. Lovric, A c. di, Berlin, Heidelberg: Springer Berlin Heidelberg, 2011, pp. 1094–1096. doi: 10.1007/978-3-642-04898-2_455.

[222] A. L. Pomerantsev, *Chemometrics in Excel*, 1ª ed. Wiley, 2014. doi: 10.1002/9781118873212.

[223] P. J. Francis e B. J. Wills, «Introduction to Principal Components Analysis», 1999, *arXiv*. doi: 10.48550/ARXIV.ASTRO-PH/9905079.

[224] J. Lever, M. Krzywinski, e N. Altman, «Principal component analysis», *Nat Methods*, vol. 14, fasc. 7, pp. 641–642, lug. 2017, doi: 10.1038/nmeth.4346.

[225] V. Klema e A. Laub, «The singular value decomposition: Its computation and some applications», *IEEE Trans. Automat. Contr.*, vol. 25, fasc. 2, pp. 164–176, apr. 1980, doi: 10.1109/TAC.1980.1102314.

[226] D. Kerschensteiner e R. O. L. Wong, «A Precisely Timed Asynchronous Pattern of ON and OFF Retinal Ganglion Cell Activity during Propagation of Retinal Waves», *Neuron*, vol. 58, fasc. 6, pp. 851–858, giu. 2008, doi: 10.1016/j.neuron.2008.04.025.

[227] P. B. Kruskal, J. J. Stanis, B. L. McNaughton, e P. J. Thomas, «A binless correlation measure reduces the variability of memory reactivation estimates», *Statistics in Medicine*, vol. 26, fasc. 21, pp. 3997–4008, set. 2007, doi: 10.1002/sim.2946.

[228] P. X. Joris, D. H. Louage, L. Cardoen, e M. Van Der Heijden, «Correlation Index: A new metric to quantify temporal coding», *Hearing Research*, vol. 216–217, pp. 19–30, giu. 2006, doi: 10.1016/j.heares.2006.03.010.

[229] R. O. L. Wong, M. Meister, e C. J. Shatz, «Transient period of correlated bursting activity during development of the mammalian retina», *Neuron*, vol. 11, fasc. 5, pp. 923–938, nov. 1993, doi: 10.1016/0896-6273(93)90122-8.

[230] C. S. Cutts e S. J. Eglen, «Detecting Pairwise Correlations in Spike Trains: An Objective Comparison of Methods and Application to the Study of Retinal Waves», *J. Neurosci.*, vol. 34, fasc. 43, pp. 14288–14303, ott. 2014, doi: 10.1523/JNEUROSCI.2767-14.2014.

[231] D. Cabrera-Garcia, D. Warm, P. de la Fuente, M. T. Fernández-Sánchez, A. Novelli, e J. M. Villanueva-Balsera, «Early prediction of developing spontaneous activity in cultured neuronal networks», *Sci Rep*, vol. 11, fasc. 1, p. 20407, ott. 2021, doi: 10.1038/s41598-021-99538-9.

[232] M. Chini, T. Pfeffer, e I. Hanganu-Opatz, «An increase of inhibition drives the developmental decorrelation of neural activity», *eLife*, vol. 11, p. e78811, 2022, doi: 10.7554/eLife.78811.

[233] H. Roh, S. Kim, H.-M. Lee, e M. Im, «Quantitative analyses of how optimally heterogeneous neural codes maximize neural information in jittery transmission environments», *Sci Rep*, vol. 14, fasc. 1, p. 29623, nov. 2024, doi: 10.1038/s41598-024-81029-2.

[234] D. P. Hunley, S. L. Johnson, R. L. Flores, A. Sundararajan, e D. R. Strachan, «Analytical model for self-heating in nanowire geometries», *Journal of Applied Physics*, vol. 113, fasc. 23, p. 234306, giu. 2013, doi: 10.1063/1.4811444.

[235] S. D. Sawtelle, «Electromigration and Electrothermal Properties in Gold Nanostructures», Yale University, 2018.

[236] P. Pu, M. Tang, e J. Mao, «Analytical Thermal Modeling of Nanowire Structures Including Self-Heating Effects», in *2019 Cross Strait Quad-Regional Radio Science and Wireless Technology Conference (CSQRWC)*, Taiyuan, China: IEEE, lug. 2019, pp. 1–2. doi: 10.1109/CSQRWC.2019.8799346.

[237] O. M. G. Ward e E. McCann, «The heat equation for nanoconstrictions in 2D materials with Joule self-heating», *J. Phys. D: Appl. Phys.*, vol. 54, fasc. 47, p. 475303, nov. 2021, doi: 10.1088/1361-6463/ac21fe.

[238] D. P. Langley *et al.*, «Metallic nanowire networks: effects of thermal annealing on electrical resistance», *Nanoscale*, vol. 6, fasc. 22, pp. 13535–13543, 2014, doi: 10.1039/C4NR04151H.

[239] S. Coskun, E. Selen Ates, e H. Emrah Unalan, «Optimization of silver nanowire networks for polymer light emitting diode electrodes», *Nanotechnology*, vol. 24, fasc. 12, p. 125202, mar. 2013, doi: 10.1088/0957-4484/24/12/125202.

[240] Z. Ebrahimpour e N. Mansour, «Annealing effects on electrical behavior of gold nanoparticle film: Conversion of ohmic to non-ohmic conductivity», *Applied Surface Science*, vol. 394, pp. 240–247, feb. 2017, doi: 10.1016/j.apsusc.2016.10.041.

[241] A. E. B. Presland, G. L. Price, e D. L. Trimm, «Kinetics of hillock and island formation during annealing of thin silver films», *Progress in Surface Science*, vol. 3, pp. 63–96, gen. 1972, doi: 10.1016/0079-6816(72)90006-8.

[242] C. V. Thompson, «Solid-State Dewetting of Thin Films», *Annu. Rev. Mater. Res.*, vol. 42, fasc. 1, pp. 399–434, ago. 2012, doi: 10.1146/annurev-matsci-070511-155048.

[243] J. Mizsei e V. Lantto, «In situ AFM, XRD and Resistivity Studies of the Agglomeration of Sputtered Silver Nanolayers», *Journal of Nanoparticle Research*, vol. 3, fasc. 4, pp. 271–278, ago. 2001, doi: 10.1023/A:1017575413163.

[244] P. R. Gadkari, A. P. Warren, R. M. Todi, R. V. Petrova, e K. R. Coffey, «Comparison of the agglomeration behavior of thin metallic films on SiO2», *Journal of Vacuum Science & Technology A: Vacuum, Surfaces, and Films*, vol. 23, fasc. 4, pp. 1152–1161, lug. 2005, doi: 10.1116/1.1861943.

[245] A. B. Tesler, B. M. Maoz, Y. Feldman, A. Vaskevich, e I. Rubinstein, «Solid-State Thermal Dewetting of Just-Percolated Gold Films Evaporated on Glass: Development of the Morphology and Optical Properties», *J. Phys. Chem. C*, vol. 117, fasc. 21, pp. 11337–11346, mag. 2013, doi: 10.1021/jp400895z.

[246] S. W. Holman, R. R. Lawrence, e L. Barr, «Melting Points of Aluminum, Silver, Gold, Copper, and Platinum», *Proceedings of the American Academy of Arts and Sciences*, vol. 31, p. 218, 1895, doi: 10.2307/20020628.

[247] Ph. Buffat e J.-P. Borel, «Size effect on the melting temperature of gold particles», *Phys. Rev. A*, vol. 13, fasc. 6, pp. 2287–2298, giu. 1976, doi: 10.1103/PhysRevA.13.2287.
[248] Z. Ye *et al.*, «Thermal Annealing Effect on Surface-Enhanced Raman Scattering of Gold Films Deposited on Liquid Substrates», *Molecules*, vol. 28, fasc. 3, p. 1472, feb. 2023, doi: 10.3390/molecules28031472.
[249] J. R. Lloyd, «Electromigration in thin film conductors», *Semicond. Sci. Technol.*, vol. 12, fasc. 10, pp. 1177–1185, ott. 1997, doi: 10.1088/0268-1242/12/10/002.
[250] R. Hoffmann-Vogel, «Electromigration and the structure of metallic nanocontacts», *Applied Physics Reviews*, vol. 4, fasc. 3, p. 031302, set. 2017, doi: 10.1063/1.4994691.
[251] R. S. Sorbello, «Theory of the direct force in electromigration», *Phys. Rev. B*, vol. 31, fasc. 2, pp. 798–804, gen. 1985, doi: 10.1103/PhysRevB.31.798.
[252] H. B. Huntington, «Driving forces for thermal mass transport», *Journal of Physics and Chemistry of Solids*, vol. 29, fasc. 9, pp. 1641–1651, set. 1968, doi: 10.1016/0022-3697(68)90106-6.
[253] H. B. Huntington, «Effect of driving forces on atom motion», *Thin Solid Films*, vol. 25, fasc. 2, pp. 265–280, feb. 1975, doi: 10.1016/0040-6090(75)90047-4.
[254] R. A. McKee, «A generalization of the Nernst-Einstein equation for self-diffusion in high defect concentration solids», *Solid State Ionics*, vol. 5, pp. 133–136, ott. 1981, doi: 10.1016/0167-2738(81)90210-1.
[255] I. A. Blech e C. Herring, «Stress generation by electromigration», *Applied Physics Letters*, vol. 29, fasc. 3, pp. 131–133, ago. 1976, doi: 10.1063/1.89024.
[256] J. R. Black, «Mass Transport of Aluminum by Momentum Exchange with Conducting Electrons», in *6th Annual Reliability Physics Symposium (IEEE)*, Los Angeles, CA, USA: IEEE, nov. 1967, pp. 148–159. doi: 10.1109/IRPS.1967.362408.
[257] M. L. Trouwborst, S. J. Van Der Molen, e B. J. Van Wees, «The role of Joule heating in the formation of nanogaps by electromigration», *Journal of Applied Physics*, vol. 99, fasc. 11, giu. 2006, doi: 10.1063/1.2203410.
[258] D. Yu *et al.*, «Electromigration-Induced Evolution of Micromorphology and Electrical Properties in Gold Nanowires: Implications for Nanoelectronics», *ACS Appl. Nano Mater.*, vol. 7, fasc. 13, pp. 14906–14920, lug. 2024, doi: 10.1021/acsanm.4c00189.
[259] F. Profumo, F. Borghi, A. Falqui, e P. Milani, «Potentiation and depression behaviour in a two-terminal memristor based on nanostructured bilayer ZrOx/Au films», *Journal of Physics D: Applied Physics*, vol. 56, fasc. 35, p. 355301, giu. 2023, doi: 10.1088/1361-6463/acd704.
[260] S. Radice, F. Profumo, F. Borghi, A. Falqui, e P. Milani, «Programmable Analog Circuits with Neuromorphic Nanostructured Platinum Films», *Advanced Electronic Materials*, vol. n/a, fasc. n/a, p. 2400434, 2024, doi: 10.1002/aelm.202400434.
[261] G. Nadalini, A. Dallinger, D. Sottocorno, F. Greco, F. Borghi, e P. Milani, «Soft Electronic Switches and Adaptive Logic Gates Based on Nanostructured Gold Networks», *Adv Elect Materials*, p. 2400717, 2024, doi: 10.1002/aelm.202400717.
[262] G. Milano *et al.*, «Quantum Conductance in Memristive Devices: Fundamentals, Developments, and Applications», *Advanced Materials*, vol. 34, fasc. 32, p. 2201248, ago. 2022, doi: 10.1002/adma.202201248.
[263] D. Cabrera-Garcia, D. Warm, P. De La Fuente, M. T. Fernández-Sánchez, A. Novelli, e J. M. Villanueva-Balsera, «Early prediction of developing spontaneous activity in cultured neuronal networks», *Sci Rep*, vol. 11, fasc. 1, p. 20407, ott. 2021, doi: 10.1038/s41598-021-99538-9.

[264] T. Nieus, E. Sola, J. Mapelli, E. Saftenku, P. Rossi, e E. D'Angelo, «LTP Regulates Burst Initiation and Frequency at Mossy Fiber–Granule Cell Synapses of Rat Cerebellum: Experimental Observations and Theoretical Predictions», *Journal of Neurophysiology*, vol. 95, fasc. 2, pp. 686–699, feb. 2006, doi: 10.1152/jn.00696.2005.

[265] J. C. van den Berg, *Wavelets in Physics*. Wageningen, The Netherlands: J. C. van den Berg, Agricultural University, 1999.

[266] Z. Heywood *et al.*, «Self-organized nanoscale networks: are neuromorphic properties conserved in realistic device geometries?», *Neuromorph. Comput. Eng.*, vol. 2, fasc. 2, p. 024009, giu. 2022, doi: 10.1088/2634-4386/ac74da.

[267] M. Mirigliano, S. Radice, A. Falqui, A. Casu, F. Cavaliere, e P. Milani, «Anomalous electrical conduction and negative temperature coefficient of resistance in nanostructured gold resistive switching films», *Sci Rep*, vol. 10, fasc. 1, nov. 2020, doi: 10.1038/s41598-020-76632-y.

[268] M. Chiappalone, M. Bove, A. Vato, M. Tedesco, e S. Martinoia, «Dissociated cortical networks show spontaneously correlated activity patterns during in vitro development», *Brain Research*, vol. 1093, fasc. 1, pp. 41–53, giu. 2006, doi: 10.1016/j.brainres.2006.03.049.

[269] N. Dehorter, L. Vinay, C. Hammond, e Y. Ben-Ari, «Timing of developmental sequences in different brain structures: physiological and pathological implications», *Eur J of Neuroscience*, vol. 35, fasc. 12, pp. 1846–1856, giu. 2012, doi: 10.1111/j.1460-9568.2012.08152.x.

[270] A. A. Fingelkurts, A. A. Fingelkurts, e S. Kähkönen, «Functional connectivity in the brain—is it an elusive concept?», *Neuroscience & Biobehavioral Reviews*, vol. 28, fasc. 8, pp. 827–836, gen. 2005, doi: 10.1016/j.neubiorev.2004.10.009.

[271] K. J. Friston, C. D. Frith, P. F. Liddle, e R. S. J. Frackowiak, «Functional Connectivity: The Principal-Component Analysis of Large (PET) Data Sets», *J Cereb Blood Flow Metab*, vol. 13, fasc. 1, pp. 5–14, gen. 1993, doi: 10.1038/jcbfm.1993.4.

[272] F. O. Morin, Y. Takamura, e E. Tamiya, «Investigating neuronal activity with planar microelectrode arrays: achievements and new perspectives», *Journal of Bioscience and Bioengineering*, vol. 100, fasc. 2, pp. 131–143, ago. 2005, doi: 10.1263/jbb.100.131.

[273] C. Chen, L. Chen, Y. Lin, S. Zeng, e Q. Luo, «The origin of spontaneous synchronized burst in cultured neuronal networks based on multi-electrode arrays», *Biosystems*, vol. 85, fasc. 2, pp. 137–143, ago. 2006, doi: 10.1016/j.biosystems.2005.12.006.

[274] T. Kobayashi, K. Shimba, T. Narumi, T. Asahina, K. Kotani, e Y. Jimbo, «Revealing single-neuron and network-activity interaction by combining high-density microelectrode array and optogenetics», *Nat Commun*, vol. 15, fasc. 1, p. 9547, nov. 2024, doi: 10.1038/s41467-024-53505-w.

[275] G. Tononi, «Complexity and coherency: integrating information in the brain», *Trends in Cognitive Sciences*, vol. 2, fasc. 12, pp. 474–484, dic. 1998, doi: 10.1016/S1364-6613(98)01259-5.

[276] G. Tononi, O. Sporns, e G. M. Edelman, «A measure for brain complexity: relating functional segregation and integration in the nervous system.», *Proc. Natl. Acad. Sci. U.S.A.*, vol. 91, fasc. 11, pp. 5033–5037, mag. 1994, doi: 10.1073/pnas.91.11.5033.

[277] D. J. Watts e S. H. Strogatz, «Collective dynamics of 'small-world' networks», *Nature*, vol. 393, fasc. 6684, pp. 440–442, giu. 1998, doi: 10.1038/30918.

[278] O. Sporns e J. D. Zwi, «The Small World of the Cerebral Cortex», *NI*, vol. 2, fasc. 2, pp. 145–162, 2004, doi: 10.1385/NI:2:2:145.

[279] D. Fraiman, P. Balenzuela, J. Foss, e D. R. Chialvo, «Ising-like dynamics in large-scale functional brain networks», *Phys. Rev. E*, vol. 79, fasc. 6, p. 061922, giu. 2009, doi: 10.1103/PhysRevE.79.061922.

[280] C. J. Stam, «Functional connectivity patterns of human magnetoencephalographic recordings: a 'small-world' network?», *Neuroscience Letters*, vol. 355, fasc. 1–2, pp. 25–28, gen. 2004, doi: 10.1016/j.neulet.2003.10.063.

[281] D. R. Chialvo, «Emergent complex neural dynamics», *Nature Phys*, vol. 6, fasc. 10, pp. 744–750, ott. 2010, doi: 10.1038/nphys1803.

[282] V. Pasquale, P. Massobrio, L. L. Bologna, M. Chiappalone, e S. Martinoia, «Self-organization and neuronal avalanches in networks of dissociated cortical neurons», *Neuroscience*, vol. 153, fasc. 4, pp. 1354–1369, giu. 2008, doi: 10.1016/j.neuroscience.2008.03.050.

[283] W. L. Shew, H. Yang, S. Yu, R. Roy, e D. Plenz, «Information Capacity and Transmission Are Maximized in Balanced Cortical Networks with Neuronal Avalanches», *J. Neurosci.*, vol. 31, fasc. 1, pp. 55–63, gen. 2011, doi: 10.1523/JNEUROSCI.4637-10.2011.

[284] C. S. Dunham *et al.*, «Nanoscale neuromorphic networks and criticality: a perspective», *Journal of Physics: Complexity*, vol. 2, fasc. 4, p. 042001, dic. 2021, doi: 10.1088/2632-072X/ac3ad3.

[285] G. Mijatovic, T. Loncar-Turukalo, e N. Bozanic, «Investigating Neural Correlations – an Approach to Measure Concurrent Firing Activity», in *2020 11th Conference of the European Study Group on Cardiovascular Oscillations (ESGCO)*, Pisa, Italy: IEEE, lug. 2020, pp. 1–2. doi: 10.1109/ESGCO49734.2020.9158035.

[286] T. Kreuz, J. S. Haas, A. Morelli, H. D. I. Abarbanel, e A. Politi, «Measuring spike train synchrony», *Journal of Neuroscience Methods*, vol. 165, fasc. 1, pp. 151–161, set. 2007, doi: 10.1016/j.jneumeth.2007.05.031.

[287] J. P. Sethna, K. A. Dahmen, e C. R. Myers, «Crackling noise», *Nature*, vol. 410, fasc. 6825, pp. 242–250, mar. 2001, doi: 10.1038/35065675.

[288] L. Chen, Y. Deng, W. Luo, Z. Wang, e S. Zeng, «Detection of bursts in neuronal spike trains by the mean inter-spike interval method», *Progress in Natural Science*, 2009.

[289] D. E. Johnston, D. R. Strachan, e A. T. C. Johnson, «Parallel Fabrication of Nanogap Electrodes», *Nano Lett.*, vol. 7, fasc. 9, pp. 2774–2777, set. 2007, doi: 10.1021/nl0713169.

[290] Z. Tian *et al.*, «Metal Nanogap Memory: Performances and Switching Mechanism», *ACS Appl. Mater. Interfaces*, vol. 16, fasc. 20, pp. 26360–26373, mag. 2024, doi: 10.1021/acsami.4c01597.

[291] M. Olsen, M. Hummelgård, e H. Olin, «Surface Modifications by Field Induced Diffusion», *PLoS ONE*, vol. 7, fasc. 1, p. e30106, gen. 2012, doi: 10.1371/journal.pone.0030106.

[292] A. Sattar, S. Fostner, e S. A. Brown, «Quantized Conductance and Switching in Percolating Nanoparticle Films», *Phys. Rev. Lett.*, vol. 111, fasc. 13, p. 136808, set. 2013, doi: 10.1103/PhysRevLett.111.136808.

[293] G. Martini, E. Tentori, M. Mirigliano, D. E. Galli, P. Milani, e F. Mambretti, «Efficiency and controllability of stochastic boolean function generation by a random network of non-linear nanoparticle junctions», *Front. Phys.*, vol. 12, p. 1400919, mag. 2024, doi: 10.3389/fphy.2024.1400919.

[294] W. J. Hill e W. G. Hunter, «A Review of Response Surface Methodology: A Literature Survey», *Technometrics*, vol. 8, fasc. 4, p. 571, nov. 1966, doi: 10.2307/1266632.

[295] J. Wang, «An Intuitive Tutorial to Gaussian Process Regression», *Comput. Sci. Eng.*, vol. 25, fasc. 4, pp. 4–11, lug. 2023, doi: 10.1109/MCSE.2023.3342149.

[296] G. Milano, F. Michieletti, C. Ricciardi, e E. Miranda, «Self-organizing neuromorphic nanowire networks are stochastic dynamical systems», 4 aprile 2024. doi: 10.21203/rs.3.rs-4102090/v1.

[297] G. Milano, E. Miranda, e C. Ricciardi, «Connectome of memristive nanowire networks through graph theory», *Neural Networks*, vol. 150, pp. 137–148, giu. 2022, doi: 10.1016/j.neunet.2022.02.022.

[298] E. Miranda, G. Milano, e C. Ricciardi, «Modeling of Short-Term Synaptic Plasticity Effects in ZnO Nanowire-Based Memristors Using a Potentiation-Depression Rate Balance Equation», *IEEE Trans. Nanotechnology*, vol. 19, pp. 609–612, 2020, doi: 10.1109/TNANO.2020.3009734.

[299] D. B. Strukov, G. S. Snider, D. R. Stewart, e R. S. Williams, «The missing memristor found», *Nature*, vol. 453, fasc. 7191, pp. 80–83, mag. 2008, doi: 10.1038/nature06932.

[300] D. Shaik e S. Sahoo, «Memristor and Its Modelling: A Review», in *Proceedings of Fifth International Conference on Inventive Material Science Applications*, V. Bindhu, J. M. R. S. Tavares, e J. I.-Z. Chen, A c. di, in Advances in Sustainability Science and Technology. , Singapore: Springer Nature Singapore, 2023, pp. 219–233. doi: 10.1007/978-981-19-4304-1_20.

[301] F. Yuan *et al.*, «Real-Time Observation of the Electrode-Size-Dependent Evolution Dynamics of the Conducting Filaments in a SiO_2 Layer», *ACS Nano*, vol. 11, fasc. 4, pp. 4097–4104, apr. 2017, doi: 10.1021/acsnano.7b00783.

[302] J. Chen *et al.*, «High-performance perovskite memristor by integrating a tip-shape contact», *J. Mater. Chem. C*, vol. 9, fasc. 43, pp. 15435–15444, 2021, doi: 10.1039/D1TC04164A.

[303] R. G. Forbes, C. J. Edgcombe, e U. Valdrè, «Some comments on models for field enhancement», *Ultramicroscopy*, vol. 95, pp. 57–65, mag. 2003, doi: 10.1016/S0304-3991(02)00297-8.

Acknowledgements

This thesis is the result of an intense effort carried out over the past several years and, at the same time, represents the culmination of a much longer journey. Its completion was made possible also thanks to the many wonderful people who have accompanied me along the way. Challenging moments were certainly not lacking, and if I have been able to reach this goal, it is also because I was privileged to receive the support of so many extraordinary people around me.

First and foremost, I would like to thank my parents and my family, who raised me with care and affection and have always supported my choices. Without them, I would not have achieved much. A special acknowledgment goes to my beloved grandparents, that I remember with affection and gratitude.

I would like to sincerely thank my supervisor, Prof. Paolo Milani, for welcoming me into his research group, for the valuable insights that significantly contributed to my professional growth, and for always placing his trust in me. I am equally grateful to my co-supervisor, Dr. Francesca Borghi, for her constant support and friendship over all these years and for helping me growing professionally. I sincerely thank Dr. Claudio Piazzoni for introducing me to the laboratory equipment, thus contributing to the development of my technical skills, and for always providing essential support throughout this work.

A very special acknowledgement goes to my longtime friends Martina, Luca, Chiara, Alex, Giulia, Fabio, Nata, Paolo, and Vera who have always shown me great affection and closeness during difficult times, and whose companionship I have been fortunate to enjoy for many years. I care deeply for you all and promise I will make a real effort to see you more often.

I would like to thank all the wonderful people I had the pleasure to meet over these years at the CIMaINa laboratories, especially my colleagues and dear friends Silvia, Stefano, Gianluca, Giacomo, and Filippo, for the meaningful exchanges we shared, for their constant support, and for making this journey less demanding through their invaluable friendship.

I am also grateful to all the friends with whom I shared my university life, along with a healthy amount of delightfully chaotic moments: Lorenz, Alli, Cristina, Karina, Petru, Laura, Marco, Sidra, Jacob, Valentina, Luca, Elena, Llorenç: you are truly amazing!

I would like to thank all the students who collaborated with me that shared part of this journey, as well as sincere friendships. In particular, I want to thank Cristina, Stefano, Davide, Tommaso, Amara, Mattia, Giacomo, Carmen, Miriam. Your curiosity and commitment greatly helped me to learn and to improve this work. I hope I was able to pass on something meaningful to you, and I wish you all a future full of joy.

A very special acknowledgment goes to my former undergraduate thesis advisor, and dear friend, Matteo. Looking back, I realize that his precious guidance during my first steps into scientific research has been truly decisive for my professional growth.

I would like to express my sincere gratitude to the members of FUCI, who welcomed me as a friend during the final period of my studies and allowed me to experience the value of an active approach to student life. Through them, I learned not to face the challenges of university life passively, but rather to make use of this time as an opportunity for personal growth and human development. Viva la FUCI! Likewise, I would like to thank the friends I met inside Azione Cattolica. I had the privilege to share with them a truly meaningful journey of faith and friendship. Each of you has witnessed something precious to me, which I will certainly keep in my heart.

Thank you for helping me in finding the joy of living in Jesus. I have come to realize that I would not get very far without Him. Thanks to all of you, I have rediscovered my professional skills as something that can be offered as a gift, with the hope that in the future they may become fruitful for others.

Finally, I would like to thank with great affection the members of the Cemband, for more than ten years of playing good music together, for their precious friendship, and, above all, for patiently enduring my frequent off-key moments.